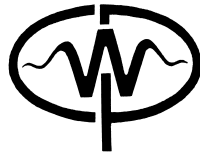


CWP-551
April 2006



Seismic Wave Propagation in Attenuative Anisotropic Media

Yaping Zhu

— Doctoral Thesis —
Geophysics

Defended on April 26, 2006

Committee Chair:	Prof. Panagiotis Kiousis
Advisor:	Prof. Ilya Tsvankin
Committee members:	Prof. Ken Larner
	Prof. Roel Snieder
	Prof. Tom Boyd
	Prof. Luis Tenorio
	Prof. Douglas Hart

Center for Wave Phenomena
Colorado School of Mines
Golden, Colorado 80401
(1) 303 273-3557

Abstract

Directionally-dependent attenuation may strongly influence body-wave amplitudes and distort the results of the AVO (amplitude variation with offset) analysis. Following the idea of Thomsen's (1986) notation for velocity anisotropy, I introduce a set of attenuation-anisotropy parameters for TI (transversely isotropic) and orthorhombic media, which have similar physical meaning to the corresponding velocity-anisotropy parameters. Based on the concept of homogeneous wave propagation (i.e., the real and imaginary parts of the wave vector are assumed to be parallel to one another), I analyze plane-wave properties for TI and orthorhombic media and obtain linearized attenuation coefficients for models with weak attenuation as well as weak velocity and attenuation anisotropy. I then analyze measurements of the P-wave attenuation coefficient in a transversely isotropic sample made of phenolic material using the anisotropic version of the spectral-ratio method, which takes into account the difference between the group and phase attenuation. Recovered attenuation-anisotropy parameters demonstrate that attenuation anisotropy can be much stronger than velocity anisotropy.

To explore the physical reasons for attenuation anisotropy of finely layered media, I apply Backus averaging to obtain the effective attenuation-anisotropy parameters for a medium formed by an arbitrary number of anisotropic, attenuative constituents. Using approximate solutions, I evaluate the contributions of various factors (related to both heterogeneity and intrinsic anisotropy) to the effective attenuation anisotropy. Interestingly, the effective attenuation for P- and SV-waves is anisotropic even for a medium composed of isotropic layers with no attenuation contrast, provided there is a velocity variation among the constituent layers. Contrasts in the intrinsic attenuation, however, do not create attenuation anisotropy, unless they are accompanied by velocity contrasts. Further analysis for models composed of azimuthally anisotropic constituents with misaligned vertical symmetry planes suggests the possibility of different symmetries and principal azimuthal directions of the effective velocity and attenuation.

Finally, I present an asymptotic study of 2D far-field radiation from seismic sources for media with anisotropic velocity and attenuation functions and discuss the influence of the inhomogeneity angle on the radiation patterns and the relationship between the phase and group attenuation coefficients.

An approximate answer to the right problem is worth a good deal more than an exact answer to an approximate problem.

(John Tukey)

Table of Contents

Abstract	i
	iii
Acknowledgments	ix
Chapter 1 Introduction	1
1.1 Motivation	1
1.2 Assumptions	3
1.3 Thesis layout	3
Chapter 2 Plane-wave attenuation anisotropy for TI media	5
2.1 Summary	5
2.2 Introduction	5
2.3 Definition of the \mathbf{Q} matrix	6
2.3.1 Christoffel equation for anisotropic, attenuative media	8
2.4 SH-wave attenuation	9
2.4.1 Isotropic attenuation	9
2.4.2 VTI attenuation	10
2.5 P- and SV-wave attenuation	11
2.6 Thomsen-style notation for VTI attenuation	13
2.6.1 SH-wave parameter γ_Q	15
2.6.2 P-SV wave parameters ϵ_Q and δ_Q	16
2.7 Approximate attenuation coefficients for P- and SV-waves	19
2.7.1 Approximate P-wave attenuation	19
2.7.2 Approximate SV-wave attenuation	19
2.7.3 <i>Isotropic</i> attenuation coefficients	20
2.7.4 Numerical examples	21
2.8 Summary and conclusions	25
Chapter 3 Plane-wave attenuation anisotropy for orthorhombic media	29
3.1 Summary	29
3.2 Introduction	29
3.3 Christoffel equation for attenuative orthorhombic media	30
3.4 Attenuation coefficients in the symmetry planes	32

3.5	Attenuation-anisotropy parameters	34
3.5.1	Thomsen-style notation	34
3.6	Approximate attenuation coefficients in the symmetry planes	37
3.7	P-wave attenuation outside the symmetry planes	38
3.7.1	Influence of attenuation on phase velocity	39
3.7.2	Approximate attenuation outside the symmetry planes	39
3.7.3	Parameters for P-wave attenuation	43
3.7.4	Accuracy of the linearized solution	43
3.8	Summary and observations	45
Chapter 4 Physical modeling and analysis of P-wave attenuation anisotropy for TI media		51
4.1	Summary	51
4.2	Introduction	51
4.3	Spectral-ratio method for anisotropic attenuation	52
4.4	Experimental setup and data processing	53
4.5	Evaluation of attenuation anisotropy	55
4.5.1	Estimation of the attenuation-anisotropy parameters	56
4.5.2	Uncertainty analysis	58
4.6	Discussion	60
4.7	Conclusions	62
4.8	Acknowledgments	62
Chapter 5 Effective attenuation anisotropy of layered media		63
5.1	Summary	63
5.2	Introduction	64
5.3	Effective parameters of layered anisotropic attenuative media	64
5.3.1	Effective stiffnesses for TI media	66
5.4	Approximate attenuation parameters of effective VTI media	67
5.4.1	First-order approximation	68
5.4.2	Second-order approximation	68
5.4.3	Velocity contrast versus attenuation contrast	70
5.5	Accuracy of the approximations	73
5.5.1	Magnitude of attenuation anisotropy	77
5.6	Effective symmetry for azimuthally anisotropic media	81
5.7	Discussion and conclusions	84
Chapter 6 Far-field radiation from seismic sources in 2D attenuative anisotropic media		89
6.1	Summary	89
6.2	Introduction	89

6.3	Inhomogeneity angle	90
6.4	VTI media with VTI attenuation	91
6.4.1	SH-waves	91
6.4.2	P- and SV-waves	92
6.4.3	Numerical examples	93
6.5	Radiation patterns	96
6.5.1	Phase and group properties	96
6.5.2	Numerical examples	97
6.6	Discussion and conclusions	99
Chapter 7 Conclusions and recommendations		103
7.1	Conclusions	103
7.2	Recommendations	104
References		107
Appendix A Plane SH-waves in attenuative VTI media		113
A.1	VTI \mathbf{Q} matrix: Inhomogeneous wave propagation	113
A.2	VTI \mathbf{Q} matrix: Homogeneous wave propagation	115
A.3	Isotropic \mathbf{Q} matrix	116
Appendix B Plane P- and SV-waves in attenuative VTI media		117
B.1	VTI \mathbf{Q} -matrix	117
B.2	Special case: $Q_{ij} \equiv Q$	119
Appendix C Approximate solutions for weak attenuation and weak attenuation anisotropy		121
C.0.1	Attenuation coefficients for P- and SV-waves	121
C.0.2	Parameter δ_Q	122
Appendix D Isotropic conditions for the attenuation coefficient k^I		123
D.0.3	SH-wave	123
D.0.4	P-SV waves	123
Appendix E Approximate attenuation outside the symmetry planes of orthorhombic media		125
Appendix F Second-order approximation for the effective parameters		129
F.0.5	Anisotropy parameters for SH-waves	129
F.0.6	Anisotropy parameters for P- and SV-waves	132
Appendix G Radiation patterns for 2D attenuative anisotropic media		137

Acknowledgments

I am deeply grateful to Center for Wave Phenomena for supporting my PhD study over the years.

I appreciate the continuous assistance from my thesis committee, Dr. Panagiotis Kioussis, Dr. Ilya Tsvankin, Dr. Ken Larner, Dr. Roel Snieder, Dr. Tom Boyd, Dr. Luis Tenorio, and Dr. Douglas Hart. My thesis advisor, Dr. Ilya Tsvankin, guided me through the thesis work and influenced me with his deep physical insight. I felt fortunate enough that he didn't call me an idiot when I was wrong. Dr. Ken Larner's (and later on Dr. Ilya Tsvankin's) red pens greatly improved my writing of technical reports. Dr. Roel Snieder not only guided me through my first comps project but also shared with me his research style through the course *Art of Science*. The department head, Dr. Terry Young, was always there to listen and give advice. I am greatly indebted to Dr. Yaoguo Li for his guidance at difficult times. I also thank Dr. Andrey Bakulin and Dr. Vladimir Grechka (both from Shell E&P) for discussions on the thesis topic.

So many people shared with me their valuable time that I cannot provide a complete list of names: Matt Haney, Marty Terrell, Richard Krahenbuhl, Albena Mateeva, Debashish Sarkar, Alex Grêt, Petr Jílek, Alison Malcolm, Pawan Dewangan, Huub Douma, Rodrigo Fuck, Carlos Pacheco, Xiaoxia Xu, Ivan Vasconcelos, Jyoti Behura, Kurang Mehta, Jia Yan, Steve Smith, Matt Renolds, Dongjie Cheng, Zhaobo Meng, André Pech, Lydia Deng, Ronny Hofmann, Reynaldo Cardona, Niran Tasdemir, and Amir Ghaderi. Dr. Kasper van Wijk kindly acquired the transmission data used in Chapter 4. Dr. Mike Batzle opened an exciting attenuation world to me and showed (with his humor) how little I had learned about rock physics. John Stockwell helped me not only with computer problems but also with mathematical issues. Moreover, I thank Dr. Tom Davis, Dr. Dave Hale, Dr. Paul Sava, and the visiting professor, Dr. Martin Landrø, for useful discussions.

I miss Lela Webber, who helped me looking for an apartment (and later for furniture) during the first days I arrived at Mines. Let me also say "thank you" to Michelle Szobody, Barbara McLenon, Sara Summers, Susan Venable, and Barbara Middlebrook for their wonderful help, whether it is faxing a few pages or showing me tips on the Latex.

I also wish to thank WesternGeco and ExxonMobil for taking me as an intern student, which not only gave me hands-on experience in seismic data processing, but also impressed me with their company culture.

Living and studying in a country with different culture from that of my home country turned out to be challenging and most beneficial to me. Thanks to all friends who helped me overcome my deficiency in English and, probably, communication skills. Finally, my deepest thanks go to my wife, Hanqiu, who has been a constant resource of support, and my lovely daughter, Yitian, who brings endless happiness.

Chapter 1

Introduction

1.1 Motivation

Most existing publications on seismic anisotropy are devoted to the influence of angular velocity variation on the traveltimes and amplitudes of seismic waves (e.g., Backus, 1962; Thomsen, 1986; Alford, 1986; Alkhalifah and Tsvankin, 1995; Bakulin et al., 2000a,b,c; Grechka and Tsvankin, 2002a,b; Wang, 2002; Upadhyay, 2004; Tsvankin, 2005; Crampin and Peacock, 2005; Helbig and Thomsen, 2005). It is likely, however, that anisotropic formations are also characterized by directionally dependent attenuation, which is possibly related to the internal structure of the rock matrix or the presence of aligned fractures or pores.

It has long been recognized that attenuation, a process that dissipates the energy of elastic waves and alters their amplitude and frequency content, is prevalent in the earth. Application of attenuation in seismic exploration, however, remains a challenging topic. One important reason is the uncertainty associated with attenuation measurements (e.g., Schoenberg and Levin, 1974; Kibblewhite, 1989; Mateeva, 2003; King, 2005). As pointed out by Leon Thomsen (cited from Lynn et al., 1999), while attenuation itself is difficult to estimate, the azimuthal variation in attenuation might be more tractable. Indeed, the directional dependence of attenuation has been measured in laboratory experiments (e.g., Johnston, 1981; Hosten et al., 1987; Tao and King, 1990; Best, 1994; Prasad and Nur, 2003) and several field case studies (e.g., Liu et al., 1993; Hiramatsu, 1995; Lynn et al., 1999; Vasconcelos and Jenner, 2005).

The physical mechanism of attenuation remains an active field of research (Biot, 1956, 1962; White, 1975; Dvorkin et al., 1995; King, 2005), and several mechanisms have been proposed for attenuation anisotropy. For example, fluid flow in fractured and porous media is usually considered the dominant mechanism of anisotropic dissipation (Mavko and Nur, 1979; Akbar et al., 1993; Parra, 1997; Brajanovski et al., 2005). MacBeth (1999) reviews some intrinsic attenuation mechanisms, such as intracrack fluid flow, and attributes the azimuthal variation of P-wave reflection amplitudes to anisotropic attenuation. Pointer et al. (2000) discuss three different models of wave-induced fluid flow in cracked porous media, which may result in anisotropic velocities and attenuation coefficients when the cracks are aligned. A poroelastic model introduced by Chapman (2003) in his discussion of frequency-dependent anisotropy can explain strong anisotropic attenuation in the seismic frequency band. Using Chapman's model, Maultzsch et al. (2003a) estimated the quality factor Q (a commonly used parameter for attenuation measurement) as a function of phase

angle for synthetic samples composed of sand-epoxy matrix with embedded thin metal discs.

Attenuation anisotropy can also be caused by directionally-dependent stress (e.g., Stanley and Christensen, 2001; Prasad and Nur, 2003). For example, Liu et al. (1993) estimated anisotropy in both velocity and attenuation for a shallow multiazimuth reverse VSP survey, and attributed it to stress-induced fractures and microcracks. Analysis of seismic body waves and normal-mode data shows that even the inner core of the earth possesses attenuation anisotropy that may be caused by columnar crystals elongated in the radial direction (Souriau and Romanowicz, 1996; Bergman, 1997). Other possible causes of attenuation anisotropy may include interbedding of thin attenuative layers (e.g., Carcione, 1992; Molotkov and Bakulin, 1998), anisotropy of the density tensor in poroelastic Biot media (Bakulin and Molotkov, 1998), and azimuthal scattering (Willis et al., 2004).

A problem of significant interest is how we can benefit from studying attenuation anisotropy. Johnston and Toksöz (1981) suggest that seismic attenuation data can at least double the information obtained from velocities alone. Blangy (1994) speculates that anisotropic attenuation may help answer some of the unexplained pitfalls in AVO (amplitude variation with offset) interpretation. Maultzsch et al. (2003b) compare various overburden effects and suggest that the influence of anisotropic attenuation on the amplitude is of the same order as that of reflection coefficients. Hence anisotropic attenuation needs to be corrected in AVO analysis.

Although inferring rock properties (e.g., the fracture density) from anisotropic attenuation suffers from uncertainty caused by the large number of parameters and relies heavily on specific models, attenuation anisotropy complements other physical measurements, such as velocity anisotropy, and carries information about permeability and other parameters (Martin and Brown, 1995; Lynn and Beckham, 1998). For example, based on Biot's (1956, 1962) theory, Gelinsky and Shapiro (1994) found that fluid flow in media with anisotropic permeability results in stronger anisotropy for attenuation than that for velocity in the seismic frequency range.

Current literature on anisotropic attenuation generally falls into two categories: measurements and physical mechanisms. Measurements of attenuation in the laboratory or field are generally carried out for a few directions (e.g., two orthogonal directions) to describe (qualitatively) the directional dependence of attenuation. This, however, does not provide a full description of the directional dependence of attenuation and may cause errors even in estimating the principal direction of attenuation. On the other hand, discussions of possible mechanisms of anisotropic attenuation are primarily limited to a specific model, such as intracrack fluid flow (MacBeth, 1999).

The goal of this thesis is to develop a consistent treatment of attenuation anisotropy in the presence of velocity anisotropy. Without attempting to address specific mechanisms of anisotropic attenuation for fractured and porous media, I characterize attenuation anisotropy at the macroscopic level to design a set of attenuation-anisotropy parameters that govern attenuation coefficients. One of the main challenges in describing wave propagation in attenuative anisotropic media is the large number of parameters that control the attenuation coefficients because of the coupling between the real and imaginary parts of the stiffness matrix. I show, however, that attenuation anisotropy is to some extent analogous

to the corresponding velocity anisotropy (within the assumptions discussed below), and this can be used to facilitate the description of attenuation anisotropy.

1.2 Assumptions

An important assumption of this work is a constant quality factor Q in the operational frequency band. For frequency-dependent Q , the velocity- and attenuation-anisotropy parameters also become functions of frequency.

For plane waves propagating in attenuative media, the orientations of the real and imaginary parts of the wave vector generally differ from one another. This means that the planes of constant phase and constant amplitude do not coincide (Borcherdt and Wennerberg, 1985; Borcherdt et al., 1986; Krebes and Slawinski, 1991; Krebes and Le, 1994), and the direction of wave propagation deviates from the direction of maximum attenuation. However, when the wavefield is excited by a point source in a weakly attenuative homogeneous medium, the angle between the real and imaginary parts of the wave vector (the so-called *inhomogeneity angle*) is usually small, and the rate of attenuation is highest close to the propagation direction (Ben-Menahem and Singh, 1981; Červený and Pšenčík, 2005). In Chapters 2–4, I consider *homogeneous wave propagation* in attenuative media, which means that the real and the imaginary parts of the wave vector are parallel to each other. Chapters 5 and 6, however, give a more general treatment of wave propagation that takes the inhomogeneity angle into account.

Another important assumption in Chapters 2–3 is the alignment of the symmetry directions of the velocity and attenuation anisotropy. For example, Chapter 2 discusses media with VTI (transversely isotropic with a vertical symmetry axis) symmetry for both velocity and attenuation. Chapter 5 shows, however, that the effective velocity and attenuation functions for layered attenuative HTI (TI with a horizontal symmetry axis) media may have different symmetry orientations. Analysis of seismic-source radiation in Chapter 6 is valid for general attenuative anisotropic media with different symmetries for velocity and attenuation.

Most analytic results in Chapters 2–6 are derived for models with weak attenuation as well as weak anisotropy for both velocity and attenuation.

To make the assumptions clear, they are reiterated in appropriate places throughout the thesis.

1.3 Thesis layout

In addition to the introduction and conclusions, the thesis consists of five chapters on various aspects of attenuation anisotropy: attenuation analysis for TI media, generalization of the TI results for orthorhombic media, laboratory measurements of P-wave TI attenuation, effective attenuation anisotropy of finely layered media, and far-field radiation in 2D attenuative anisotropic media.

Chapter 2 gives a consistent analytic treatment of plane-wave propagation for attenuative TI media (i.e., both velocity and attenuation have TI symmetry). Extending Thomsen's

(1986) notation for velocity anisotropy, I suggest defining attenuation anisotropy using two reference isotropic quantities (wavenumber-normalized attenuation coefficients for P- and SV-waves along the symmetry axis) plus three attenuation-anisotropy parameters (ϵ_Q , δ_Q , and γ_Q). These attenuation parameters, in combination with the reference isotropic quantities for P- and SV-velocities along the symmetry axis (V_{P0} and V_{S0} , respectively) and three velocity-anisotropy parameters (ϵ , δ , and γ), fully characterize the attenuation of P-, SV- and SH-waves. Moreover, the Thomsen-style attenuation-anisotropy parameters can be used to linearize attenuation coefficients under the assumptions of weak attenuation and weak velocity and attenuation anisotropy. The approximate attenuation coefficients reveal a close similarity between velocity and attenuation anisotropy.

Chapter 3 is an extension of the results obtained for TI symmetry to orthorhombic media. By using the analogy between velocity and attenuation, as well as the analogous form of the Christoffel equation in TI media and the symmetry planes of orthorhombic media, I follow Tsvankin's (1997, 2005) notation to develop a set of anisotropy parameters for orthorhombic attenuation. This parameterization is then used to linearize the P-wave attenuation coefficients in the limit of weak attenuation as well as weak velocity and attenuation anisotropy. The reduction in the number of attenuation-anisotropy parameters governing P-wave attenuation provides a basis for processing P-wave attenuation measurements from orthorhombic media.

Chapter 4 describes laboratory measurements of P-wave attenuation anisotropy for a synthetic sample. To estimate the complete angular dependence of attenuation, I suggest an anisotropic version of the spectral-ratio method, which takes into account the difference between the attenuation coefficients in the phase and group directions. Despite a number of limitations in the measurements and analysis, this methodology can be applied to processing of field data (e.g., AVO analysis) for attenuative anisotropic media.

To understand the physical reasons for attenuation anisotropy, I analyze the effective parameters of finely layered attenuative media in the long-wavelength limit (Chapter 5). Linearization of the effective attenuation-anisotropy parameters for TI constituent layers provides physical insight into the relative influence of heterogeneity versus intrinsic velocity and attenuation anisotropy. If the model includes azimuthally anisotropic layers with misaligned vertical symmetry planes, the effective velocity and attenuation may have different symmetries and principal azimuthal directions.

The discussion in Chapters 2–4 is based on the assumption of homogeneous wave propagation. In Chapter 6, I study the influence of the inhomogeneity angle on attenuation behavior, such as the radiation patterns for homogeneous attenuative media. By evaluating 2D far-field (asymptotic) radiation from seismic sources, I find that the inhomogeneity angle is governed by both velocity and attenuation anisotropy and vanishes in symmetry directions. The relationship between the group and phase attenuation coefficients is influenced by the inhomogeneity angle, which can have serious implications for field measurements and AVO analysis of attenuative anisotropic media.

Chapter 2

Plane-wave attenuation anisotropy for TI media

2.1 Summary

I develop a consistent analytic treatment of plane-wave properties for TI media with attenuation anisotropy. The anisotropic quality factor can be described by matrix elements Q_{ij} defined as the ratios of the real and imaginary parts of the corresponding stiffness coefficients. To characterize TI attenuation, I follow the idea of Thomsen's notation for velocity anisotropy and replace the components Q_{ij} by two reference isotropic quantities and three dimensionless anisotropic parameters ϵ_Q , δ_Q , and γ_Q . The parameters ϵ_Q and γ_Q quantify the difference between the horizontal and vertical attenuation coefficients for P- and SH-waves (respectively), while δ_Q is defined through the second derivative of the P-wave attenuation coefficient in the symmetry direction. Although the definitions of ϵ_Q , δ_Q , and γ_Q are similar to those for the corresponding Thomsen parameters, significantly, the expression for δ_Q reflects the coupling between the attenuation and velocity anisotropy.

Assuming weak attenuation as well as weak velocity and attenuation anisotropy helps to obtain simple attenuation coefficients linearized in Thomsen-style parameters. The normalized attenuation coefficients for both P- and SV-waves have the same form as do the corresponding approximate phase-velocity functions, but both δ_Q and the effective SV-wave attenuation-anisotropy parameter σ_Q depend on the velocity-anisotropy parameters in addition to the elements Q_{ij} . The linearized approximations not only provide valuable analytic insight, they also remain accurate for the practical and important range of small and moderate anisotropy parameters, in particular for near-vertical and near-horizontal propagation directions.

2.2 Introduction

This chapter is devoted to plane-wave signatures in TI media with both isotropic and TI attenuation. Although waves propagating through attenuative media are generally inhomogeneous (i.e., the orientations of the real and the imaginary parts of the wave vector differ from one another), the inhomogeneity angle is usually small for the wavefield excited by a point source in a weakly attenuative homogeneous medium. Here, I show that as long as the inhomogeneity angle is of the same order as the velocity-anisotropy and attenuation-anisotropy parameters, the misalignment of the real and imaginary parts of the wave vector has negligible influence on the attenuation coefficient. Therefore, in most of the discussion below the real and imaginary parts of the wave vector are taken to be parallel to one another,

which corresponds to homogeneous wave propagation.

A detailed discussion of wave propagation in anisotropic attenuative media is given by Carcione (2001). His treatment, however, is formulated in terms of the stiffness coefficients, and the results are not generally expressed in a form amenable to data-processing applications. As demonstrated below, analysis of the influence of anisotropic attenuation on seismic signatures can be facilitated by introducing dimensionless anisotropic parameters responsible for the angle-dependent quality factor.

After defining the quality-factor elements Q_{ij} through the ratios of the real and imaginary parts of the stiffness coefficients, I introduce Thomsen-style parameters that describe the angle-dependent attenuation. The advantages of this notation are demonstrated by analyzing the attenuation coefficient as a function of phase angle. To gain insight into the behavior of the attenuation coefficients for P- and SV-waves, I simplify the exact equations under the assumptions that the attenuation and velocity anisotropy, as well as the attenuation itself, are weak. The accuracy of the approximate attenuation coefficients is verified by numerical tests for representative TI models.

The terminology in this chapter is designed to draw a clear distinction between the anisotropy of velocity and attenuation. To ensure consistency with existing literature on non-attenuative anisotropic media, terms such as *anisotropic media* or *transversely isotropic (TI) media* refer to the velocity anisotropy. When discussing attenuative media, I explicitly specify the character of the attenuation. For example, the term *TI medium with isotropic attenuation* means that the model is transversely isotropic with respect to the velocity function but the attenuation is isotropic (i.e., independent of direction).

2.3 Definition of the Q matrix

Although a number of parameters have been introduced to quantify attenuation-related amplitude decay (e.g., Johnston and Toksöz, 1981), such as the quality factor Q , attenuation coefficient, logarithmic decrement of amplitude, and complex modulus, these parameters were originally designed for isotropic attenuation and need to be generalized for anisotropic materials. To develop a consistent description of the quality factor for both isotropic and anisotropic attenuation, I follow Carcione (2001, p. 58) in defining Q as twice the time-averaged strain-energy density divided by the time-averaged dissipated-energy density. In terms of the complex stiffness coefficients, the quality-factor matrix is given by

$$Q_{ij} \equiv \frac{c_{ij}}{c_{ij}^I}, \quad (2.1)$$

where c_{ij} and c_{ij}^I are the real and the imaginary parts, respectively, of the stiffness coefficient $\tilde{c}_{ij} = c_{ij} + ic_{ij}^I$. Note that there is no summation over i or j in equation 2.1.

The analysis below is restricted to transversely isotropic media with either isotropic or TI attenuation. The symmetry axis is assumed to be vertical (VTI), but since all results are derived for a homogeneous medium, they can be readily adapted to TI models with any symmetry-axis orientation.

As follows from equation 2.1, the \mathbf{Q} matrix inherits the structure of the stiffness matrix. For the case of VTI media with VTI attenuation, the matrices c_{ij} and c_{ij}^I have the same (VTI) symmetry, and the quality-factor matrix has the form

$$\mathbf{Q} = \begin{bmatrix} Q_{11} & Q_{12} & Q_{13} & 0 & 0 & 0 \\ Q_{12} & Q_{11} & Q_{13} & 0 & 0 & 0 \\ Q_{13} & Q_{13} & Q_{33} & 0 & 0 & 0 \\ 0 & 0 & 0 & Q_{55} & 0 & 0 \\ 0 & 0 & 0 & 0 & Q_{55} & 0 \\ 0 & 0 & 0 & 0 & 0 & Q_{66} \end{bmatrix}, \quad (2.2)$$

where $Q_{12} = Q_{11} \frac{c_{11} - 2c_{66}}{c_{11} - 2c_{66} Q_{11}/Q_{66}}$.

When both the real and imaginary parts of the stiffness matrix have isotropic structure, the quality factor is described by only two independent parameters, Q_{33} and Q_{55} :

$$\mathbf{Q} = \begin{bmatrix} Q_{33} & Q_{13} & Q_{13} & 0 & 0 & 0 \\ Q_{13} & Q_{33} & Q_{13} & 0 & 0 & 0 \\ Q_{13} & Q_{13} & Q_{33} & 0 & 0 & 0 \\ 0 & 0 & 0 & Q_{55} & 0 & 0 \\ 0 & 0 & 0 & 0 & Q_{55} & 0 \\ 0 & 0 & 0 & 0 & 0 & Q_{55} \end{bmatrix}, \quad (2.3)$$

where the component $Q_{13} = Q_{12}$ is given as $Q_{13} = Q_{33} \frac{c_{33} - 2c_{55}}{c_{33} - 2c_{55} Q_{33}/Q_{55}}$. The P-wave attenuation is controlled by Q_{33} , while Q_{55} is responsible for the SV-wave attenuation (see below).

According to the attenuation measurements in sandstones by (Gautam et al., 2003), the Q factor for P-waves may be either larger or smaller than that for SV-waves, depending on the mobility of fluids in the rock. The ‘‘crossover’’ frequency, for which $Q_{33} = Q_{55}$, corresponds to the special case when all components of the \mathbf{Q} matrix are identical:

$$Q_{ij} = Q. \quad (2.4)$$

As discussed below, if the quality factor is given by equation 2.4, the attenuation for both P- and S-waves is isotropic (independent of direction), even for arbitrarily anisotropic media.

Anisotropic attenuation can be described by calculating the so-called *eigenstiffnesses* from the c_{ij} matrix and applying relaxation functions to the eigenstiffnesses to obtain the complex stiffness coefficients \tilde{c}_{ij} and the \mathbf{Q} matrix (Helbig, 1994). For TI media, those operations are described in detail by Carcione (2001, Chapter 4). Here, I do not consider any specific attenuation mechanism and focus on examining wave propagation for general TI structure of the \mathbf{Q} matrix.

The discussion below is based on the assumption of a frequency-independent Q , which is often valid in the seismic frequency band. In a more rigorous description of attenuation, the complex stiffness components and the quality factor vary with frequency, as does

the velocity. The results, however, can still be applied for any given frequency, and the Thomsen-style anisotropy coefficients become frequency-dependent.

2.3.1 Christoffel equation for anisotropic, attenuative media

The displacement of a harmonic plane wave in an attenuative medium can be written as

$$\tilde{\mathbf{u}} = \tilde{\mathbf{U}} \exp \left[i(\omega t - \tilde{\mathbf{k}} \cdot \mathbf{x}) \right], \quad (2.5)$$

where $\tilde{\mathbf{U}}$ denotes the polarization vector, ω is the angular frequency, t is the time, and $\tilde{\mathbf{k}}$ is the wave vector, which becomes complex in the presence of attenuation: $\tilde{\mathbf{k}} = \mathbf{k} - i\mathbf{k}^I$. The imaginary part (\mathbf{k}^I) of the wave vector is sometimes called the *attenuation vector*. In general, the wave propagation is inhomogeneous since \mathbf{k}^I is not parallel to \mathbf{k} , which means that the planes of constant phase and constant amplitude do not coincide, and the direction of the fastest amplitude decay deviates from the phase-velocity vector. The angle between \mathbf{k}^I and \mathbf{k} is the inhomogeneity angle.

While the inhomogeneity angle is a free parameter in plane-wave propagation, for wavefields excited by point sources in weakly attenuative media, the angle between the direction of \mathbf{k}^I and that of \mathbf{k} is usually small (Ben-Menahem and Singh, 1981). As discussed in Appendices A and B, if the inhomogeneity angle is of the same order as the velocity-anisotropy and attenuation-anisotropy parameters, the deviation of \mathbf{k}^I from \mathbf{k} has a negligibly small influence on both the attenuation coefficient and phase velocity. Hence, the treatment of plane waves is restricted to homogeneous wave propagation, for which the vectors \mathbf{k} and \mathbf{k}^I are parallel to one another so that $\tilde{\mathbf{k}} = \mathbf{n}(k - ik^I)$, where \mathbf{n} is the unit vector in the phase direction, $k = |\mathbf{k}|$, and $k^I = |\mathbf{k}^I|$.

By substituting the plane wave (equation 2.5) into the equation of motion, I obtain the Christoffel equation, which has the same form as that in non-attenuative media (e.g., Crampin, 1981):

$$\left[\tilde{G}_{ik} - \rho \tilde{V}^2 \delta_{ik} \right] \tilde{U}_k = 0. \quad (2.6)$$

Here, $\tilde{G}_{ik} = \tilde{c}_{ijkl} n_j n_l$ is the Christoffel matrix, which depends on the complex stiffnesses \tilde{c}_{ijkl} and the phase direction \mathbf{n} , ρ is the density, δ_{ik} is Kronecker's delta function, and $\tilde{V} = \frac{\omega}{\tilde{k}}$ is the complex phase velocity ($\tilde{k} = |\tilde{\mathbf{k}}|$). The real part V of the phase velocity is given by (Carcione, 2001)

$$V = \left[\text{Re} \left(\frac{1}{\tilde{V}} \right) \right]^{-1} = \frac{\omega}{k}. \quad (2.7)$$

Below I examine the solutions of the Christoffel equation 2.6 for all three wave types (P, SV, SH) in VTI media with both isotropic and VTI attenuation.

2.4 SH-wave attenuation

2.4.1 Isotropic attenuation

For waves propagating in the $[x_1, x_3]$ -plane of VTI media, the Christoffel equation 2.6 splits into an equation for the SH-wave polarized in the x_2 -direction and two coupled equations for the in-plane polarized P- and SV-waves. The equation for the wave vector of the SH-wave has the same form as that in non-attenuative media but the stiffness coefficients and wavenumbers are complex quantities:

$$\tilde{c}_{66}\tilde{k}_1^2 + \tilde{c}_{55}\tilde{k}_3^2 - \rho\omega^2 = 0. \quad (2.8)$$

As shown in Appendix A, for homogeneous wave propagation in a medium with isotropic Q ($Q = Q_{55} = Q_{66}$), the imaginary part of equation 2.8 reduces to

$$\mathcal{K}_2 \equiv \frac{k^2 - (k^I)^2}{Q} - 2kk^I = 0. \quad (2.9)$$

Note that the assumption of isotropic Q for SH-waves does not involve the condition $Q_{33} = Q_{55}$. Solving for k^I , I find [also see equation 2.122 in Carcione (2001)]

$$k^I = k \left(\sqrt{1 + Q^2} - Q \right). \quad (2.10)$$

It is convenient to introduce the *normalized attenuation coefficient* \mathcal{A} , which defines the rate of amplitude decay per wavelength:

$$\mathcal{A} \equiv \frac{k^I}{k}. \quad (2.11)$$

For brevity, the word *normalized* is omitted in most of the text below. Equation 2.10 shows that the coefficient \mathcal{A} for SH-waves in media with isotropic Q is independent of the phase angle. When attenuation is weak (i.e., $\frac{1}{Q} \ll 1$), equation 2.10 yields

$$\mathcal{A}_{SH} = \frac{1}{2Q}. \quad (2.12)$$

The weak-attenuation approximation (equation 2.12) is close to the exact attenuation coefficient \mathcal{A} for the practically important range $Q > 10$ and breaks down only for strongly attenuative media (Figure 2.1).

The real part of the Christoffel equation 2.8 can be used to obtain the phase velocity of the SH-wave (Appendix A):

$$V_{SH}(\theta) = \xi_Q V_{SH}^{\text{elast}}(\theta), \quad (2.13)$$

where V_{SH}^{elast} is the SH-wave phase velocity in the reference non-attenuative medium (equa-

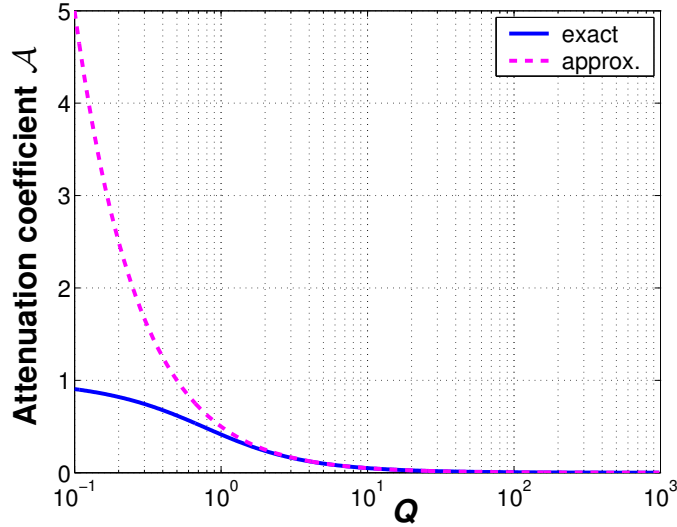


Figure 2.1. Normalized attenuation coefficient \mathcal{A} for SH-waves as a function of the Q factor for a medium with $Q_{55} = Q_{66} = Q$. The solid line is the exact \mathcal{A} from equations 2.10 and 2.11; the dashed line is the weak-attenuation approximation (equation 2.12).

tion A.15) and ξ_Q is given in equation A.19. In the limit of weak attenuation, the phase velocity becomes

$$V_{SH}(\theta) = V_{SH}^{\text{elast}}(\theta) \left(1 + \frac{1}{2Q^2} \right). \quad (2.14)$$

For a realistic range of Q values, the influence of attenuation on the real part of the wavenumber and, therefore, on the phase velocity can be ignored. Even for strongly attenuative media with $Q = 5$, the contribution of the term $\frac{1}{2Q^2}$ in equation 2.14 is limited to 2% of the velocity V_{SH} . Attenuation, however, causes velocity dispersion that is not always negligible even in the seismic frequency band.

2.4.2 VTI attenuation

Since the real and imaginary parts of the wave vector are coupled in the Christoffel equation, the directional dependence of the attenuation is influenced by the velocity anisotropy of the material. The physical reasons for the attenuation and velocity anisotropy in TI media may be similar. For example, preferential orientation of clay platelets in shales may be responsible not just for the velocity anisotropy (Sayers, 1994), but also for the attenuation anisotropy. Therefore, it is reasonable to assume that the symmetry of the attenuation in TI media is the same as that of the phase velocity. Furthermore, through-

out this chapter the symmetry axes of the attenuation coefficient and velocity function are taken to be parallel to one another, which results in the general VTI form of the \mathbf{Q} matrix in equation 2.2.

The Christoffel equation 2.8 yields the following relationship between the real and the imaginary SH-wavenumbers (Appendix A):

$$k^2 - (k^I)^2 - 2Q_{55} \alpha k k^I = 0, \quad (2.15)$$

where

$$\alpha \equiv \frac{(1 + 2\gamma) \sin^2 \theta + \cos^2 \theta}{(1 + 2\gamma) \frac{Q_{55}}{Q_{66}} \sin^2 \theta + \cos^2 \theta}, \quad (2.16)$$

and $\gamma \equiv (c_{66} - c_{55})/(2c_{55})$ is Thomsen's velocity-anisotropy parameter for SH-waves. Equation 2.16 is equivalent to equation 35 in Krebes and Le (1994). Solving equation 2.15 for k^I , I find the SH-wave attenuation coefficient,

$$\mathcal{A}_{SH} \equiv \frac{k^I}{k} = \sqrt{1 + (Q_{55} \alpha)^2} - Q_{55} \alpha. \quad (2.17)$$

In the weak-attenuation limit, equation 2.17 reduces to

$$\mathcal{A}_{SH} = \frac{1}{2Q_{55} \alpha}. \quad (2.18)$$

Equation 2.18 shows that Q_{55} is multiplied with the directionally-dependent parameter α to form the effective quality factor for the SH-wave, $Q_{55}^{\text{eff}} = Q_{55} \alpha$. At vertical incidence ($\theta = 0^\circ$), $\alpha = 1$ and $\mathcal{A}_{SH} = \frac{1}{2Q_{55}}$. In the horizontal direction ($\theta = 90^\circ$), $\alpha = \frac{Q_{66}}{Q_{55}}$ and $\mathcal{A}_{SH} = \frac{1}{2Q_{66}}$. For intermediate propagation directions, α reflects the coupling between the SH-wave velocity-anisotropy parameter γ and the ratio of the elements Q_{55} and Q_{66} . The contribution of the ratio Q_{55}/Q_{66} in equation 2.16 is used below to define an attenuation-anisotropy parameter analogous to Thomsen's parameter γ .

2.5 P- and SV-wave attenuation

Because of the coupling between P- and SV-waves, the equations governing their velocity and attenuation are more complicated than those for SH-waves. While the complex wavenumbers for P- and SV-waves can be evaluated numerically from equations B.3 and B.4 in Appendix B, the expression for the imaginary wavenumber k^I is cumbersome. Therefore, here I employ approximate solutions to study the dependence of the attenuation coefficients of P- and SV-waves on the medium parameters.

If both the attenuation anisotropy and attenuation itself are weak, the coefficient \mathcal{A}

for both P- and SV-waves can be found as (see Appendix C)

$$\mathcal{A} = \frac{1}{2Q_{33}}(1 + \mathcal{H}), \quad (2.19)$$

where $\mathcal{H} \equiv \frac{\mathcal{H}_u}{\mathcal{H}_d}$,

$$\begin{aligned} \mathcal{H}_u &\equiv \left(c_{11} \sin^2 \theta \frac{Q_{33} - Q_{11}}{Q_{11}} + c_{55} \cos^2 \theta \frac{Q_{33} - Q_{55}}{Q_{55}} \right) (c_{55} \sin^2 \theta + c_{33} \cos^2 \theta - \rho V^2) \\ &+ c_{55} \sin^2 \theta \frac{Q_{33} - Q_{55}}{Q_{55}} (c_{11} \sin^2 \theta + c_{55} \cos^2 \theta - \rho V^2) \\ &- 2 \left(c_{13} \frac{Q_{33} - Q_{13}}{Q_{13}} + c_{55} \frac{Q_{33} - Q_{55}}{Q_{55}} \right) (c_{13} + c_{55}) \sin^2 \theta \cos^2 \theta, \end{aligned} \quad (2.20)$$

and

$$\mathcal{H}_d \equiv \rho V^2 [(c_{55} + c_{11}) \sin^2 \theta + (c_{33} + c_{55}) \cos^2 \theta - 2\rho V^2]. \quad (2.21)$$

The phase velocity V in equations 2.20 and 2.21 corresponds to either P- or SV-waves, depending on which attenuation coefficient is desired.

The parameter \mathcal{H} is responsible for the contribution of the attenuation anisotropy. For P-waves at vertical incidence ($\theta = 0^\circ$), $\mathcal{H} = 0$ and $\mathcal{A}_P = \frac{1}{2Q_{33}}$; For the horizontal direction ($\theta = 90^\circ$), $\mathcal{H} = \frac{Q_{33} - Q_{11}}{Q_{11}}$ and $\mathcal{A}_P = \frac{1}{2Q_{11}}$. Hence, the ratio $\frac{Q_{33} - Q_{11}}{Q_{11}}$ quantifies the fractional difference between the P-wave attenuation coefficients in the horizontal and the vertical directions and can be used to characterize the P-wave attenuation anisotropy (see the next section). If $\mathcal{H} = 0$ for all angles, then the P-wave attenuation is isotropic, and $\mathcal{A}_P = \frac{1}{2Q_{33}}$.

For SV-waves the value $\mathcal{H} = \frac{Q_{33} - Q_{55}}{Q_{55}}$ is the same for both the vertical and horizontal directions; the corresponding attenuation coefficient is $\mathcal{A}_{SV} = \frac{1}{2Q_{55}}$. Therefore, isotropic SV-wave attenuation implies that $\mathcal{H} = \frac{Q_{33} - Q_{55}}{Q_{55}}$ for the whole range of angles.

The high accuracy of the approximate solutions for \mathcal{A} is confirmed by the example in Figure 2.2 generated for a VTI medium with substantial attenuation (the smallest Q -value is 15). The model is elliptical for the velocity anisotropy since $\epsilon = \delta$, but the shape of the attenuation coefficients is strongly nonelliptical. The attenuation coefficients in Figure 2.2 were computed from equations 2.19–2.21 and then substituted into equation B.3 to estimate the real part of the wavenumber and calculate the slownesses. These approximations practically coincide with the exact solutions for both slowness and attenuation obtained by jointly solving equations B.3 and B.4. (For that reason, the exact curves are not plotted in Figure 2.2.) This test also demonstrates that the phase velocities are virtually unchanged

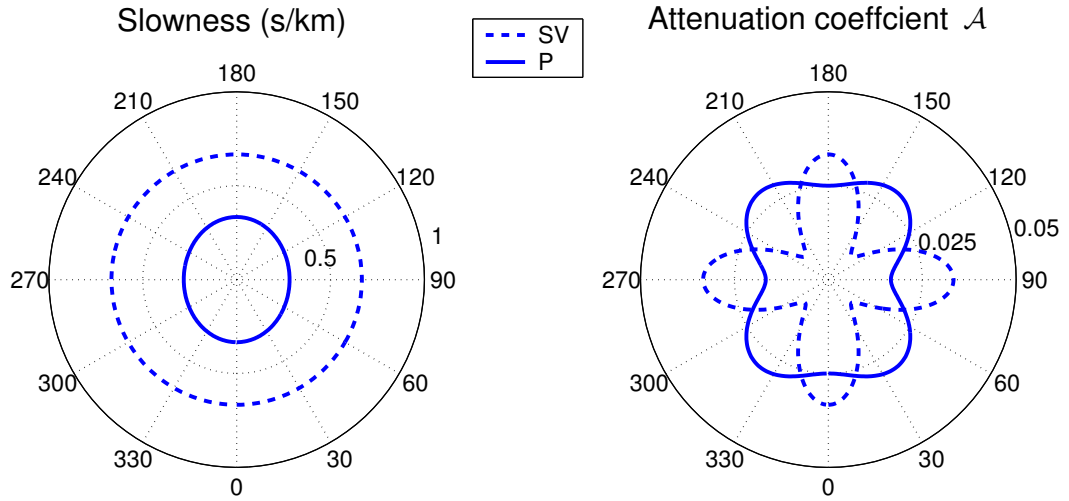


Figure 2.2. Slownesses (left) and attenuation coefficients \mathcal{A} (right) of P-waves (solid curves) and SV-waves (dashed) as functions of the phase angle with the symmetry axis (numbers on the perimeter). The coefficients \mathcal{A} were computed from the approximation (equation 2.19) and substituted into equation B.3 to obtain the slownesses. The approximations are almost indistinguishable from the exact solutions (not shown). The model parameters are $V_{P0}=3$ km/s, $V_{S0}=1.5$ km/s, $\epsilon = \delta = 0.2$, $Q_{11} = 30$, $Q_{33} = 20$, $Q_{13} = 15$, and $Q_{55} = 15$. (The Q components yield the attenuation-anisotropy parameters $\epsilon_Q = -0.33$ and $\delta_Q = 0.98$ defined in the section “Thomsen-style notation for VTI attenuation.”)

in the presence of moderate attenuation.

The approximate solution (equation 2.19) for \mathcal{A} remains accurate even for models with much more significant attenuation and uncommonly large values of the velocity-anisotropy parameters ϵ and δ (Figure 2.3). Note that in both the vertical ($\theta = 0^\circ$) and horizontal ($\theta = 90^\circ$) directions the attenuation is independent of ϵ or δ . However, the shape of the attenuation curves at intermediate angles varies with both ϵ and δ , especially when the velocity anisotropy is strong.

2.6 Thomsen-style notation for VTI attenuation

The description of seismic signatures in the presence of velocity anisotropy can be substantially simplified by using Thomsen (1986) notation. The advantages of Thomsen parameters in the analysis of seismic velocities and amplitudes for TI media are discussed in detail by Tsvankin (2001).

Here, I extend the principle of Thomsen notation to the directionally-dependent attenuation coefficient. The \mathbf{Q} matrix for models with VTI attenuation contains five independent elements, which can be replaced by two reference (isotropic) parameters and three dimen-

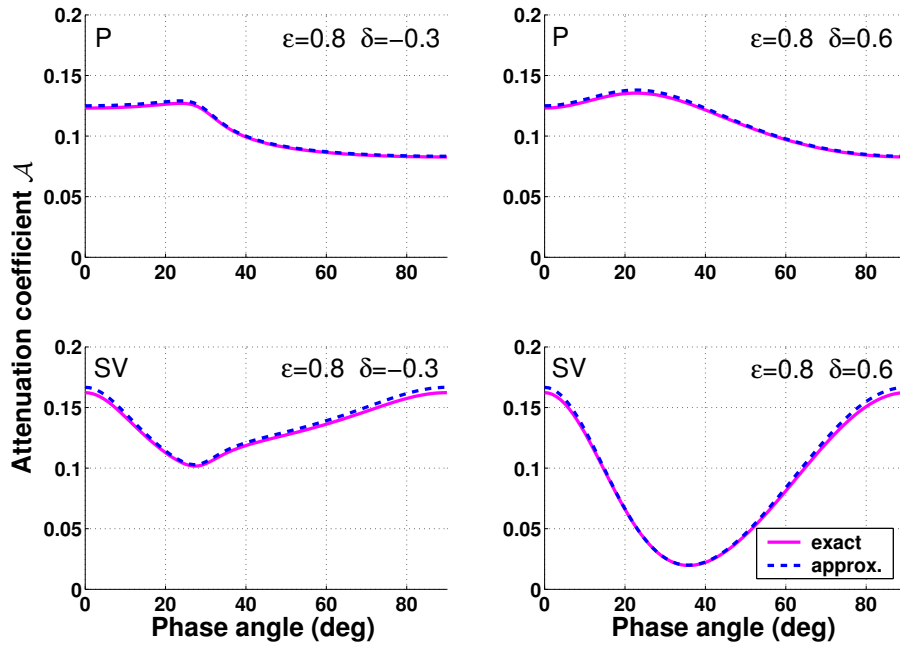


Figure 2.3. Normalized attenuation coefficients for P-waves (top row) and SV-waves (bottom row) computed for a strongly attenuative, strongly anisotropic medium. The solid curves are the exact solutions from equations B.3 and B.4, the dashed curves represent the approximation (equation 2.19). The pairs of the parameters ϵ and δ used in the tests are marked on the plots. The other model parameters are $V_{P0}=3$ km/s, $V_{S0}=1.5$ km/s, $Q_{11} = 4$, $Q_{33} = 3$, $Q_{13} = 2$, and $Q_{55} = 3$.

sionless coefficients (ϵ_Q , δ_Q , and γ_Q) responsible for the attenuation anisotropy. Since I operate with the attenuation coefficient, which is inversely proportional to the quality factor, the Thomsen-style parameters are convenient to define through quantities $\frac{1}{Q_{ij}}$. To maintain close similarity with Thomsen notation for velocity anisotropy and make our parameterization suitable for reflection data, I choose the P- and SV-wave attenuation coefficients in the symmetry (vertical) direction as the reference values:

$$\mathcal{A}_{P0} = Q_{33} \left(\sqrt{1 + 1/Q_{33}^2} - 1 \right) \approx \frac{1}{2Q_{33}}, \quad (2.22)$$

$$\mathcal{A}_{S0} = Q_{55} \left(\sqrt{1 + 1/Q_{55}^2} - 1 \right) \approx \frac{1}{2Q_{55}}. \quad (2.23)$$

The coefficient \mathcal{A}_{S0} is also responsible for the SH-wave attenuation in the symmetry (vertical) direction and the SV-wave attenuation in the isotropy plane. Note that the linearization of the square-roots in the above definitions (equations 2.22 and 2.23) produces approximate vertical attenuation coefficients accurate to first order in $1/Q_{ij}$.

2.6.1 SH-wave parameter γ_Q

The attenuation-anisotropy parameter γ_Q for SH-waves can be defined as the fractional difference between the attenuation coefficients in the horizontal and vertical directions (see equation 2.18):

$$\gamma_Q \equiv \frac{1/Q_{66} - 1/Q_{55}}{1/Q_{55}} = \frac{Q_{55} - Q_{66}}{Q_{66}}. \quad (2.24)$$

This definition is analogous to that of the Thomsen parameter γ , which is close to the fractional difference between the horizontal and vertical velocities of the SH-wave. The parameter γ_Q controls the magnitude of the SH-wave attenuation anisotropy; for isotropic Q , $\gamma_Q = 0$.

Substituting γ_Q into equation 2.16 for the parameter α yields

$$\alpha = \frac{(1 + 2\gamma) \sin^2 \theta + \cos^2 \theta}{(1 + 2\gamma)(1 + \gamma_Q) \sin^2 \theta + \cos^2 \theta}. \quad (2.25)$$

When both γ and γ_Q are small ($|\gamma| \ll 1$, $|\gamma_Q| \ll 1$), α can be linearized in these parameters:

$$\alpha = 1 - \gamma_Q \sin^2 \theta. \quad (2.26)$$

The attenuation coefficient from equation 2.18 then becomes independent of γ :

$$\mathcal{A}_{SH} = \mathcal{A}_{S0} (1 + \gamma_Q \sin^2 \theta), \quad (2.27)$$

where \mathcal{A}_{S0} is given in equation 2.23. Equation 2.27 has the same form as that of the SH-

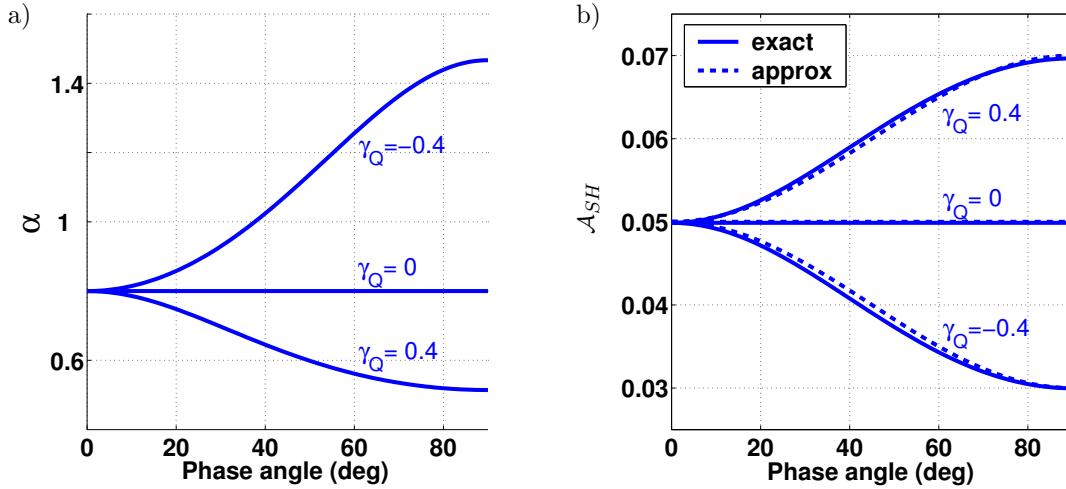


Figure 2.4. a) Factor α and b) SH-wave attenuation coefficient \mathcal{A}_{SH} for a medium with $\gamma = 0.1$, $Q_{55} = 10$, and γ_Q varying from -0.4 to 0.4. The exact \mathcal{A}_{SH} (solid line) is computed from equation 2.17, and the approximate \mathcal{A}_{SH} (dashed) from equation 2.27.

wave phase velocity linearized in the parameter γ (Thomsen, 1986). Note, however, that the *exact* phase velocity, unlike the exact attenuation coefficient, is described by a simple function of γ that corresponds to an elliptical slowness surface.

It is clear from equation 2.27 that γ_Q determines the sign and rate of the variation of $\mathcal{A}_{SH}(\theta)$ away from the vertical (symmetry) direction. When $\gamma_Q > 0$, the factor α decreases with the phase angle θ , which causes an increase in the attenuation coefficient (Figure 2.4). If the magnitude of the velocity anisotropy is small (i.e., $|\gamma| \ll 1$), the approximation (equation 2.27) gives an accurate estimate of the attenuation coefficient even for relatively large absolute values of γ_Q reaching 0.4 (Figure 2.4b).

2.6.2 P-SV wave parameters ϵ_Q and δ_Q

The attenuation-anisotropy parameter ϵ_Q can be defined by analogy with the Thomsen parameter ϵ as the fractional difference between the P-wave attenuation coefficients in the horizontal and vertical directions (see also Chichinina et al., 2004):

$$\epsilon_Q \equiv \frac{1/Q_{11} - 1/Q_{33}}{1/Q_{33}} = \frac{Q_{33} - Q_{11}}{Q_{11}}. \quad (2.28)$$

To complete the description of TI attenuation, I need to introduce a parameter similar to Thomsen's δ that involves the quality-factor component Q_{13} . It may seem that the definition of δ (Thomsen, 1986) can be adapted for attenuative media by simply replacing

the stiffnesses c_{ij} with $1/Q_{ij}$:

$$\hat{\delta}_Q \equiv \frac{(1/Q_{13} + 1/Q_{55})^2 - (1/Q_{33} - 1/Q_{55})^2}{2/Q_{33} (1/Q_{33} - 1/Q_{55})}. \quad (2.29)$$

The parameter $\hat{\delta}_Q$ from equation 2.29, however, is not physically meaningful. For example, when the attenuation is isotropic and $Q_{33} = Q_{55}$ (Gautam et al., 2003), the anisotropic parameters should vanish. Instead, $\hat{\delta}_Q$ for isotropic Q goes to infinity.

As discussed by Tsvankin (2001, see equation 1.49), the parameter δ proved to be extremely useful in describing signatures of reflected P-waves in VTI media because it determines the second derivative of the P-wave phase-velocity function in the vertical (symmetry) direction (the first derivative goes to zero). Therefore, the idea of Thomsen notation can be preserved by defining δ_Q through the second derivative of the P-wave attenuation coefficient \mathcal{A}_P at $\theta = 0$:

$$\delta_Q \equiv \frac{1}{2\mathcal{A}_{P0}} \left. \frac{d^2 \mathcal{A}_P}{d\theta^2} \right|_{\theta=0}. \quad (2.30)$$

In other words, the parameter δ_Q controls the curvature of the attenuation function $\mathcal{A}_P(\theta)$ in the vertical direction.

Assuming that both the attenuation and attenuation anisotropy are weak, I find the following explicit expression for δ_Q (Appendix C):

$$\delta_Q \equiv \frac{\frac{Q_{33} - Q_{55}}{Q_{55}} c_{55} \frac{(c_{13} + c_{33})^2}{(c_{33} - c_{55})} + 2 \frac{Q_{33} - Q_{13}}{Q_{13}} c_{13} (c_{13} + c_{55})}{c_{33} (c_{33} - c_{55})}. \quad (2.31)$$

The role of δ_Q in describing the P-wave attenuation anisotropy is similar to that of δ in the P-wave phase-velocity equation (Thomsen, 1986; Tsvankin, 2001). Since the first derivative of \mathcal{A}_P for $\theta = 0$ is equal to zero, δ_Q is responsible for the angular variation of the P-wave attenuation coefficient near the vertical direction.

In the special case of a purely isotropic (i.e., angle-independent) velocity function, δ_Q reduces to a weighted summation of the fractional differences $(Q_{33} - Q_{55})/Q_{55}$ and $(Q_{33} - Q_{13})/Q_{13}$:

$$\delta_Q = \frac{Q_{33} - Q_{55}}{Q_{55}} \frac{4\mu}{\lambda + 2\mu} + \frac{Q_{33} - Q_{13}}{Q_{13}} \frac{2\lambda}{\lambda + 2\mu}, \quad (2.32)$$

where λ and μ are the Lamé parameters.

Unless attenuation is uncommonly strong, the phase velocities of P- and SV-waves are close to those in the reference non-attenuative medium and do not depend on the attenuation parameters ϵ_Q and δ_Q . Equation 2.31 for the parameter δ_Q , however, indicates that the attenuation anisotropy is influenced by the velocity anisotropy. If I approximate

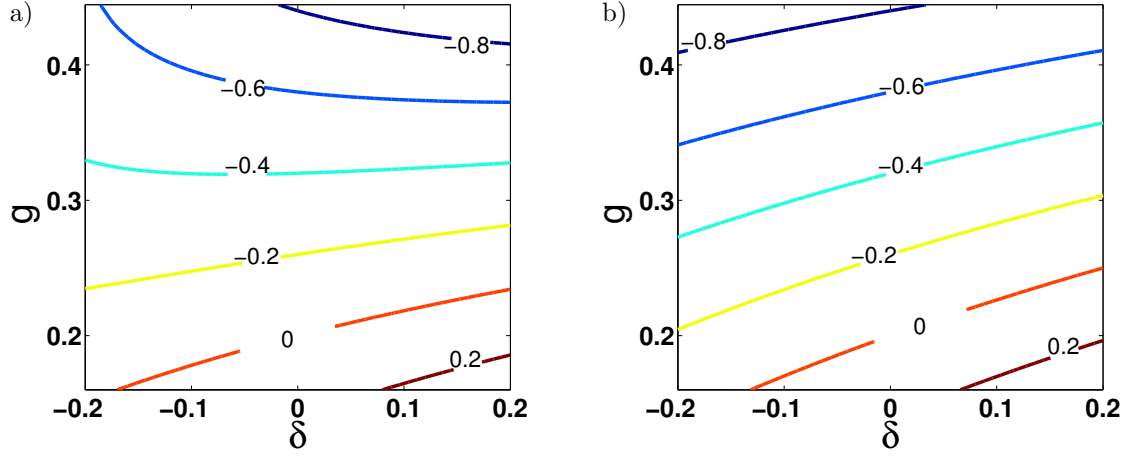


Figure 2.5. Contour plot of the parameter δ_Q as a function of δ and $g \equiv V_{S0}^2/V_{P0}^2$ computed from (a) equation 2.31, and (b) equation 2.35. The other parameters are $Q_{33} = 4$, $Q_{55} = 8$, and $Q_{13} = 3$. The range of g values corresponds to $1.5 < V_{P0}/V_{S0} < 2.5$.

$c_{13} \approx c_{33}(1 + \delta) - 2c_{55}$, which can be done for small $|\delta|$ (Tsvankin, 2001, p. 20), and denote

$$g \equiv \frac{V_{S0}^2}{V_{P0}^2} = \frac{c_{55}}{c_{33}}, \quad (2.33)$$

equation 2.31 for δ_Q can be rewritten as

$$\delta_Q = \frac{Q_{33} - Q_{55}}{Q_{55}} g \frac{(2 + \delta - 2g)^2}{(1 - g)^2} + \frac{Q_{33} - Q_{13}}{Q_{13}} \frac{2(1 + \delta - 2g)(1 + \delta - g)}{(1 - g)}. \quad (2.34)$$

Linearizing equation 2.34 in g under the assumption $g \ll 1$ leads to the following simplified expression:

$$\delta_Q = 4 \frac{Q_{33} - Q_{55}}{Q_{55}} g + 2 \frac{Q_{33} - Q_{13}}{Q_{13}} (1 + 2\delta - 2g). \quad (2.35)$$

Figure 2.5 shows an example of δ_Q as a function of δ and g . The parameters Q_{33} and Q_{55} are taken from the experimental results of (Gautam et al., 2003) for Rim sandstone at a frequency of 25 Hz, while Q_{13} is assigned an arbitrary value. With this choice of the Q components, the parameter δ_Q is quite sensitive to the squared velocity ratio g and reaches large negative values for hard rocks with $g > 0.35$. While the simplified equation 2.35 for δ_Q is sufficiently accurate for small magnitudes of both δ and g ($-0.1 < \delta < 0.2$ and $g < 0.2$), it produces a significant error for $g > 0.25$. Note that the absolute value of δ_Q may be large (even greater than unity).

In combination with the Thomsen parameters for the velocity function, the parameters \mathcal{A}_{P0} , \mathcal{A}_{S0} , ϵ_Q , δ_Q , and γ_Q fully characterize the attenuation of P-, SV- and SH-waves.

2.7 Approximate attenuation coefficients for P- and SV-waves

The exact equations for the P- and SV-wave attenuation coefficients are too cumbersome to be represented as explicit functions of the anisotropy-attenuation parameters introduced above. It is possible, however, to obtain relatively simple approximations for the coefficient \mathcal{A} by assuming simultaneously:

- 1) weak attenuation ($\frac{1}{Q_{ij}} \ll 1$);
- 2) weak attenuation anisotropy ($|\epsilon_Q| \ll 1$, $|\delta_Q| \ll 1$); and
- 3) weak velocity anisotropy ($|\epsilon| \ll 1$, $|\delta| \ll 1$).

Note that weak attenuation and weak attenuation anisotropy were already assumed in deriving the P- and SV-wave attenuation coefficients in equations 2.19–2.21.

2.7.1 Approximate P-wave attenuation

The approximate P-wave attenuation coefficient can be obtained from equation 2.19 by expressing the stiffnesses c_{ij} through the Thomsen parameters ϵ and δ , and the elements Q_{ij} through the attenuation parameters ϵ_Q and δ_Q introduced above. Dropping terms quadratic in ϵ , δ , ϵ_Q , and δ_Q yields the following linearized expression:

$$\mathcal{A}_P = \mathcal{A}_{P0} (1 + \delta_Q \sin^2 \theta \cos^2 \theta + \epsilon_Q \sin^4 \theta), \quad (2.36)$$

where \mathcal{A}_{P0} is defined in equation 2.22. The angle dependence of the approximate \mathcal{A}_P is governed by just the attenuation-anisotropy parameters ϵ_Q and δ_Q , although δ_Q itself contains a contribution of the velocity anisotropy. The parameter δ_Q is responsible for the attenuation coefficient in near-vertical directions, while ϵ_Q controls \mathcal{A}_P near the horizontal plane. If both ϵ_Q and δ_Q go to zero, the approximate coefficient \mathcal{A}_P becomes isotropic.

It is noteworthy that equation 2.36 has the same form as the well-known Thomsen's (1986) weak-anisotropy approximation for P-wave phase velocity:

$$V_P = V_{P0} (1 + \delta \sin^2 \theta \cos^2 \theta + \epsilon \sin^4 \theta). \quad (2.37)$$

To obtain attenuation-coefficient equation 2.36 from phase-velocity equation 2.37, one needs to make the following substitutions: $V_{P0} \rightarrow \mathcal{A}_{P0}$, $\epsilon \rightarrow \epsilon_Q$, and $\delta \rightarrow \delta_Q$.

2.7.2 Approximate SV-wave attenuation

The SV-wave attenuation coefficient is also obtained by linearizing equation 2.19:

$$\mathcal{A}_{SV} = \mathcal{A}_{S0} \frac{1 + \left(\frac{2\sigma}{g_Q} + \frac{\epsilon_Q - \delta_Q}{gg_Q} \right) \sin^2 \theta \cos^2 \theta}{1 + 2\sigma \sin^2 \theta \cos^2 \theta}, \quad (2.38)$$

where \mathcal{A}_{S0} and g are defined in equations 2.23 and 2.33, respectively, g_Q is given by

$$g_Q \equiv \frac{Q_{33}}{Q_{55}}, \quad (2.39)$$

and σ is the SV-wave velocity-anisotropy parameter (Tsvankin and Thomsen, 1994; Tsvankin 2001):

$$\sigma \equiv \frac{V_{P0}^2}{V_{S0}^2} (\epsilon - \delta) = \frac{\epsilon - \delta}{g}. \quad (2.40)$$

If $|\sigma| \ll 1$ and $\left| \frac{2\sigma}{g_Q} + \frac{\epsilon_Q - \delta_Q}{gg_Q} \right| \ll 1$, equation 2.38 can be further simplified to

$$\mathcal{A}_{SV} = \mathcal{A}_{S0} (1 + \sigma_Q \sin^2 \theta \cos^2 \theta), \quad (2.41)$$

with

$$\sigma_Q \equiv \frac{1}{g_Q} \left[2(1 - g_Q) \sigma + \frac{\epsilon_Q - \delta_Q}{g} \right]. \quad (2.42)$$

The parameter σ_Q determines the curvature of the SV-wave attenuation coefficient \mathcal{A}_{SV} in the symmetry direction. The form of equation 2.41 is identical to that of Thomsen's (1986) approximation for the SV-wave phase velocity in terms of the parameter σ . It should be emphasized that σ_Q is a function of both attenuation-anisotropy and velocity-anisotropy parameters. Depending on the sign of σ_Q , the coefficient \mathcal{A}_{SV} has either a maximum or a minimum at $\theta = 45^\circ$.

Note that the assumption $|\sigma| \ll 1$ used in deriving equation 2.41 might not be valid for many typical TI formations because σ often has a substantial magnitude even when $|\epsilon - \delta|$ is small.

2.7.3 Isotropic attenuation coefficients

According to the approximate expression 2.36, the normalized P-wave attenuation coefficient is isotropic (i.e., independent of angle) if

$$\epsilon_Q = \delta_Q = 0. \quad (2.43)$$

Similarly, the coefficient \mathcal{A}_{SV} for SV-waves (equation 2.41) is isotropic when $\sigma_Q = 0$, that is, when

$$\epsilon_Q - \delta_Q = -2(1 - g_Q)(\epsilon - \delta). \quad (2.44)$$

The coefficients \mathcal{A}_P and \mathcal{A}_{SV} are both isotropic when $\epsilon_Q = \delta_Q = 0$ and either 1) $g_Q = 1$ or 2) $\epsilon - \delta = 0$ (elliptical anisotropy). The condition $g_Q = 1$, combined with

$\epsilon_Q = \delta_Q = 0$, corresponds to the special case of identical Q components for P-SV waves,

$$Q_{11} = Q_{33} = Q_{13} = Q_{55}, \quad (2.45)$$

which yields isotropic normalized attenuation coefficients for P- and SV-waves in VTI media with arbitrary velocity anisotropy. (As discussed above, the normalized SH-wave attenuation coefficient is isotropic when $Q_{55} = Q_{66}$, i.e., $\gamma_Q = 0$). The second condition, however, is limited to the approximate attenuation coefficients, unless all anisotropy parameters for P- and SV-waves vanish ($\epsilon = \delta = \epsilon_Q = \delta_Q = 0$). Hence, when referring to “isotropic” attenuation in TI media, one ought to specify the type of plane wave.

The above discussion pertains to the normalized attenuation coefficient \mathcal{A} , which characterizes the rate of amplitude decay per wavelength. Alternatively, attenuation can be described by the imaginary wavenumber (i.e., the attenuation coefficient without normalization) denoted here as k^I . Since the wavelength in anisotropic media changes with direction, a model with a purely isotropic coefficient \mathcal{A} generally has an angle-dependent wavenumber k^I . The conditions that make k^I for all three modes isotropic are derived in Appendix D.

2.7.4 Numerical examples

The approximate P-wave attenuation coefficient (equation 2.36) does not contain the vertical shear-wave attenuation coefficient \mathcal{A}_{S0} . Although the linearized approximation becomes inaccurate with increasing magnitude of the anisotropy parameters, \mathcal{A}_P remains independent of \mathcal{A}_{S0} even for models with strong attenuation and pronounced velocity and attenuation anisotropy. As demonstrated in Figure 2.6a, the variation of the coefficient \mathcal{A}_P with \mathcal{A}_{S0} becomes noticeable only for extremely high attenuation (i.e., uncommonly small values of Q_{55}). Therefore, P-wave attenuation in VTI media is mainly governed by a reduced set of parameters: \mathcal{A}_{P0} , ϵ_Q , and δ_Q . Note that a similar result is valid for the P-wave phase-velocity function, which is practically independent of the shear-wave vertical velocity V_{S0} (Tsvankin and Thomsen, 1994; Tsvankin, 2001).

In contrast, SV-wave attenuation is strongly influenced by the vertical P-wave attenuation coefficient \mathcal{A}_{P0} through the parameter σ_Q (Figure 2.6b). Since σ_Q for this model is negative (for values of Q_{33} equal to 15, 35, and 300, the parameter σ_Q is -4.84, -2.93, and -1.66, respectively), further reduction in Q_{33} results in negative SV-wave attenuation coefficients, which should be considered unphysical.

The accuracy of the approximate solutions (equations 2.36, 2.38, and 2.41) is illustrated by the numerical tests in Figures 2.7–2.11. The P-wave attenuation coefficient in Figure 2.7 has an extremum (a maximum) at an angle slightly smaller than 45° because ϵ_Q and δ_Q have opposite signs. If the signs of ϵ_Q and δ_Q are the same, \mathcal{A}_P varies monotonically between the vertical and horizontal directions.

The curve of \mathcal{A}_{SV} has a concave shape because σ_Q in equation 2.41 is negative and large in absolute value. Both approximations (equations 2.38 and 2.41) predict a minimum of the SV-wave attenuation coefficient at $\theta = 45^\circ$. The extrema of the exact coefficients \mathcal{A} in Figure 2.7 (solid lines) for both P- and SV-waves, however, are somewhat shifted toward the vertical axis relative to their approximate positions.

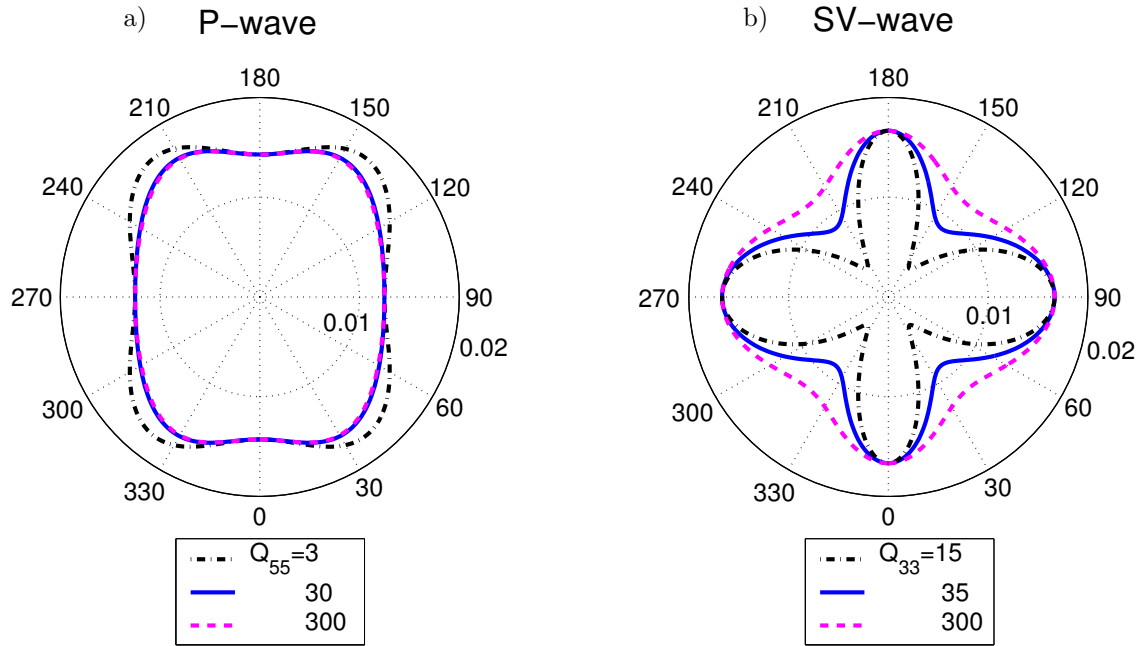


Figure 2.6. a) Influence of the parameter $\mathcal{A}_{S0} = 1/(2Q_{55})$ on the normalized P-wave attenuation coefficient; $\mathcal{A}_{P0} = 0.014$ ($Q_{33} = 35$). b) Influence of the parameter $\mathcal{A}_{P0} = 1/(2Q_{33})$ on the normalized SV-wave attenuation coefficient; $\mathcal{A}_{S0} = 0.017$ ($Q_{55} = 30$). The other model parameters on both plots are $V_{P0}=2.42$ km/s, $V_{S0}=1.4$ km/s, $\epsilon = 0.4$, $\delta = 0.15$, $\epsilon_Q = -0.125$, and $\delta_Q = 0.94$ (δ_Q is computed from equation 2.31).

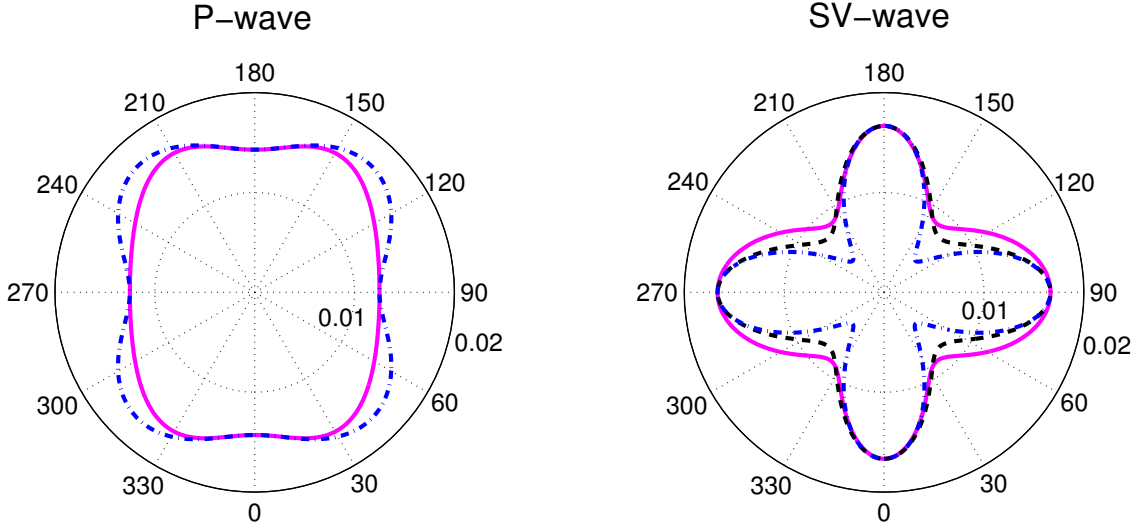


Figure 2.7. Attenuation coefficients of P-waves (left) and SV-waves (right) as functions of the phase angle. The solid curves are the exact values of \mathcal{A} obtained by jointly solving equations B.3 and B.4; the dash-dotted curves are the approximate coefficients from equations 2.36 and 2.41; the dashed curve on the right plot is the approximate SV-wave coefficient from equation 2.38. The model parameters are the same as in Figure 2.6, except for $Q_{33} = 35$ and $Q_{55} = 30$.

The linearized expressions for the attenuation coefficients give satisfactory results for near-vertical propagation directions with angles θ up to about 30° . The error becomes noticeable for intermediate angles $30^\circ < \theta < 75^\circ$ and then decreases again near the horizontal plane. Note that the velocity (see Figure 2.8) and attenuation anisotropy for the model from Figure 2.7 cannot be considered weak, and the values of $\sigma = 0.75$ and $\sigma_Q = -2.93$ are particularly large. Since equation 2.38 does not assume that the parameter σ and the term $\left(\frac{2\sigma}{g_Q} + \frac{\epsilon_Q - \delta_Q}{gg_Q}\right) = (2\sigma + \sigma_Q)$ are small in absolute value, it provides a better approximation for the SV-wave attenuation coefficient than does equation 2.41.

For models with smaller magnitudes of the anisotropy parameters (Figure 2.9), equations 2.36 and 2.41 become sufficiently accurate for the attenuation coefficients over the full range of phase angles. The numerical tests show that the error of the approximate solutions (equations 2.36, 2.38, and 2.41) is controlled primarily by the strength of the velocity anisotropy, even if the magnitude of the attenuation anisotropy is much higher.

Figure 2.10 displays the attenuation coefficients for a medium with $\epsilon_Q = \delta_Q = 0$. The approximate P-wave attenuation computed from equation 2.36 in this case is isotropic. The exact coefficient \mathcal{A}_P , however, slightly deviates from a circle, which indicates non-negligible influence of quadratic and higher-order terms in the parameters ϵ_Q and δ_Q . Also,

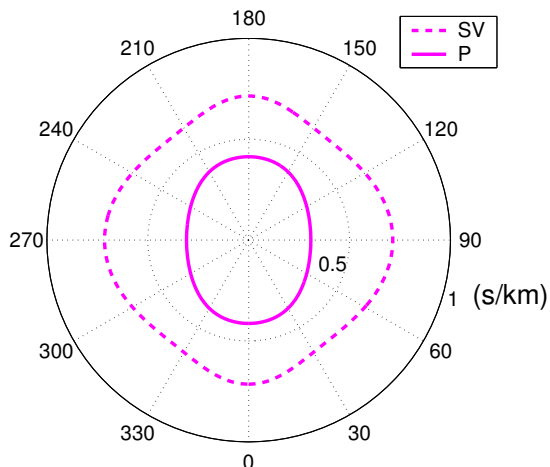


Figure 2.8. Slownesses of P- and SV-waves for the model from Figure 2.7.

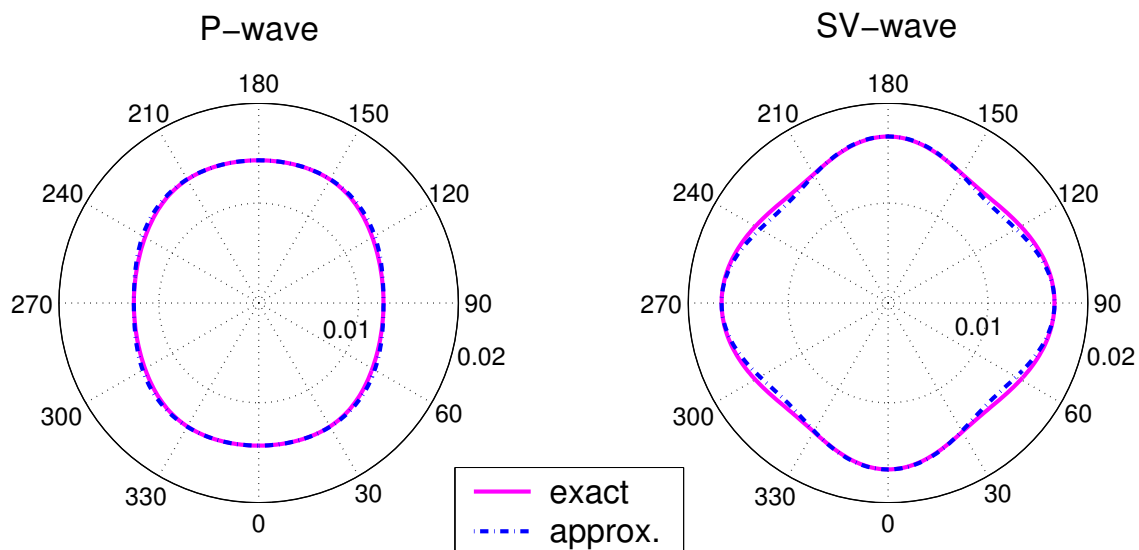


Figure 2.9. Attenuation coefficients of P-waves (left) and SV-waves (right) for $V_{P0}=2.42$ km/s, $V_{S0}=1.4$ km/s, $\epsilon = 0.125$, $\delta = -0.05$, $Q_{33} = 35$, $Q_{55} = 30$, $\epsilon_Q = -0.125$, and $\delta_Q = 0.05$. The solid curves are the exact values of \mathcal{A} obtained by jointly solving equations B.3 and B.4; the dash-dotted curves are the approximate coefficients from equations 2.36 and 2.41.

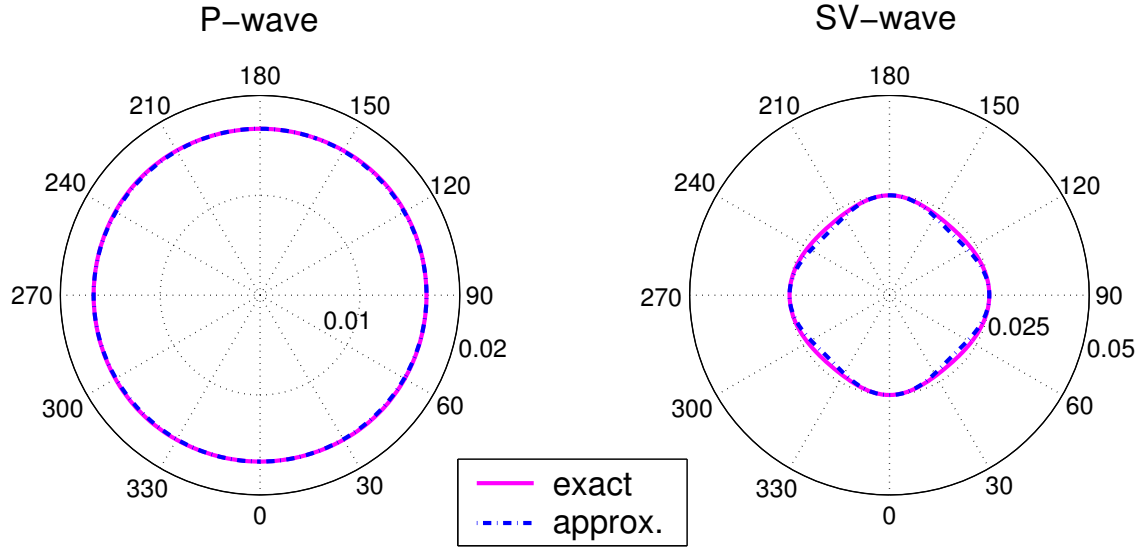


Figure 2.10. Attenuation coefficients of P-waves (left) and SV-waves (right) for $\epsilon = 0.4$, $\delta = 0.15$, and $\epsilon_Q = \delta_Q = 0$. The solid curves are the exact values of \mathcal{A} obtained by jointly solving equations B.3 and B.4; the dash-dotted curves are the approximate coefficients from equations 2.36 and 2.41. The other model parameters are the same as those in Figure 2.9.

the attenuation coefficient of SV-waves varies with angle because of the contribution of the velocity anisotropy (i.e., of the term involving σ) in equation 2.41. As discussed above, if the condition $\epsilon_Q = \delta_Q = 0$ is supplemented by $g_Q = 1$, all components Q_{ij} are identical, and both P- and SV-wave attenuation coefficients are independent of direction no matter how strong the velocity anisotropy is.

If ϵ_Q and δ_Q satisfy condition 2.44, which results in $\sigma_Q = 0$ (Figure 2.11), the exact SV-wave attenuation coefficient is almost constant, although some deviations from a circle are visible. The curve of the P-wave coefficient \mathcal{A}_P looks close to an ellipse, but *elliptical attenuation anisotropy* for P-waves requires that $\epsilon_Q = \delta_Q$.

2.8 Summary and conclusions

The main goal of this chapter is to build a practical, analytic framework for describing attenuation-related amplitude distortions in transversely isotropic (TI) media. Although the symmetry axis was taken to be vertical, all results can be applied for TI media with an arbitrary axis orientation. Under the assumption of weak attenuation, I restricted the discussion to *homogeneous* wave propagation by taking the real and the imaginary parts of the wave vector to be parallel to one another. For layered attenuative models, however, the assumption of homogeneity may cause errors in the estimation of attenuation coefficients.

When attenuation is directionally dependent, the quality factor Q is a matrix with each

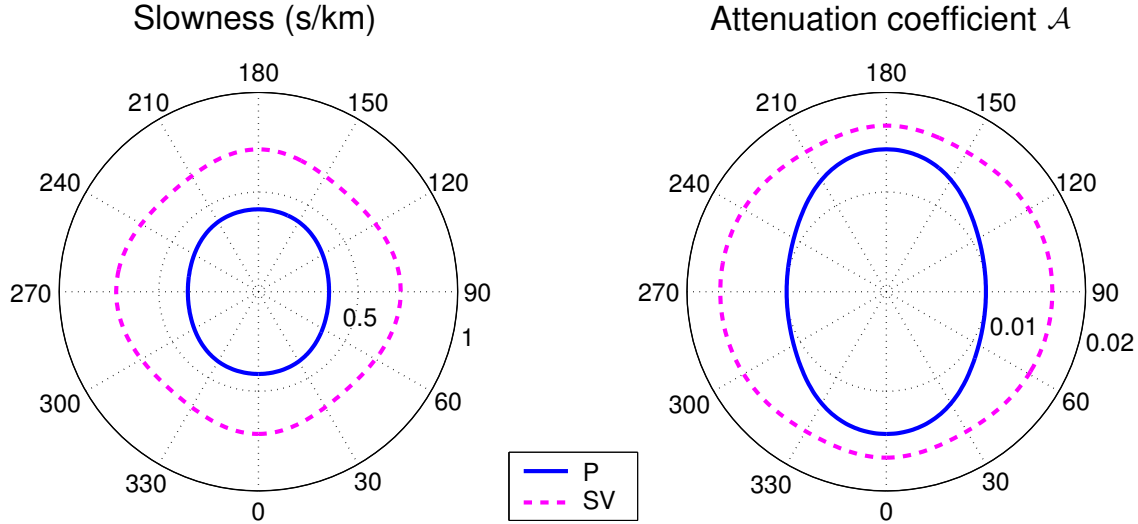


Figure 2.11. Exact slownesses (left) and attenuation coefficients \mathcal{A} (right) of P-waves (solid curves) and SV-waves (dashed) for a medium with the isotropic condition for SV-wave attenuation ($\sigma_Q = 0$). The model parameters are $V_{P0}=2.42$ km/s, $V_{S0}=1.4$ km/s, $\epsilon = 0.18$, $\delta = 0.05$, $Q_{33} = 35$, $Q_{55} = 30$, $\epsilon_Q = -0.30$, and $\delta_Q = -0.40$ (ϵ_Q and δ_Q satisfy equation 2.44).

component Q_{ij} defined as the ratio of the real and the imaginary parts of the corresponding stiffness coefficient. The \mathbf{Q} matrix has a purely isotropic structure if it includes just two independent elements responsible for the attenuation coefficients of P- and S-waves along the symmetry axis. For the special case of $Q_{ij} = \text{const}$, plane-wave attenuation is independent of propagation direction, even for arbitrary velocity anisotropy.

It seems plausible that the attenuation anisotropy, as defined by the structure of the \mathbf{Q} matrix, has symmetry the same as or higher than that of the velocity anisotropy. Here, I treated TI velocity models with either TI or isotropic attenuation and assumed that the symmetry axes for the velocity and attenuation anisotropy are aligned. Analysis of the Christoffel equation for this model shows that the perturbation of the phase-velocity function caused by the attenuation is of the second order and can be ignored.

To facilitate the description of TI attenuation, I introduced Thomsen-style parameters responsible for directionally dependent attenuation coefficients of P-, SV-, and SH-waves. The reference “isotropic” values are the P- and S-wave attenuation coefficients in the vertical (symmetry) direction (\mathcal{A}_{P0} and \mathcal{A}_{S0}). Following the idea of Thomsen’s notation for velocity anisotropy, I supplemented the reference quantities with three dimensionless anisotropic parameters denoted by ϵ_Q , δ_Q , and γ_Q .

The parameter ϵ_Q is equal to the fractional difference between the P-wave horizontal and vertical attenuation coefficients, and γ_Q denotes the same quantity for SH-waves.

Similar to the Thomsen parameter δ for velocity anisotropy, the parameter δ_Q is designed to describe near-vertical variations in P-wave attenuation. I defined δ_Q as the normalized second derivative of the P-wave attenuation coefficient at vertical incidence. In contrast to ϵ_Q and γ_Q , the parameter δ_Q depends on δ and, therefore, reflects the coupling between the attenuation and velocity anisotropy. If the frequency dependence of the quality factor and phase velocity for seismic bandwidth cannot be ignored, the attenuation-anisotropy parameters also become functions of frequency. This, however, does not formally change the definitions of ϵ_Q , δ_Q , and γ_Q .

While the attenuation coefficient of SH-waves can be expressed in a straightforward way through the parameter γ_Q , exact equations for the attenuation anisotropy of P- and SV-waves are much more involved. The Thomsen-style parameters, however, can be used to obtain the linearized attenuation coefficients under the assumptions of weak attenuation and weak velocity and attenuation anisotropy. The approximate P-wave attenuation coefficient has the same form as does the linearized phase-velocity function, with the vertical velocity V_{P0} replaced by \mathcal{A}_{P0} , ϵ by ϵ_Q , and δ by δ_Q . Although the approximate solution for the attenuation coefficient for SV-waves involves contributions of both attenuation and velocity parameters, it has the same angle dependence as does its phase-velocity counterpart.

Numerical examples demonstrate that the approximate solutions adequately reproduce the character of attenuation anisotropy and are sufficiently accurate for moderately anisotropic (in terms of both velocity and attenuation) TI models. It should be emphasized that the exact P-wave attenuation coefficient in strongly anisotropic media remains a function of just three parameters – \mathcal{A}_{P0} , ϵ_Q , and δ_Q . Computation of the exact attenuation coefficients also confirms that the isotropic \mathbf{Q} matrix in TI media does not necessarily yield isotropic (i.e., independent of direction) attenuation of P- and SV-waves because of the influence of the velocity anisotropy.

Chapter 3

Plane-wave attenuation anisotropy for orthorhombic media

3.1 Summary

Orthorhombic velocity and attenuation models are needed in the interpretation of the azimuthal variation of seismic signatures recorded over fractured reservoirs. As an extension of the discussion of attenuative TI media in Chapter 2, I develop an analytic framework for describing the attenuation coefficients in orthorhombic media with orthorhombic attenuation having identical symmetry of both the real and imaginary parts of the stiffness tensor, under the assumption of homogeneous wave propagation.

The analogous form of the Christoffel equation in the symmetry planes of orthorhombic and VTI media helps to obtain the symmetry-plane attenuation coefficients by adapting the existing VTI equations. To take full advantage of this equivalence with transverse isotropy, I introduce a parameter set similar to the VTI attenuation-anisotropy parameters ϵ_Q , δ_Q , and γ_Q . This notation, based on the same principle as Tsvankin's velocity-anisotropy parameters for orthorhombic media, leads to simple linearized equations for the symmetry-plane attenuation coefficients of all three modes (P, S_1 , and S_2).

The attenuation-anisotropy parameters also make it possible to simplify the P-wave attenuation coefficient \mathcal{A}_P outside the symmetry planes under the assumption of small attenuation and weak velocity and attenuation anisotropy. The approximate \mathcal{A}_P has the same form as that of the linearized phase-velocity function, with Tsvankin's velocity parameters $\epsilon^{(1,2)}$ and $\delta^{(1,2,3)}$ replaced by the attenuation parameters $\epsilon_Q^{(1,2)}$ and $\delta_Q^{(1,2,3)}$. The exact attenuation coefficient \mathcal{A}_P , however, also depends on the velocity-anisotropy parameters, while the body-wave velocities are almost uninfluenced by the presence of attenuation.

The reduction in the number of parameters responsible for the P-wave attenuation and the simple approximation for the coefficient \mathcal{A}_P provide a basis for inverting P-wave attenuation measurements from orthorhombic media. The attenuation processing has to be preceded by anisotropic velocity analysis that, in the absence of pronounced velocity dispersion, can be performed using existing algorithms for nonattenuative media.

3.2 Introduction

Effective velocity models of fractured reservoirs often have orthorhombic or an even lower symmetry (Schoenberg and Helbig, 1997; Bakulin et al., 2000b). It is likely that polar

and azimuthal velocity variations in orthorhombic formations are accompanied by directionally dependent attenuation. Indeed, systems of aligned fractures or pores are among the most common physical reasons for anisotropic attenuation. For example, Lynn et al. (1999) discuss the relationship between the azimuthal variation of attenuation and horizontal permeability measured over a fractured reservoir.

In this chapter, I study the attenuation of plane waves propagating in a homogeneous medium that has orthorhombic symmetry for both the velocity function and attenuation coefficient. The main signature analyzed here is the wavenumber-normalized attenuation coefficient \mathcal{A} defined in equation 2.11, which determines the rate of amplitude decay per wavelength. Here the discussion is based on the same assumptions as those in Chapter 2, i.e., homogeneous wave propagation as well as aligned symmetry for both velocity and attenuation.

The main challenge in describing the attenuation anisotropy in orthorhombic materials is in the large number of parameters that control the attenuation coefficients. Because of the coupling between the velocity and attenuation anisotropy, the coefficient \mathcal{A} depends (for a fixed orientation of the symmetry planes) on the nine real stiffness coefficients and nine elements of the quality-factor matrix. Here, I show that significant simplifications can be achieved by extending the principle of Tsvankin's (1997, 2005) notation for velocity anisotropy to attenuative orthorhombic media.

The equivalence between the complex Christoffel equation in the symmetry planes of orthorhombic and VTI media makes it possible to obtain the symmetry-plane attenuation coefficients from the corresponding VTI equations. As shown in Chapter 2, attenuation anisotropy in VTI media can be conveniently described by the Thomsen-style parameters ϵ_Q , δ_Q , and γ_Q . Adapting these results for the symmetry planes of orthorhombic media, I introduce a set of seven anisotropy parameters that fully characterizes (in combination with the velocity parameters) directionally-dependent attenuation in orthorhombic materials. Linearizing the P-wave attenuation coefficient in the limit of small attenuation and weak anisotropy yields a simple expression *outside* the symmetry planes that has the same form as Tsvankin's (1997, 2005) weak-anisotropy approximation for the velocity function. The accuracy of this approximate solution is verified using numerical tests for models with substantial attenuation and velocity anisotropy.

To highlight the similarities between the anisotropy parameters for velocity and attenuation, I generally follow the organization of Tsvankin's (1997) paper in which he extended Thomsen's (1986) velocity-anisotropy notation to orthorhombic media. On the other hand, I emphasize distinct properties of attenuation anisotropy related to the coupling between the attenuation coefficient and velocity function.

3.3 Christoffel equation for attenuative orthorhombic media

Consider plane-wave propagation in orthorhombic media (Figure 3.1) with orthorhombic attenuation, in which the symmetry of the imaginary part of the stiffness matrix is identical to that of the real part. It is convenient to choose a Cartesian coordinate system aligned with the natural coordinate frame of the model, so that each coordinate plane

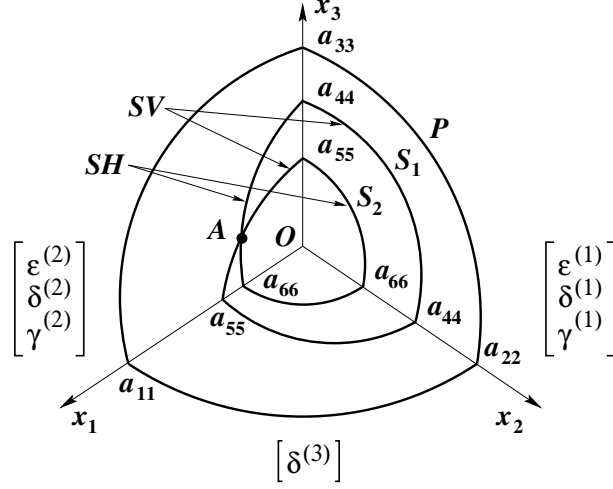


Figure 3.1. Sketch of the phase-velocity surfaces in orthorhombic media (after Tsvankin, 2005). $a_{ij} \equiv \sqrt{c_{ij}/\rho}$ are the normalized stiffness coefficients. Tsvankin's (1997) velocity-anisotropy parameters, $\epsilon^{(1,2)}$, $\delta^{(1,2,3)}$, and $\gamma^{(1,2)}$, are defined in the symmetry planes of the model, which coincide with the coordinate planes.

coincides with one of the three symmetry planes.

Substituting a plane wave (equation 2.5) into the wave equation yields the following Christoffel equation:

$$\begin{bmatrix} \tilde{c}_{11}\tilde{k}_1^2 + \tilde{c}_{66}\tilde{k}_2^2 + \tilde{c}_{55}\tilde{k}_3^2 - \rho\omega^2 & (\tilde{c}_{12} + \tilde{c}_{66})\tilde{k}_1\tilde{k}_2 & (\tilde{c}_{13} + \tilde{c}_{55})\tilde{k}_1\tilde{k}_3 \\ (\tilde{c}_{12} + \tilde{c}_{66})\tilde{k}_1\tilde{k}_2 & \tilde{c}_{66}\tilde{k}_1^2 + \tilde{c}_{22}\tilde{k}_2^2 + \tilde{c}_{44}\tilde{k}_3^2 - \rho\omega^2 & (\tilde{c}_{23} + \tilde{c}_{44})\tilde{k}_2\tilde{k}_3 \\ (\tilde{c}_{13} + \tilde{c}_{55})\tilde{k}_1\tilde{k}_3 & (\tilde{c}_{23} + \tilde{c}_{44})\tilde{k}_2\tilde{k}_3 & \tilde{c}_{55}\tilde{k}_1^2 + \tilde{c}_{44}\tilde{k}_2^2 + \tilde{c}_{33}\tilde{k}_3^2 - \rho\omega^2 \end{bmatrix} \begin{bmatrix} \tilde{U}_1 \\ \tilde{U}_2 \\ \tilde{U}_3 \end{bmatrix} = 0, \quad (3.1)$$

where $\tilde{c}_{ij} = c_{ij} + ic_{ij}^I$ are the complex stiffness coefficients. Following Carcione (2001), the elements of the quality-factor matrix are defined as the ratio of the real and imaginary parts of the corresponding stiffness coefficients (equation 2.1).

Assuming homogeneous wave propagation ($\mathbf{k} \parallel \mathbf{k}^I$), the wave vector can be expressed through the unit vector \mathbf{n} in the slowness direction: $\tilde{\mathbf{k}} = \mathbf{n}\tilde{k}$. Then, the Christoffel equation 3.1 becomes

$$\left[\tilde{G}_{ij} - \rho\tilde{V}^2\delta_{ik} \right] \tilde{U}_k = 0, \quad (3.2)$$

where $\tilde{V} = \frac{\omega}{k}$ is the complex phase velocity, and \tilde{G}_{ij} are the elements of the complex Christoffel matrix:

$$\begin{aligned}
\tilde{G}_{11} &= \tilde{c}_{11}n_1^2 + \tilde{c}_{66}n_2^2 + \tilde{c}_{55}n_3^2, \\
\tilde{G}_{22} &= \tilde{c}_{66}n_1^2 + \tilde{c}_{22}n_2^2 + \tilde{c}_{44}n_3^2, \\
\tilde{G}_{33} &= \tilde{c}_{55}n_1^2 + \tilde{c}_{44}n_2^2 + \tilde{c}_{33}n_3^2, \\
\tilde{G}_{12} &= (\tilde{c}_{12} + \tilde{c}_{66})n_1n_2, \\
\tilde{G}_{13} &= (\tilde{c}_{13} + \tilde{c}_{55})n_1n_3, \\
\tilde{G}_{23} &= (\tilde{c}_{23} + \tilde{c}_{44})n_2n_3.
\end{aligned} \tag{3.3}$$

The components of the unit slowness (phase) vector \mathbf{n} can be expressed through the polar phase angle θ and the azimuthal phase angle ϕ : $n_1 = \sin \theta \cos \phi$, $n_2 = \sin \theta \sin \phi$, $n_3 = \cos \theta$.

Note that although equation 3.2 has the same form as that of the Christoffel equation in nonattenuative (purely elastic) orthorhombic media, the velocity, polarization, and stiffnesses are complex. As a result, plane-wave propagation is described by two coupled equations obtained by separating the real and imaginary parts of the Christoffel equation.

3.4 Attenuation coefficients in the symmetry planes

Suppose that the plane wave (equation 2.5) propagates in the $[x_1, x_3]$ -plane, so $n_1 = \sin \theta$, $n_2 = 0$, and $n_3 = \cos \theta$. Then the Christoffel equation 3.1 simplifies to

$$\begin{bmatrix}
\tilde{c}_{11}\tilde{k}_1^2 + \tilde{c}_{55}\tilde{k}_3^2 - \rho\omega^2 & 0 & (\tilde{c}_{13} + \tilde{c}_{55})\tilde{k}_1\tilde{k}_3 \\
0 & \tilde{c}_{66}\tilde{k}_1^2 + \tilde{c}_{44}\tilde{k}_3^2 - \rho\omega^2 & 0 \\
(\tilde{c}_{13} + \tilde{c}_{55})\tilde{k}_1\tilde{k}_3 & 0 & \tilde{c}_{55}\tilde{k}_1^2 + \tilde{c}_{33}\tilde{k}_3^2 - \rho\omega^2
\end{bmatrix}
\begin{bmatrix}
\tilde{U}_1 \\
\tilde{U}_2 \\
\tilde{U}_3
\end{bmatrix} = 0. \tag{3.4}$$

Equation 3.4 has the same form as the Christoffel equation for VTI media with VTI attenuation. The only difference between the two equations is that while for VTI media $\tilde{c}_{44} = \tilde{c}_{55}$, this is generally not the case for orthorhombic symmetry. However, the stiffness \tilde{c}_{44} influences only the SH-wave polarized perpendicular to the propagation plane (see below), while \tilde{c}_{55} contributes to the velocity and attenuation of the in-plane polarized waves (P and SV). Therefore, the known equivalence between the Christoffel equation in purely elastic VTI media and symmetry planes of orthorhombic media (e.g., Tsvankin, 1997, 2005) holds for attenuative models with identical symmetries of the real and imaginary parts of stiffness tensor.

Since the Christoffel matrix for wave propagation in the $[x_1, x_3]$ -plane has four vanishing elements, equation 3.4 splits into two separate equations, one for the SH-wave polarized in the x_2 -direction (the displacement component \tilde{U}_2), and the other for the in-plane polarized P- and SV-waves (the components \tilde{U}_1 and \tilde{U}_3). The solutions for the velocity and attenuation of all three modes can be obtained by simply adapting the results of Chapter 2 for VTI media.

With the assumption of homogeneous wave propagation, the Christoffel equation for

the SH-wave takes the form

$$(\tilde{c}_{66} \sin^2 \theta + \tilde{c}_{44} \cos^2 \theta) \tilde{k}^2 - \rho \omega^2 = 0. \quad (3.5)$$

By analogy with attenuative VTI media, the normalized attenuation coefficient of SH-waves in the $[x_1, x_3]$ -plane can be obtained from equation 3.5 as

$$\mathcal{A}_{SH}^{(2)} = \sqrt{1 + (Q_{44} \alpha^{(2)})^2} - Q_{44} \alpha^{(2)}, \quad (3.6)$$

where the superscript “(2)” stands for the x_2 -axis orthogonal to the propagation plane (the same convention as in Tsvankin, 1997), and

$$\alpha^{(2)} \equiv \frac{(1 + 2\gamma^{(2)}) \sin^2 \theta + \cos^2 \theta}{(1 + 2\gamma^{(2)}) \frac{Q_{44}}{Q_{66}} \sin^2 \theta + \cos^2 \theta}.$$

For P- and SV-waves in the regime of homogeneous wave propagation, equation 3.4 reduces to

$$\begin{bmatrix} (\tilde{c}_{11} \sin^2 \theta + \tilde{c}_{55} \cos^2 \theta) \tilde{k}^2 - \rho \omega^2 & (\tilde{c}_{13} + \tilde{c}_{55}) \sin \theta \cos \theta \tilde{k}^2 \\ (\tilde{c}_{13} + \tilde{c}_{55}) \sin \theta \cos \theta \tilde{k}^2 & (\tilde{c}_{55} \sin^2 \theta + \tilde{c}_{33} \cos^2 \theta) \tilde{k}^2 - \rho \omega^2 \end{bmatrix} \begin{bmatrix} \tilde{U}_1 \\ \tilde{U}_3 \end{bmatrix} = 0. \quad (3.7)$$

The wavenumber obtained from equation 3.7 is described by the same expression as that for nonattenuative VTI media (e.g., Tsvankin, 2005):

$$\begin{aligned} \tilde{k} &= \omega \sqrt{2\rho} \{ (\tilde{c}_{11} + \tilde{c}_{55}) \sin^2 \theta + (\tilde{c}_{33} + \tilde{c}_{55}) \cos^2 \theta \\ &\pm \sqrt{[(\tilde{c}_{11} - \tilde{c}_{55}) \sin^2 \theta - (\tilde{c}_{33} - \tilde{c}_{55}) \cos^2 \theta]^2 + 4(\tilde{c}_{13} + \tilde{c}_{55})^2 \sin^2 \theta \cos^2 \theta} \}^{-1/2}. \end{aligned} \quad (3.8)$$

The normalized attenuation coefficients $\mathcal{A}_{P,SV}^{(2)}$ were derived from the complex part of equation 3.9. For example, the P-wave coefficients $\mathcal{A}_P^{(2)}$ in the vertical and horizontal directions are given by (see also equations 2.22 and 2.23)

$$\mathcal{A}_P^{(2)}(\theta = 0^\circ) = Q_{33} \left(\sqrt{1 + 1/Q_{33}^2} - 1 \right) \approx \frac{1}{2Q_{33}}, \quad (3.9)$$

$$\mathcal{A}_P^{(2)}(\theta = 90^\circ) = Q_{11} \left(\sqrt{1 + 1/Q_{11}^2} - 1 \right) \approx \frac{1}{2Q_{11}}. \quad (3.10)$$

The SV-wave attenuation coefficient in both the vertical and horizontal directions is

$$\mathcal{A}_{SV}^{(2)}(\theta = 0^\circ) = \mathcal{A}_{SV}^{(2)}(\theta = 90^\circ) = Q_{55} \left(\sqrt{1 + 1/Q_{55}^2} - 1 \right) \approx \frac{1}{2Q_{55}}. \quad (3.11)$$

For plane-wave propagation in the $[x_2, x_3]$ -plane ($n_1 = 0$, $n_2 = \sin \theta$, and $n_3 = \cos \theta$), the Christoffel equation 3.1 gives

$$\begin{bmatrix} \tilde{c}_{66}\tilde{k}_1^2 + \tilde{c}_{55}\tilde{k}_3^2 - \rho\omega^2 & 0 & 0 \\ 0 & \tilde{c}_{22}\tilde{k}_1^2 + \tilde{c}_{44}\tilde{k}_3^2 - \rho\omega^2 & (\tilde{c}_{23} + \tilde{c}_{44})\tilde{k}_1\tilde{k}_3 \\ 0 & (\tilde{c}_{23} + \tilde{c}_{44})\tilde{k}_1\tilde{k}_3 & \tilde{c}_{44}\tilde{k}_1^2 + \tilde{c}_{33}\tilde{k}_3^2 - \rho\omega^2 \end{bmatrix} \begin{bmatrix} \tilde{U}_1 \\ \tilde{U}_2 \\ \tilde{U}_3 \end{bmatrix} = 0. \quad (3.12)$$

The SH-wave, which is polarized in the x_1 -direction, is described by the element $[\tilde{c}_{66}\tilde{k}_1^2 + \tilde{c}_{55}\tilde{k}_3^2 - \rho\omega^2]$ of the matrix in equation 3.12. It is clear from equations 3.4 and 3.12 that both the velocity and attenuation of the SH-wave can be obtained from the corresponding equations for the $[x_1, x_3]$ -plane (or VTI media) by making the substitution $4 \rightarrow 5$ in the subscripts of the stiffnesses and elements Q_{ij} . Note that the SH-waves in the two vertical symmetry planes actually represent two different split shear modes (S_1 and S_2); this is discussed in more detail below.

The velocity and attenuation of P- and SV-waves in the $[x_2, x_3]$ -plane can be found from (for homogeneous wave propagation)

$$\begin{bmatrix} (\tilde{c}_{22} \sin^2 \theta + \tilde{c}_{44} \cos^2 \theta) \tilde{k}^2 - \rho\omega^2 & (\tilde{c}_{23} + \tilde{c}_{44}) \sin \theta \cos \theta \tilde{k}^2 \\ (\tilde{c}_{23} + \tilde{c}_{44}) \sin \theta \cos \theta \tilde{k}^2 & (\tilde{c}_{44} \sin^2 \theta + \tilde{c}_{33} \cos^2 \theta) \tilde{k}^2 - \rho\omega^2 \end{bmatrix} \begin{bmatrix} \tilde{U}_2 \\ \tilde{U}_3 \end{bmatrix} = 0. \quad (3.13)$$

Because equations 3.7 and 3.13 have analogous form, the P- and SV-wave attenuation coefficients can be obtained from the corresponding expressions for the $[x_1, x_3]$ -plane using the following substitutions in the subscripts: $1 \rightarrow 2$ and $5 \rightarrow 4$. The same substitutions were used by Tsvankin (1997, 2005) in his extension of VTI velocity equations to the symmetry planes of orthorhombic media. The equivalence with vertical transverse isotropy is also valid for the complex Christoffel equation in the $[x_1, x_2]$ symmetry plane.

3.5 Attenuation-anisotropy parameters

3.5.1 Thomsen-style notation

The Thomsen-style notation for velocity anisotropy introduced by Tsvankin (1997, 2005) helps to simplify the analytic description of a wide range of seismic signatures for orthorhombic media. Tsvankin's parameters provided a basis for developing a number of seismic inversion and processing methods operating with orthorhombic models (Grechka and Tsvankin, 1999; Grechka et al., 1999; Bakulin et al., 2000b). Here, I extend his approach to attenuative orthorhombic media with the main goal of defining the parameter combinations that govern the directionally dependent attenuation coefficient.

Since the new notation is designed primarily for reflection data, I choose the P- and S-wave attenuation coefficients in the vertical (x_3) direction (\mathcal{A}_{P0} and \mathcal{A}_{S0}) as the reference isotropic quantities. The coefficient \mathcal{A}_{S0} corresponds to the S-wave polarized in the x_1 -direction, which may be either the fast or slow shear mode depending on the relationship

between the stiffnesses c_{44} and c_{55} . According to equations 3.9 and 3.11, the approximate (accurate to the second order in $1/Q$) coefficients \mathcal{A}_{P0} and \mathcal{A}_{S0} are given by

$$\mathcal{A}_{P0} \equiv \frac{1}{2Q_{33}}, \quad (3.14)$$

$$\mathcal{A}_{S0} \equiv \frac{1}{2Q_{55}}. \quad (3.15)$$

To characterize the attenuation of waves propagating in the $[x_1, x_3]$ -plane, I define three attenuation-anisotropy parameters analogous to the Thomsen-style parameters ϵ_Q , δ_Q , and γ_Q introduced for VTI media with VTI attenuation (Chapter 2). The parameters $\epsilon_Q^{(2)}$ and $\gamma_Q^{(2)}$ (the superscript “(2)” stands for the x_2 -axis perpendicular to the $[x_1, x_3]$ -plane) determine the fractional difference between the normalized attenuation coefficients in the x_1 - and x_3 -directions for the P- and SH-waves, respectively. Another parameter, $\delta_Q^{(2)}$, is expressed through the second derivative of the P-wave attenuation coefficient in the vertical direction and, therefore, governs the P-wave attenuation for near-vertical propagation in the $[x_1, x_3]$ -plane.

$$\epsilon_Q^{(2)} \equiv \frac{Q_{33} - Q_{11}}{Q_{11}}, \quad (3.16)$$

$$\begin{aligned} \delta_Q^{(2)} &\equiv \frac{1}{2\mathcal{A}_{P0}} \left. \frac{d^2 \mathcal{A}_P^{(2)}}{d\theta^2} \right|_{\theta=0} \\ &= \frac{\frac{Q_{33} - Q_{55}}{Q_{55}} c_{55} \frac{(c_{13} + c_{33})^2}{(c_{33} - c_{55})} + 2 \frac{Q_{33} - Q_{13}}{Q_{13}} c_{13} (c_{13} + c_{55})}{c_{33} (c_{33} - c_{55})} \end{aligned} \quad (3.17)$$

$$\approx 4 \frac{Q_{33} - Q_{55}}{Q_{55}} g^{(2)} + 2 \frac{Q_{33} - Q_{13}}{Q_{13}} (1 + 2\delta^{(2)} - 2g^{(2)}), \quad (3.18)$$

$$\gamma_Q^{(2)} \equiv \frac{Q_{44} - Q_{66}}{Q_{66}}, \quad (3.19)$$

where equation 3.18 for $\delta_Q^{(2)}$ has been simplified by assuming that the ratio $g^{(2)} \equiv \frac{c_{55}}{c_{33}}$ and the absolute value of Tsvankin’s velocity-anisotropy parameter $\delta^{(2)}$ are small. Since the Christoffel equation in the $[x_1, x_3]$ -plane has the same form as that for VTI media, equations 3.16–3.19 are identical to the definitions of the corresponding VTI parameters. In contrast to VTI models, however, the parameters of orthorhombic media with the subscripts “55” and “44” generally differ, and cannot be interchanged in equations 3.17–3.19.

Using the substitutions $1 \rightarrow 2$ and $5 \rightarrow 4$ in the subscripts, I further adapt the definitions of attenuation anisotropy parameters for VTI media to introduce three attenuation-

anisotropy parameters in the $[x_2, x_3]$ -plane:

$$\epsilon_Q^{(1)} \equiv \frac{Q_{33} - Q_{22}}{Q_{22}}, \quad (3.20)$$

$$\begin{aligned} \delta_Q^{(1)} &\equiv \frac{1}{2\mathcal{A}_{P0}} \left. \frac{d^2 \mathcal{A}_P^{(1)}}{d\theta^2} \right|_{\theta=0} \\ &= \frac{\frac{Q_{33} - Q_{44}}{Q_{44}} c_{44} \frac{(c_{23} + c_{33})^2}{(c_{33} - c_{44})} + 2 \frac{Q_{33} - Q_{23}}{Q_{23}} c_{23} (c_{23} + c_{44})}{c_{33} (c_{33} - c_{44})} \end{aligned} \quad (3.21)$$

$$\approx 4 \frac{Q_{33} - Q_{44}}{Q_{44}} g^{(1)} + 2 \frac{Q_{33} - Q_{23}}{Q_{23}} (1 + 2\delta^{(1)} - 2g^{(1)}), \quad (3.22)$$

$$\gamma_Q^{(1)} \equiv \frac{Q_{55} - Q_{66}}{Q_{66}}. \quad (3.23)$$

In equation 3.22, $\delta^{(1)}$ is the velocity-anisotropy parameter defined in the $[x_2, x_3]$ -plane (Tsvankin, 1997, 2005), and $g^{(1)} \equiv \frac{c_{44}}{c_{33}}$. Since the attenuation coefficient must be positive (otherwise, the amplitude will increase with distance), the diagonal components of the Q_{ij} -matrix have to be positive as well. This constraint implies that the parameters $\epsilon_Q^{(1)}$, $\epsilon_Q^{(2)}$, $\gamma_Q^{(1)}$, and $\gamma_Q^{(2)}$ are always larger than -1 .

The only element of the \mathbf{Q} -matrix not involved in the definitions of the reference isotropic quantities and the attenuation-anisotropy parameters in the vertical symmetry planes is Q_{12} . Following the approach of Tsvankin (1997, 2005), I use Q_{12} to introduce one more anisotropy parameter, $\delta_Q^{(3)}$, which plays the role of the VTI parameter δ_Q in the $[x_1, x_2]$ -plane (x_1 is treated as the symmetry axis of the equivalent VTI model):

$$\begin{aligned} \delta_Q^{(3)} &\equiv \frac{1}{2\mathcal{A}_P^{(3)}(\theta=0)} \left. \frac{d^2 \mathcal{A}_P^{(3)}}{d\theta^2} \right|_{\theta=0} \\ &= \frac{\frac{Q_{11} - Q_{66}}{Q_{66}} c_{66} \frac{(c_{11} + c_{12})^2}{(c_{11} - c_{66})} + 2 \frac{Q_{11} - Q_{12}}{Q_{12}} c_{12} (c_{12} + c_{66})}{c_{11} (c_{11} - c_{66})} \end{aligned} \quad (3.24)$$

$$\approx 4 \frac{Q_{11} - Q_{66}}{Q_{66}} g^{(3)} + 2 \frac{Q_{11} - Q_{12}}{Q_{12}} (1 + 2\delta^{(3)} - 2g^{(3)}), \quad (3.25)$$

where the phase angle θ is measured from the x_1 -axis, $\delta^{(3)}$ is a velocity-anisotropy parameter defined in the $[x_1, x_2]$ -plane, and $g^{(3)} \equiv \frac{c_{66}}{c_{11}}$. Although it is also possible to introduce the parameters $\epsilon_Q^{(3)}$ and $\gamma_Q^{(3)}$ in the $[x_1, x_2]$ -plane, they would be redundant.

The nine attenuation-anisotropy parameters defined in equations 3.14–3.25, combined with Tsvankin's (1997, 2005) velocity-anisotropy parameters, are sufficient to fully characterize plane-wave attenuation in orthorhombic media. An additional parameter, of practical importance because it is responsible for the differential attenuation of the split S-waves in

the vertical (x_3) direction, is described in the next section.

3.6 Approximate attenuation coefficients in the symmetry planes

The equivalence between plane-wave propagation in the symmetry planes of orthorhombic media and in VTI media means that the symmetry-plane attenuation coefficients of all three modes can be obtained by adapting the VTI equations. While the exact attenuation coefficients are rather complicated even for VTI models and do not provide insight into the influence of various attenuation-anisotropy parameters, much simpler solutions can be found under the following assumptions:

1. The magnitude of attenuation measured by the inverse Q_{ij} values or the parameters \mathcal{A}_{P0} and \mathcal{A}_{S0} is small.
2. Attenuation anisotropy is weak, which implies that the absolute values of all attenuation-anisotropy parameters introduced above are much smaller than unity.
3. Velocity anisotropy is also weak, so the absolute values of all Tsvankin's (1997, 2005) anisotropy parameters are much smaller than unity.

The approximate (linearized in the small parameters) SH-wave attenuation coefficient in the $[x_1, x_3]$ -plane can be written as (compare to equation 2.27)

$$\mathcal{A}_{SH}^{(2)} = \bar{\mathcal{A}}_{S0} (1 + \gamma_Q^{(2)} \sin^2 \theta), \quad (3.26)$$

where

$$\bar{\mathcal{A}}_{S0} = \frac{1}{2Q_{44}} = \mathcal{A}_{S0} \frac{1 + \gamma_Q^{(1)}}{1 + \gamma_Q^{(2)}} \quad (3.27)$$

is the vertical attenuation coefficient for the S-wave polarized in the x_2 -direction. Equation 3.26 is obtained by replacing the parameter γ_Q in the linearized VTI result (Chapter 2) by $\gamma_Q^{(2)}$ and using the appropriate reference value $\bar{\mathcal{A}}_{S0}$. Similarly, the corresponding linearized coefficient in the $[x_2, x_3]$ -plane has the form

$$\mathcal{A}_{SH}^{(1)} = \mathcal{A}_{S0} (1 + \gamma_Q^{(1)} \sin^2 \theta). \quad (3.28)$$

It should be emphasized that the term *SH-wave* refers to two different shear modes in the vertical symmetry planes (Tsvankin, 1997, 2005). For example, if $c_{44} > c_{55}$, then the fast shear wave S_1 represents an SH-wave in the $[x_1, x_3]$ -plane in which it is polarized in the x_2 -direction. For propagation in the $[x_2, x_3]$ -plane, however, the S_1 -wave becomes an SV mode that has an in-plane polarization vector.

The difference between the attenuation coefficients of the vertically traveling split shear waves can be quantified by the *attenuation splitting parameter* $\gamma_Q^{(S)}$:

$$\gamma_Q^{(S)} \equiv \left| \frac{\bar{\mathcal{A}}_{S0} - \mathcal{A}_{S0}}{\mathcal{A}_{S0}} \right| = \frac{|\gamma_Q^{(1)} - \gamma_Q^{(2)}|}{1 + \gamma_Q^{(2)}} \approx |\gamma_Q^{(1)} - \gamma_Q^{(2)}|. \quad (3.29)$$

The definition 3.29 is analogous to that of the widely used S-wave velocity splitting parameter $\gamma^{(S)}$ (e.g., Tsvankin, 1997, 2005). Although $\gamma_Q^{(S)}$ would be redundant as part of the notation for attenuative orthorhombic media, this parameter should play an important role in the attenuation analysis of shear-wave data.

Substituting the attenuation-anisotropy parameters $\epsilon_Q^{(2)}$ and $\delta_Q^{(2)}$ into the VTI equations of Chapter 2 yields the following approximate attenuation coefficients of the P- and SV-waves in the $[x_1, x_3]$ -plane (compared to equations 2.36 and 2.41, respectively):

$$\mathcal{A}_P^{(2)} = \mathcal{A}_{P0} \left(1 + \delta_Q^{(2)} \sin^2 \theta \cos^2 \theta + \epsilon_Q^{(2)} \sin^4 \theta \right), \quad (3.30)$$

$$\mathcal{A}_{SV}^{(2)} = \mathcal{A}_{S0} \left(1 + \sigma_Q^{(2)} \sin^2 \theta \cos^2 \theta \right), \quad (3.31)$$

where

$$\sigma_Q^{(2)} \equiv \frac{1}{g_Q^{(2)}} \left[2(1 - g_Q^{(2)}) \sigma^{(2)} + \frac{\epsilon_Q^{(2)} - \delta_Q^{(2)}}{g_Q^{(2)}} \right], \quad (3.32)$$

$g^{(2)} \equiv \frac{c_{55}}{c_{33}}$, $g_Q^{(2)} \equiv \frac{Q_{33}}{Q_{55}} = \frac{\mathcal{A}_{S0}}{\mathcal{A}_{P0}}$, and $\sigma^{(2)} \equiv \frac{\epsilon^{(2)} - \delta^{(2)}}{g^{(2)}}$. The approximate attenuation coefficients in equations 3.30 and 3.31 have exactly the same form as the corresponding linearized phase-velocity equations (Thomsen, 1986). However, as shown in equation 3.17, the dependence of the attenuation-anisotropy parameter $\delta_Q^{(2)}$ on the real parts of the stiffness coefficients reflects the coupling between the attenuation and velocity anisotropy. In contrast, the anisotropic phase-velocity function is practically independent of attenuation (see below).

The linearized coefficients $\mathcal{A}_P^{(1)}$ and $\mathcal{A}_{SV}^{(1)}$ in the $[x_2, x_3]$ -plane are obtained in the same way from the VTI equations by using the attenuation-anisotropy parameters $\epsilon_Q^{(1)}$ and $\delta_Q^{(1)}$. For example,

$$\mathcal{A}_P^{(1)} = \mathcal{A}_{P0} \left(1 + \delta_Q^{(1)} \sin^2 \theta \cos^2 \theta + \epsilon_Q^{(1)} \sin^4 \theta \right). \quad (3.33)$$

3.7 P-wave attenuation outside the symmetry planes

Because of the difficulties in linearizing S-wave attenuation coefficients for out-of-plane phase directions, the scope of this section is limited to P-wave attenuation. While the attenuation of the split shear waves can be studied numerically by solving the Christoffel equation, the area of validity of such plane-wave solutions in describing radiation from seismic sources is significantly reduced because of the influence of S-wave point singularities (e.g., Crampin, 1991).

3.7.1 Influence of attenuation on phase velocity

As pointed out above, the attenuation coefficients depend not just on the quality-factor elements Q_{ij} but also on the velocity-anisotropy parameters. In contrast, the presence of attenuation has an almost negligible influence on the phase-velocity function. This result remains valid for the symmetry planes of the orthorhombic model. Here, I demonstrate that attenuation-related distortions of phase velocity are negligible outside the symmetry planes as well.

In the limit of weak attenuation ($\frac{1}{Q_{ij}} \ll 1$), the real part of the Christoffel equation (A-2) can be simplified by dropping terms quadratic in the inverse Q components. The resulting equation (A-3) is identical to the Christoffel equation for the reference nonattenuative medium, both within and outside the symmetry planes.

To evaluate the contribution of the higher-order attenuation terms, I compute the exact P-wave phase velocity for two orthorhombic models with strong attenuation. For the first model, the attenuation is isotropic with a very low quality factor, $Q_{33} = Q_{55} = 10$ (Figure 3.2). Still, the maximum attenuation-related change in the phase velocity is limited to 0.5%, which is equal to $\frac{1}{2Q_{33}^2}$.

The second model has the same real part of the stiffness matrix, but this time accompanied by pronounced attenuation anisotropy (Figure 3.3). Although the deviation of the phase-velocity function from that in the reference nonattenuative medium increases away from the vertical, it remains insignificant (no more than 1%) for the whole range of polar and azimuthal phase angles. Although this analysis does not take into account attenuation-related velocity dispersion, it is usually small in the frequency band typical for reflection seismology.

Hence, seismic processing for orthorhombic media with orthorhombic attenuation can be divided into two steps. First, one can perform anisotropic velocity analysis and estimation of Tsvankin's parameters without taking attenuation into account (Grechka and Tsvankin, 1999; Grechka et al., 1999; Bakulin et al., 2000b). Then the reconstructed anisotropic velocity model can be used in the processing of amplitude measurements and inversion for the attenuation-anisotropy parameters.

3.7.2 Approximate attenuation outside the symmetry planes

The linearized approximation for the P-wave attenuation coefficient is extended to arbitrary propagation directions outside the symmetry planes in Appendix E:

$$\mathcal{A}_P(\theta, \phi) = \mathcal{A}_{P0} [1 + \delta_Q(\phi) \sin^2 \theta \cos^2 \theta + \epsilon_Q(\phi) \sin^4 \theta] , \quad (3.34)$$

where θ , as before, is the phase angle with the vertical, ϕ is the azimuthal phase angle, and

$$\delta_Q(\phi) = \delta_Q^{(1)} \sin^2 \phi + \delta_Q^{(2)} \cos^2 \phi , \quad (3.35)$$

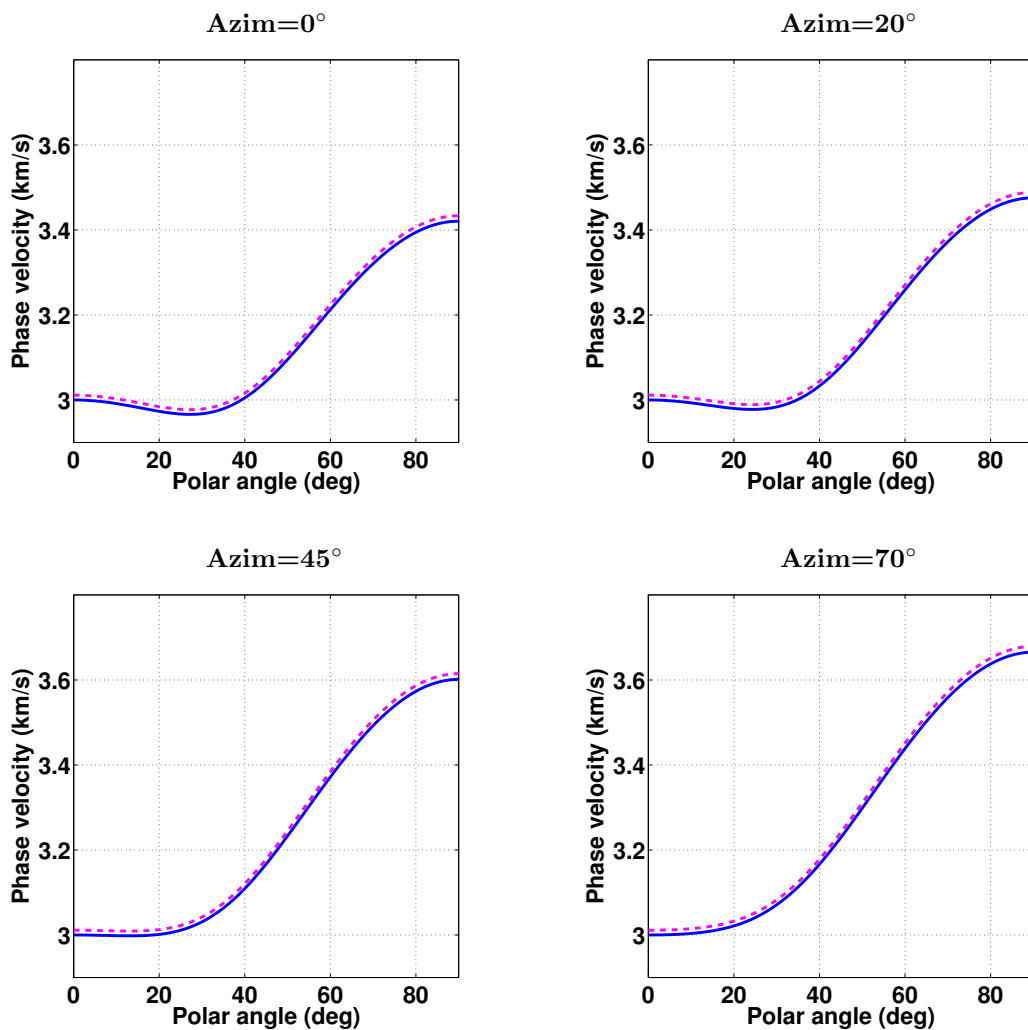


Figure 3.2. Influence of isotropic attenuation on the exact P-wave phase velocity computed from the Christoffel equation (3.2). Each plot corresponds to a fixed azimuthal phase angle. The solid curves mark the velocity for a nonattenuative orthorhombic model with the following parameters: $V_{P0} = 3$ km/s, $V_{S0} = 1.5$ km/s, $\epsilon^{(1)} = 0.25$, $\epsilon^{(2)} = 0.15$, $\delta^{(1)} = 0.05$, $\delta^{(2)} = -0.1$, $\delta^{(3)} = 0.15$, $\gamma^{(1)} = 0.28$, and $\gamma^{(2)} = 0.15$. The dashed curves are computed for a model with the same velocity parameters and strong isotropic attenuation ($Q_{33} = Q_{55} = 10$; all attenuation-anisotropy parameters are set to zero).

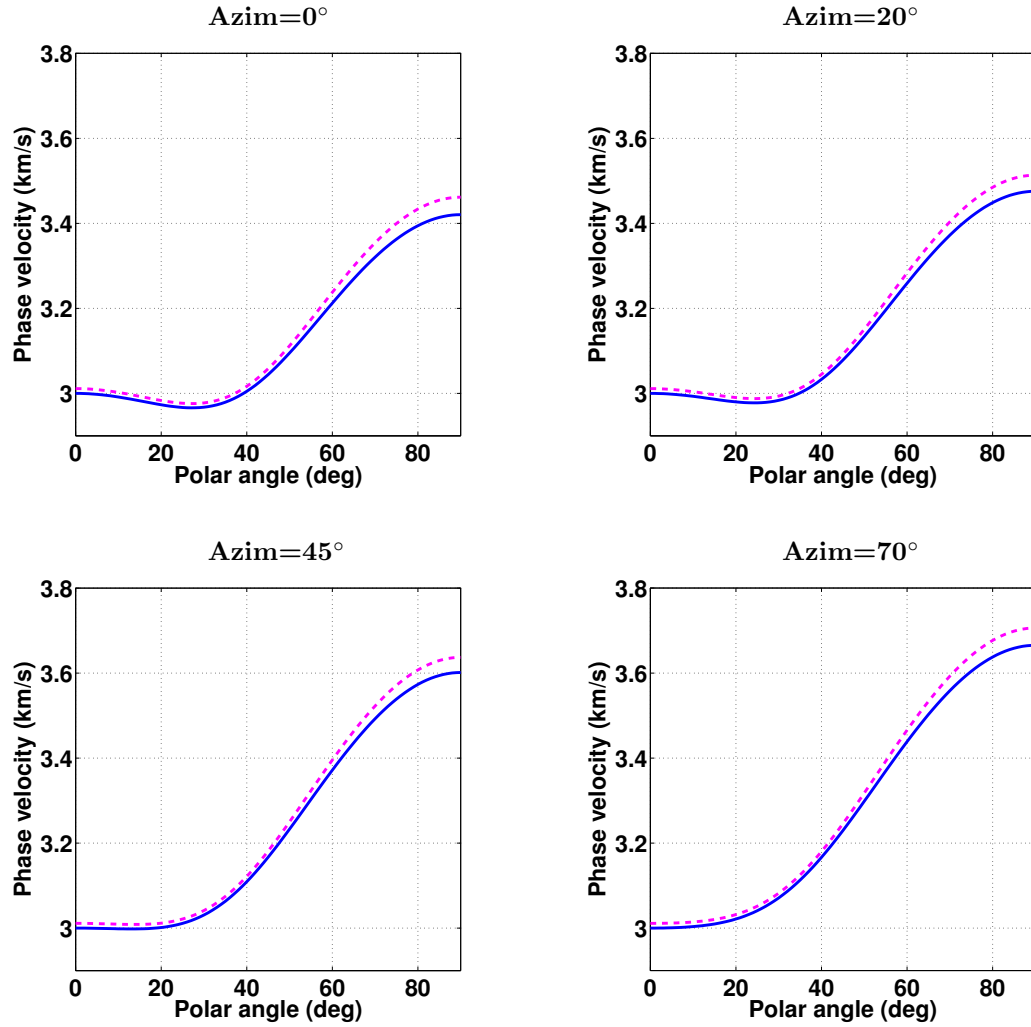


Figure 3.3. Influence of anisotropic attenuation on the exact P-wave phase velocity. The solid curves are the phase velocities for the nonattenuative orthorhombic model from Figure 3.2. The dashed curves are computed for a model with the same velocity parameters and strong orthorhombic attenuation: $Q_{33} = Q_{55} = 10$ ($\mathcal{A}_{P0} = \mathcal{A}_{S0} = 0.05$), $\epsilon_Q^{(1)} = \epsilon_Q^{(2)} = 0.8$, $\delta_Q^{(1)} = \delta_Q^{(2)} = \delta_Q^{(3)} = -0.5$, and $\gamma_Q^{(1)} = \gamma_Q^{(2)} = 0.8$.

$$\epsilon_Q(\phi) = \epsilon_Q^{(1)} \sin^4 \phi + \epsilon_Q^{(2)} \cos^4 \phi + (2\epsilon_Q^{(2)} + \delta_Q^{(3)}) \sin^2 \phi \cos^2 \phi. \quad (3.36)$$

Clearly, the approximate P-wave attenuation coefficient in any vertical plane of orthorhombic media is described by the VTI equation (Chapter 2; Zhu and Tsvankin, 2006) with the azimuthally varying parameters $\epsilon_Q(\phi)$ and $\delta_Q(\phi)$. For wave propagation in the $[x_1, x_3]$ -plane ($\phi = 0^\circ$), $\epsilon_Q = \epsilon_Q^{(2)}$, $\delta_Q = \delta_Q^{(2)}$, and equation 3.34 reduces to equation 3.30. Similarly, for the $[x_2, x_3]$ -plane ($\phi = 90^\circ$), $\epsilon_Q = \epsilon_Q^{(1)}$, $\delta_Q = \delta_Q^{(1)}$, and equation 3.34 reduces to equation 3.33.

Interestingly, equations 3.34–3.35 have exactly the same form as that of the linearized P-wave phase-velocity equations (1.107)–(1.109) in Tsvankin (1997, 2005). This similarity is explained by the identical (orthorhombic) symmetry imposed on both the real and imaginary parts of the stiffness matrix and the assumption of homogeneous wave propagation. An important difference between the coefficient \mathcal{A}_P and phase velocity, however, is that the parameters $\delta_Q^{(1)}$, $\delta_Q^{(2)}$, and $\delta_Q^{(3)}$ include a contribution of the velocity anisotropy, while the velocity function is practically independent of attenuation. Also, as discussed below, the exact coefficient \mathcal{A}_P is influenced by the velocity-anisotropy parameters even for fixed values of $\epsilon_Q^{(1,2)}$ and $\delta_Q^{(1,2,3)}$.

Transversely isotropic models with both vertical (VTI) and horizontal (HTI) symmetry axis represent special cases of orthorhombic media. For VTI media with VTI attenuation, all vertical planes are identical, and there is no velocity or attenuation variation in the horizontal (isotropy) plane:

$$\begin{aligned} \epsilon^{(1)} &= \epsilon^{(2)} = \epsilon, & \epsilon_Q^{(1)} &= \epsilon_Q^{(2)} = \epsilon_Q, \\ \delta^{(1)} &= \delta^{(2)} = \delta, & \delta_Q^{(1)} &= \delta_Q^{(2)} = \delta_Q, \\ \gamma^{(1)} &= \gamma^{(2)} = \gamma, & \gamma_Q^{(1)} &= \gamma_Q^{(2)} = \gamma_Q, \\ \delta^{(3)} &= 0, & \delta_Q^{(3)} &= 0. \end{aligned}$$

Then $\epsilon_Q(\phi) = \epsilon_Q$, $\delta_Q(\phi) = \delta_Q$, and equations 3.34–3.35 yield the VTI result:

$$\mathcal{A}_P^{\text{VTI}} = \mathcal{A}_{P0} (1 + \delta_Q \sin^2 \theta \cos^2 \theta + \epsilon_Q \sin^4 \theta). \quad (3.37)$$

Next, suppose that the symmetry axis of the TI medium (for both velocity and attenuation) points in the x_1 -direction. Then, the isotropy plane coincides with the $[x_2, x_3]$ -plane, and

$$\begin{aligned} \epsilon^{(1)} &= \epsilon_Q^{(1)} = 0, \\ \delta^{(1)} &= \delta_Q^{(1)} = 0, \\ \gamma^{(1)} &= \gamma_Q^{(1)} = 0. \end{aligned}$$

Also, the parameters $\delta^{(3)}$ and $\delta_Q^{(3)}$ are no longer independent because the $[x_1, x_2]$ -plane is equivalent to the $[x_1, x_3]$ -plane. If the velocity anisotropy is weak, $\delta^{(3)} = \delta^{(2)} - 2\epsilon^{(2)}$

(Tsvankin, 1997, 2005). For weak attenuation anisotropy, $\delta_Q^{(3)} = \delta_Q^{(2)} - 2\epsilon_Q^{(2)}$, and equation 3.36 becomes $\epsilon_Q(\phi) = \epsilon_Q^{(2)} \cos^4 \phi + \delta_Q^{(2)} \sin^2 \phi \cos^2 \phi$. Then the P-wave attenuation coefficient 3.34 takes the form

$$\mathcal{A}_P^{\text{HTI}} = \mathcal{A}_{P0} \left[1 + \delta_Q^{(2)} \cos^2 \phi \sin^2 \theta \cos^2 \theta + \left(\epsilon_Q^{(2)} \cos^4 \phi + \delta_Q^{(2)} \sin^2 \phi \cos^2 \phi \right) \sin^4 \theta \right]. \quad (3.38)$$

3.7.3 Parameters for P-wave attenuation

The linearized P-wave attenuation coefficient 3.34 is independent of the parameters \mathcal{A}_{S0} , $\gamma_Q^{(1)}$, and $\gamma_Q^{(2)}$, which are primarily responsible for shear-wave attenuation. Numerical tests show that this conclusion remains valid for models with strong attenuation and pronounced velocity and attenuation anisotropy. As illustrated by Figure 3.4, the dependence of \mathcal{A}_P on the shear-wave vertical attenuation coefficient \mathcal{A}_{S0} becomes noticeable only for extremely large attenuation (i.e., uncommonly small values of Q_{55}). The influence of the parameters $\gamma_Q^{(1)}$ and $\gamma_Q^{(2)}$ on the coefficient \mathcal{A}_P (not shown here) for typical moderately attenuative models is also negligible.

Therefore, for a fixed orientation of the symmetry planes and fixed velocity parameters, P-wave attenuation is controlled by the reference value \mathcal{A}_{P0} and five attenuation-anisotropy parameters – $\epsilon_Q^{(1)}$, $\epsilon_Q^{(2)}$, $\delta_Q^{(1)}$, $\delta_Q^{(2)}$, and $\delta_Q^{(3)}$. An equivalent result for velocity anisotropy was obtained by Tsvankin (1997, 2005), who showed that the P-wave phase-velocity function in orthorhombic media is governed just by the vertical velocity and five ϵ and δ parameters. As demonstrated below, however, while the velocity function is almost independent of attenuation, the P-wave attenuation coefficient does depend on the velocity anisotropy, even if all relevant attenuation-anisotropy parameters are held constant.

3.7.4 Accuracy of the linearized solution

To evaluate the accuracy of the weak-anisotropy approximation (3.34) outside the symmetry planes, I compare it with the exact coefficient \mathcal{A}_P (equation 3.2) for a model with pronounced orthorhombic attenuation (Figure 3.5). The velocity parameters correspond to the moderately anisotropic model of (Schoenberg and Helbig, 1997). Since no measurements of the attenuation-anisotropy parameters are available, each of them is set to be twice as large as the corresponding velocity-anisotropy parameter (e.g., $\epsilon_Q^{(2)} = 2\epsilon^{(2)}$).

As expected, the weak-anisotropy approximation gives satisfactory results for near-vertical propagation directions with polar angles up to about 30° . The error becomes more significant for intermediate propagation angles in the range $30^\circ < \theta < 75^\circ$. When the incidence plane is close to either vertical symmetry plane (i.e., the azimuth ϕ approaches 0° or 90°), the approximate solution also yields an accurate estimate of \mathcal{A}_P near the horizontal direction. Overall, the error of the weak-anisotropy approximation for the full range of polar and azimuthal angles is less than 10%. Note that while the velocity anisotropy for this model is moderate (both $\epsilon^{(1)}$ and $\epsilon^{(2)}$ are about 0.3), the attenuation anisotropy is much more pronounced. This and other tests for a suite of orthorhombic models with weak or moderate velocity anisotropy confirm that equation 3.34 gives an adequate qualitative

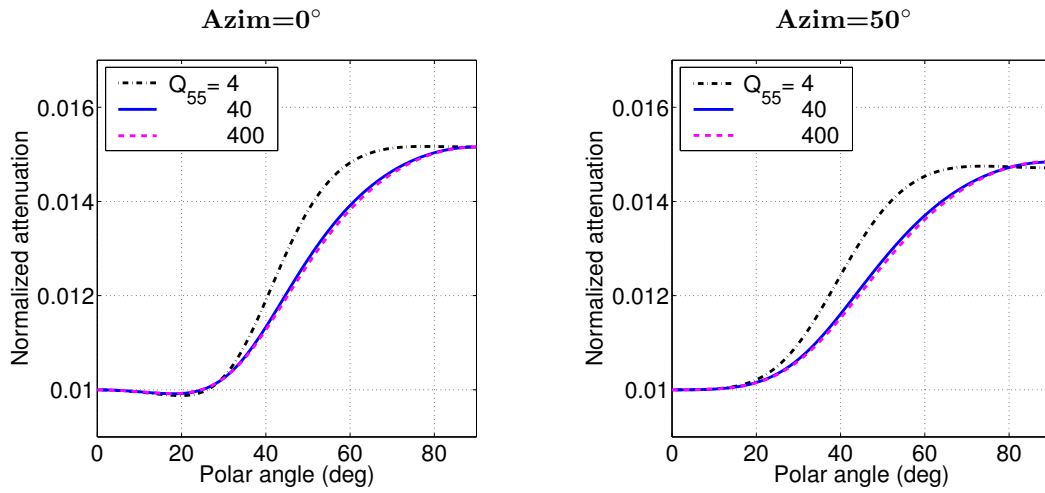


Figure 3.4. Influence of the parameter $\mathcal{A}_{S0} = 1/(2Q_{55})$ (marked on the plot) on the exact P-wave attenuation coefficient. The velocity parameters correspond to an orthorhombic model formed by vertical cracks embedded in a VTI background (Schoenberg and Helbig, 1997): $V_{P0} = 2.437$ km/s, $V_{S0} = 1.265$ km/s, $\epsilon^{(1)} = 0.329$, $\epsilon^{(2)} = 0.258$, $\delta^{(1)} = 0.083$, $\delta^{(2)} = -0.078$, $\delta^{(3)} = -0.106$, $\gamma^{(1)} = 0.182$, and $\gamma^{(2)} = 0.0455$. The P-wave vertical attenuation coefficient is $\mathcal{A}_{P0} = 0.01$ ($Q_{33} = 50$); each attenuation-anisotropy parameter is twice the corresponding velocity-anisotropy parameter: $\epsilon_Q^{(1)} = 0.658$, $\epsilon_Q^{(2)} = 0.516$, $\delta_Q^{(1)} = 0.166$, $\delta_Q^{(2)} = -0.156$, $\delta_Q^{(3)} = -0.212$, $\gamma_Q^{(1)} = 0.364$, and $\gamma_Q^{(2)} = 0.091$.

description of P-wave attenuation (under the assumption of homogeneous wave propagation) even if the attenuation anisotropy is pronounced (e.g., $\epsilon^{(2)} = 0.8$).

To identify the source of errors in the weak-anisotropy approximation, I repeat the test in Figure 3.5 using a purely isotropic velocity model (Figure 3.6). The approximate solution (dashed lines) in Figure 3.6 coincides with that in Figure 3.5 because both models have identical attenuation-anisotropy parameters. The exact coefficient \mathcal{A}_P (solid lines), however, is influenced by the velocity-anisotropy parameters in such a way that the error of the weak-anisotropy approximation almost disappears when the velocity field is isotropic (Figure 3.6).

Hence, the accuracy of the approximation 3.34 is controlled primarily by the strength of the velocity anisotropy, even if the magnitude of the attenuation anisotropy is much higher. This can be explained by the multiple linearizations in the velocity-anisotropy parameters involved in deriving equations E.4 and E.7.

It should be emphasized that the influence of different subsets of the velocity-anisotropy parameters on the attenuation coefficient \mathcal{A}_P varies with the azimuth ϕ . As illustrated in Figure 3.7, the contribution of the parameters defined in the $[x_1, x_3]$ -plane (the azimuth $\phi = 0^\circ$) decreases away from that plane and completely vanishes in the orthogonal direction. Note that according to the Christoffel equation (3.13), the P-wave attenuation coefficient in the $[x_2, x_3]$ -plane ($\phi = 90^\circ$) is indeed fully independent of the velocity- and attenuation-anisotropy parameters defined in the other two symmetry planes. Likewise, the influence on \mathcal{A}_P of the parameters defined in the $[x_2, x_3]$ -plane (the superscript “(1)”) is largest for azimuths close to 90° .

3.8 Summary and observations

The attenuation coefficients of P-, S_1 -, and S_2 -waves in orthorhombic media with orthorhombic attenuation depend on the orientation of the symmetry planes, nine velocity parameters and nine components of the quality-factor matrix. The large number of independent parameters, compounded by the coupling between the attenuation and velocity anisotropy, makes attenuation analysis for this model difficult. Here, I demonstrated that the description of the attenuation coefficients can be substantially simplified by introducing a set of attenuation-anisotropy parameters similar to Tsvankin’s notation for the orthorhombic velocity function.

The equivalence between the Christoffel equation in the symmetry planes of orthorhombic and VTI media, established previously for purely elastic media, holds in the presence of orthorhombic attenuation. Therefore, the symmetry-plane attenuation coefficients of all three modes can be obtained by simply adapting the known VTI equations. Moreover, the Thomsen-style notation for attenuative VTI media can be extended to orthorhombic models following the approach suggested by Tsvankin for velocity anisotropy. The parameter set introduced here includes two vertical P- and S-wave attenuation coefficients, \mathcal{A}_{P0} and \mathcal{A}_{S0} , and seven dimensionless anisotropy parameters, $\epsilon_Q^{(1,2)}$, $\delta_Q^{(1,2,3)}$, and $\gamma_Q^{(1,2)}$.

Adaptation of the linearized VTI equations allows me to obtain concise symmetry-plane attenuation coefficients of P-, S_1 -, and S_2 -waves valid for small attenuation and weak

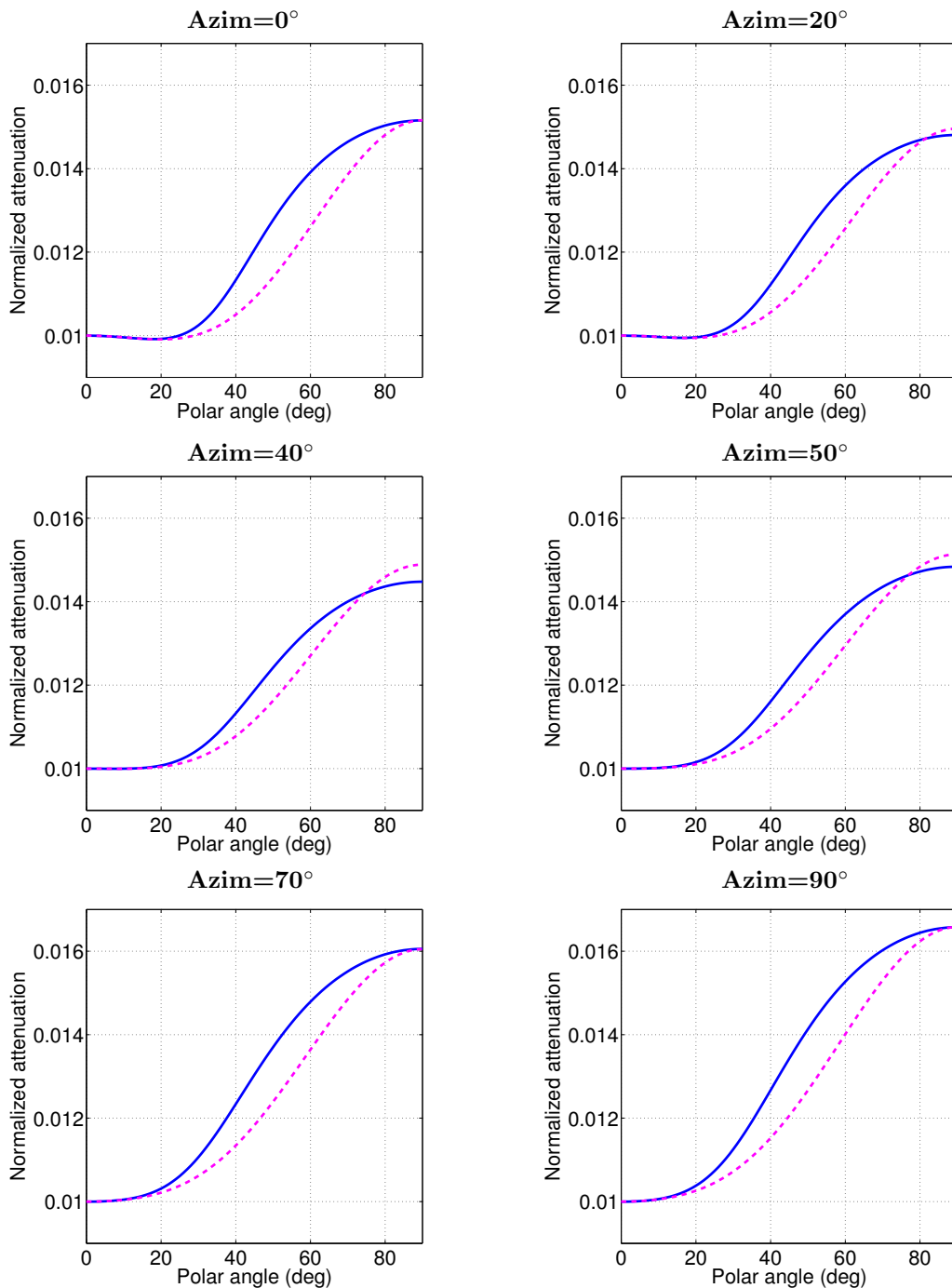


Figure 3.5. Comparison of the exact coefficient \mathcal{A}_P (solid curves) with the linearized approximation 3.34 (dashed) for an orthorhombic medium with orthorhombic attenuation. The model parameters are the same as in Figure 3.4 ($Q_{55} = 40$; $\mathcal{A}_{S0} = 0.0125$).

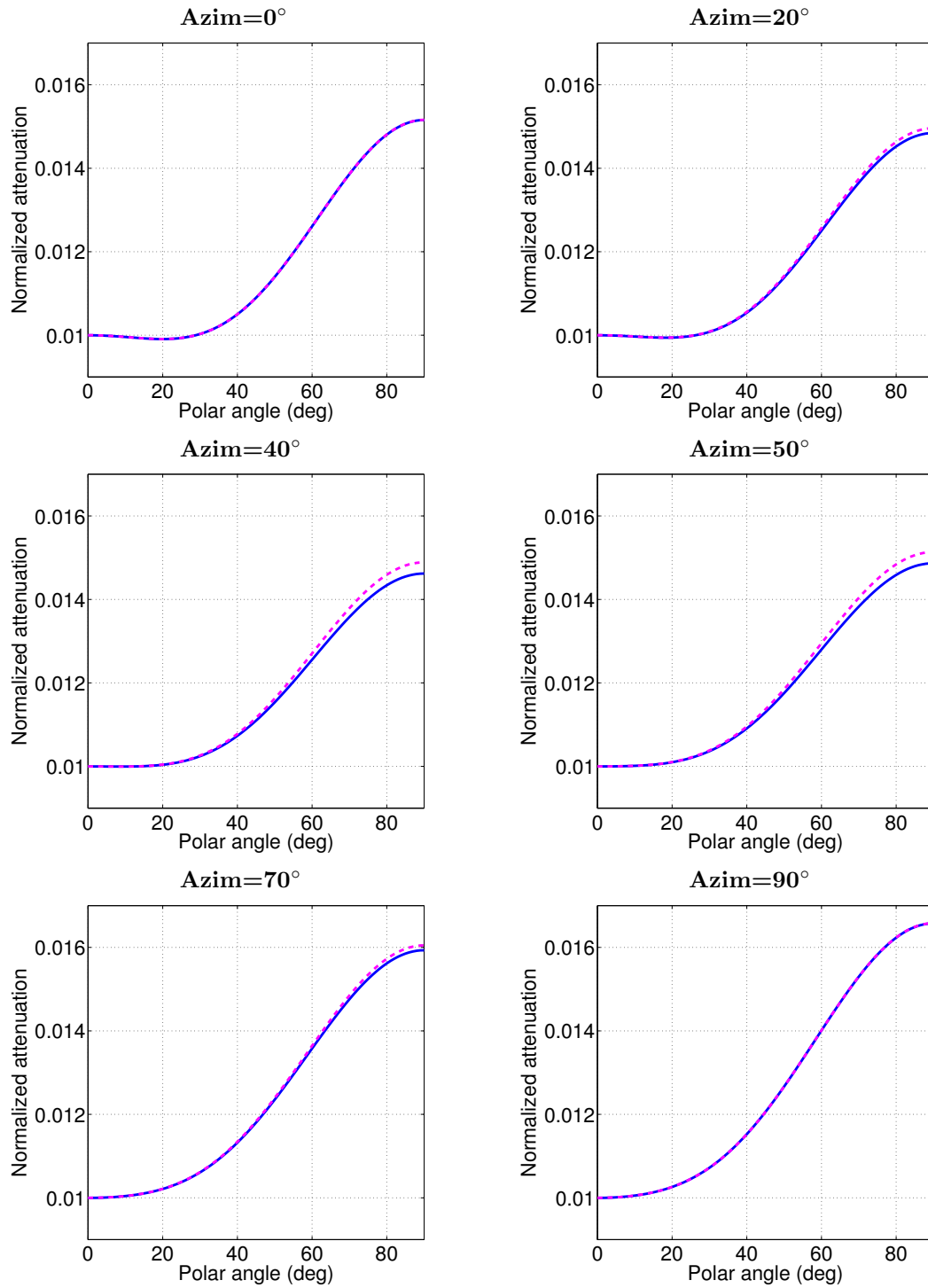


Figure 3.6. Comparison of the exact coefficient \mathcal{A}_P (solid curves) with the linearized approximation 3.34 (dashed) for a medium with orthorhombic attenuation but a purely isotropic velocity function. The attenuation parameters are the same as in Figures 3.4 and 3.5, but the velocity $V_{P0} = 2.437$ km/s is constant in all directions.

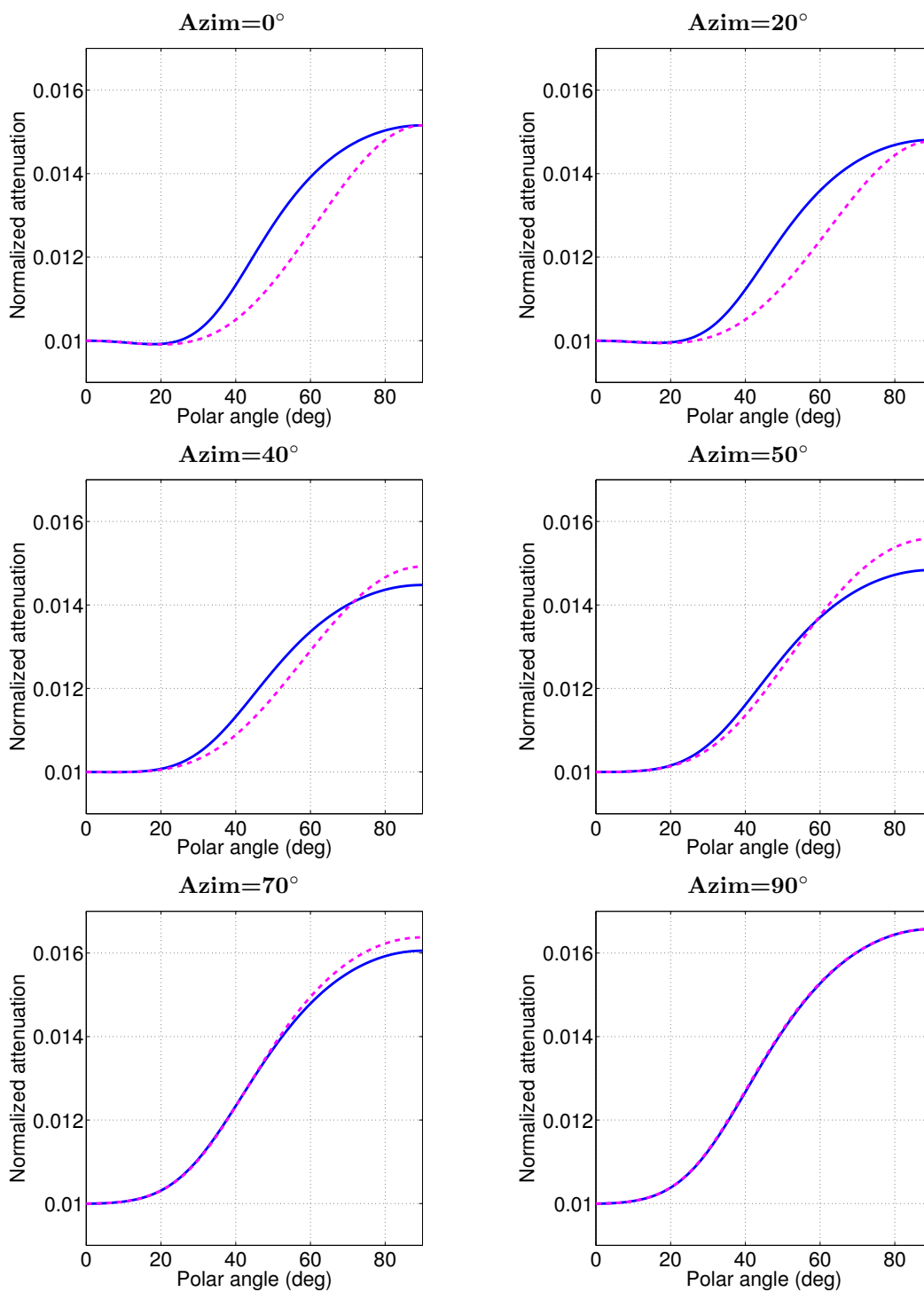


Figure 3.7. Influence of the velocity anisotropy on the exact attenuation coefficient \mathcal{A}_P . The solid curves are computed for the orthorhombic model with orthorhombic attenuation from Figures 3.4 and 3.5. The dashed curves are obtained by setting the velocity-anisotropy parameters $\epsilon^{(2)}$, $\delta^{(2)}$, and $\gamma^{(2)}$ defined in the $[x_1, x_3]$ -plane (azimuth = 0°) to zero; all other model parameters are unchanged.

velocity and attenuation anisotropy. Furthermore, linearization of the Christoffel equation in the attenuation-anisotropy parameters yields the approximate P-wave attenuation coefficient \mathcal{A}_P outside the symmetry planes as a simple function of \mathcal{A}_{P0} , $\epsilon_Q^{(1,2)}$, and $\delta_Q^{(1,2,3)}$. The influence of the parameters \mathcal{A}_{S0} and $\gamma_Q^{(1,2)}$ on P-wave attenuation remains negligible even for large attenuation anisotropy.

The approximate coefficient \mathcal{A}_P has the same form as the approximate P-wave phase-velocity function in terms of Tsvankin's velocity parameters and can be represented by the VTI equation with the azimuthally varying parameters ϵ_Q and δ_Q . This equivalence between the linearized equations for attenuation and velocity anisotropy stems from the identical (orthorhombic) symmetry of the real and imaginary parts of the stiffness tensor and the assumption of homogeneous wave propagation. Still, there are important differences between the treatment of velocity and attenuation anisotropy. The analysis shows that in the absence of pronounced velocity dispersion the influence of attenuation (i.e., of the imaginary part of the stiffness tensor) on velocity is practically negligible. In contrast, the definitions of the attenuation-anisotropy parameters $\delta_Q^{(1,2,3)}$ include the velocity parameters $\delta^{(1,2,3)}$.

Also, the exact attenuation coefficient \mathcal{A}_P varies with the velocity-anisotropy parameters even for fixed values of $\delta_Q^{(1,2,3)}$. Moreover, the accuracy of the linearized equation for \mathcal{A}_P is controlled to a large degree by the strength of the velocity anisotropy. Numerical tests demonstrate that the approximate \mathcal{A}_P remains close to the exact value even for large (by absolute value) attenuation-anisotropy parameters provided the velocity anisotropy is relatively weak.

Thus, the P-wave attenuation coefficient is primarily governed by the orientation of the symmetry planes and six (instead of nine) attenuation-anisotropy parameters: \mathcal{A}_{P0} , $\epsilon_Q^{(1,2)}$, and $\delta_Q^{(1,2,3)}$. However, because of the non-negligible influence of the velocity anisotropy on \mathcal{A}_P , accurate inversion of attenuation measurements for orthorhombic media requires anisotropic velocity analysis as well. Also, knowledge of the anisotropic velocity field is required to obtain the normalized attenuation coefficient \mathcal{A} (equation 2.11) and to correct for the difference between the phase attenuation coefficient studied here and the group attenuation coefficient responsible for the amplitude decay along seismic rays. Overall, these results provide an analytic foundation for estimating the attenuation-anisotropy parameters from wide-azimuth seismic data.

Whereas this study is restricted to homogeneous wave propagation, the inhomogeneity angle in layered attenuative media is not necessarily small (see Chapter 6). I also assumed that the symmetry planes for the velocity and attenuation functions are aligned, which is justified for effective azimuthally anisotropic media caused by systems of parallel fractures. Still, for more complicated porous fractured media or models with depth-varying fracture direction (see Chapter 5) this assumption may break down, and most of the discussion here would have to be revised. Also, I did not take into account possible frequency dependence of the quality-factor matrix in the seismic frequency band. If this dependence is not negligible, the attenuation-anisotropy parameters also become frequency-dependent, although their definitions remain the same.

Chapter 4

Physical modeling and analysis of P-wave attenuation anisotropy for TI media

4.1 Summary

I analyze measurements of the P-wave attenuation coefficient in a transversely isotropic sample made of phenolic material. Using the anisotropic version of the spectral-ratio method, I estimate the group (effective) attenuation coefficient of P-waves transmitted through the sample for a wide range of propagation angles (from 0° to 90°) with the symmetry axis. Correction for the difference between the group and phase angles helps to obtain the normalized phase attenuation coefficient \mathcal{A} governed by the Thomsen-style attenuation-anisotropy parameters ϵ_Q and δ_Q . Whereas the symmetry axis of the angle-dependent coefficient \mathcal{A} practically coincides with that of the velocity function, the magnitude of the attenuation anisotropy far exceeds that of the velocity anisotropy. The quality factor Q increases more than tenfold from the symmetry (slow) direction to the isotropy plane (fast direction). Inversion of the coefficient \mathcal{A} using the Christoffel equation yields large negative values of ϵ_Q and δ_Q .

The robustness of these results critically depends on several factors, such as the availability of an accurate anisotropic velocity model and adequacy of the “homogeneous” concept of wave propagation, as well as the choice of the frequency band. The methodology discussed here can be extended to field measurements of anisotropic attenuation needed for AVO (amplitude-variation-with-offset) analysis, amplitude-preserving migration, and seismic fracture detection.

4.2 Introduction

Although experimental measurements of attenuation, both in the field and on rock samples, are relatively rare, they indicate that the magnitude of attenuation anisotropy often exceeds that of velocity anisotropy (e.g., Tao and King, 1990; Arts and Rasolofosaon, 1992; Prasad and Nur, 2003; Shi and Deng, 2005). For example, according to the measurements of Hosten et al. (1987) for an orthorhombic sample made of composite material, the quality factor for P-waves changes from $Q \approx 6$ in the vertical direction to $Q \approx 35$ in the horizontal direction. Hosten et al. (1987) also show that the symmetry of the attenuation coefficient closely follows that of the velocity function.

Here, I extend the spectral-ratio method to anisotropic media and apply it to P-wave

transmission data acquired in a symmetry plane of a phenolic sample. Fitting the theoretical normalized attenuation coefficient \mathcal{A} to the measurements for a wide range of propagation angles yields estimates of the attenuation-anisotropy parameters ϵ_Q and δ_Q developed in Chapter 2. Although the experiment was performed for a synthetic material, the results are indicative of the high potential of attenuation-anisotropy analysis for field seismic data.

4.3 Spectral-ratio method for anisotropic attenuation

The spectral-ratio method is often used to estimate the attenuation coefficient in both physical modeling and field surveys. For laboratory experiments, application of this method typically involves amplitude measurements made under identical conditions for the sample of interest and for a reference purely elastic (non-attenuative) sample.

The frequency-domain displacement of the direct wave recorded for the reference homogeneous sample [the superscript “(0)”] can be written as

$$U^{(0)}(\omega) = S(\omega) G^{(0)}(\mathbf{x}^{(0)}) e^{i\omega(t-|\mathbf{x}^{(0)}|/V_G^{(0)})}, \quad (4.1)$$

where \mathbf{x} is the vector connecting the source and receiver, V_G is the group (ray) velocity in the direction \mathbf{x} , $S(\omega)$ is the spectrum of the source pulse, and the factor $G(\mathbf{x})$ incorporates the radiation pattern of the source and the geometrical spreading along the raypath. Similarly, the frequency-domain displacement for the attenuative sample [the superscript “(1)”] has the form

$$U^{(1)}(\omega) = S(\omega) G^{(1)}(\mathbf{x}^{(1)}) e^{-k_G^I |\mathbf{x}^{(1)}|} e^{i\omega(t-|\mathbf{x}^{(1)}|/V_G^{(1)})}; \quad (4.2)$$

k_G^I is the amplitude decay factor (attenuation coefficient) in the group (ray) direction. The logarithm of the amplitude ratio can be found from equations 4.1 and 4.2 as

$$\ln \left| \frac{U^{(1)}}{U^{(0)}} \right| = \ln \left(\frac{G^{(1)}}{G^{(0)}} \right) - k_G^I |\mathbf{x}^{(1)}|. \quad (4.3)$$

The frequency dependence of the term $G^{(1)}/G^{(0)}$ is usually considered to be negligible in the frequency range of interest. Then the slope of the function $\ln \left| \frac{U^{(1)}}{U^{(0)}} \right|$ yields the “local” value of the inverse Q -factor in the source-receiver direction. If this slope changes with frequency ω , then the assumption of frequency-independent Q is not valid.

In isotropic media with isotropic (angle-invariant) attenuation, the group attenuation coefficient k_G^I measured along the raypath coincides with the phase (plane-wave) attenuation coefficient k^I . For anisotropic media with anisotropic attenuation, however, these two coefficients generally differ. If wave propagation is homogeneous (i.e., the inhomogeneity angle is negligible), the group and phase attenuation coefficients are related by the equation $k_G^I = k^I \cos \hat{\psi}$, where $\hat{\psi}$ is the angle between the group- and phase-velocity vectors (Zhu and Tsvalkin, 2004).

Then the normalized phase attenuation coefficient introduced above is given by

$$\mathcal{A} = \frac{k^I}{k} = \frac{k^I}{\omega} V = \frac{k_G^I}{\omega} \frac{V}{\cos \hat{\psi}}, \quad (4.4)$$

where V is the phase velocity that corresponds to the source-receiver (group) direction (i.e., the velocity of the plane wave tangential to the wavefront at the receiver location). Therefore, the coefficient \mathcal{A} can be found as the measured slope of the group attenuation coefficient $k_G^I(\omega)$ scaled by the ratio $V/\cos \hat{\psi}$.

Here, I employ the following procedure of inverting P-wave attenuation measurements for the attenuation-anisotropy parameters. First, the slope of the logarithmic spectral ratio in equation 4.3 expressed as a function of ω is used to estimate k_G^I/ω . Second, using the velocity parameters of the sample (assumed to be known), I compute the phase velocity V and angle $\hat{\psi}$ and substitute them into equation 4.4 to find the coefficient \mathcal{A} . Third, the measurements of \mathcal{A} for a wide range of phase angles are inverted for the attenuation-anisotropy parameters ϵ_Q and δ_Q . Approximate values of ϵ_Q and δ_Q can be found in a straightforward way from the linearized equation 2.36. More accurate results, however, are obtained by nonlinear inversion based on the exact Christoffel equation B.1.

Because of the dependence of the exact coefficient \mathcal{A} (Chapter 2) on the velocity parameters and the contribution of the velocity anisotropy to equation 4.4, estimation of ϵ_Q and δ_Q requires knowledge of the anisotropic velocity field. Since the influence of attenuation on velocity typically is a second-order factor (Zhu and Tsvankin, 2005), anisotropic velocity analysis can be performed prior to inverting the attenuation measurements. In the inversion below I use the results of Dewangan (2004) and Dewangan et al. (2006), who estimated the velocity-anisotropy parameters of the same phenolic sample by inverting reflection traveltimes of PP- and PS-waves.

4.4 Experimental setup and data processing

The goal of this chapter is to measure the directional dependence of the P-wave attenuation coefficient in a composite sample and invert these measurements for the attenuation-anisotropy parameters ϵ_Q and δ_Q . The material was XX-paper-based phenolic composed of thin layers of paper bonded with phenolic resin. This fine layering produces an effective anisotropic medium on the scale of the predominant wavelength. The sample was prepared by Dewangan (2004; Figure 4.1), who pasted phenolic blocks together at an angle, which resulted in a transversely isotropic model with the symmetry axis tilted from the vertical by 70° (TTI medium). Laser-Doppler measurements of the vertical component of the wavefield were made by Kasper van Wijk in the Physical Acoustic Laboratory at CSM.

Dewangan et al. (2006) show that the TTI model adequately explains the kinematics of multicomponent (P, S, and PS) data in the vertical measurement plane that contains the symmetry axis (the symmetry-axis plane). Although phenolic materials are generally known to be orthorhombic (e.g., Grechka et al., 1999), body-wave velocities and polarizations in the symmetry planes of orthorhombic media can be described by the corresponding TI

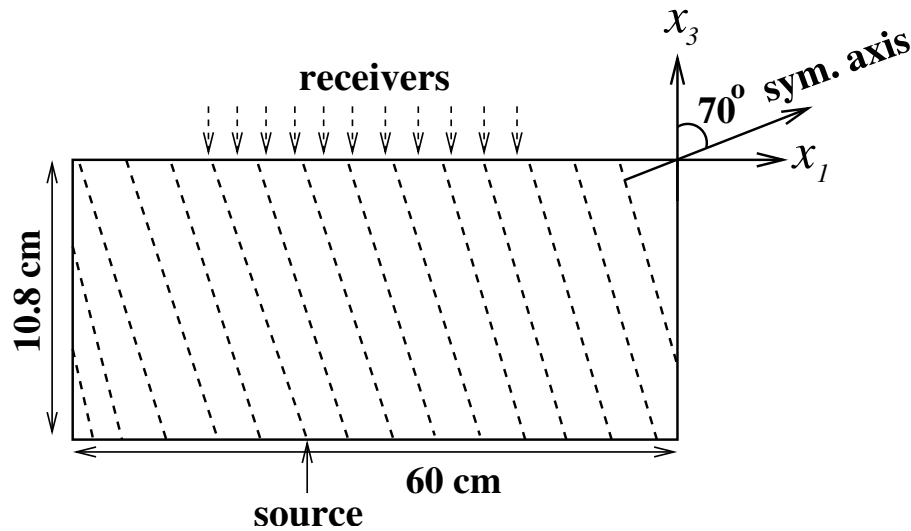


Figure 4.1. Physical model of a TI layer with the symmetry axis tilted at 70° (from Dewangan et al., 2006). The transmitted wavefield is excited by an ultrasonic contact transducer at the bottom of the model and recorded by a laser vibrometer at different locations along the top.

equations (Tsvankin, 1997, 2005).

The original purpose in acquiring the transmission data used here (Figures 4.1 and 4.2a) was to verify the accuracy of the parameter-estimation results obtained by Dewangan (2004) and Dewangan et al. (2006). The P-wave source (a flat-faced cylindrical piezoelectric contact transducer) was fixed at the bottom of the model, and the wavefield was recorded by a laser vibrometer at intervals of 2 mm. The spread of the receiver locations was wide enough to cover a full range of propagation angles (from 0° to 90°) with respect to the (tilted) symmetry axis.

To perform attenuation analysis, I separated the first (direct) arrival by applying a Gaussian window to the raw data. The amplitude spectrum of the windowed first arrival obtained by filtering out the low ($f < 5$ kHz) and high ($f > 750$ kHz) frequencies is shown in Figure 4.2b. An aluminum block with negligibly small attenuation served as the reference model. The reference trace was acquired by a receiver located directly opposite the source (Figure 4.3).

For each receiver position at the surface of the phenolic sample, I divided the spectrum of the windowed recorded trace by that of the reference trace to compute the spectral ratio (equation 4.3). Records with a low signal-to-noise ratio were excluded from the analysis. Note that Figures 4.2b and 4.3 reveal gaps in the frequency spectrum (around 170 and 200 kHz, respectively), which are likely related to the mechanical properties of the piezoelectric source. To estimate the group attenuation coefficient k_G^I from equation 4.3, I chose a

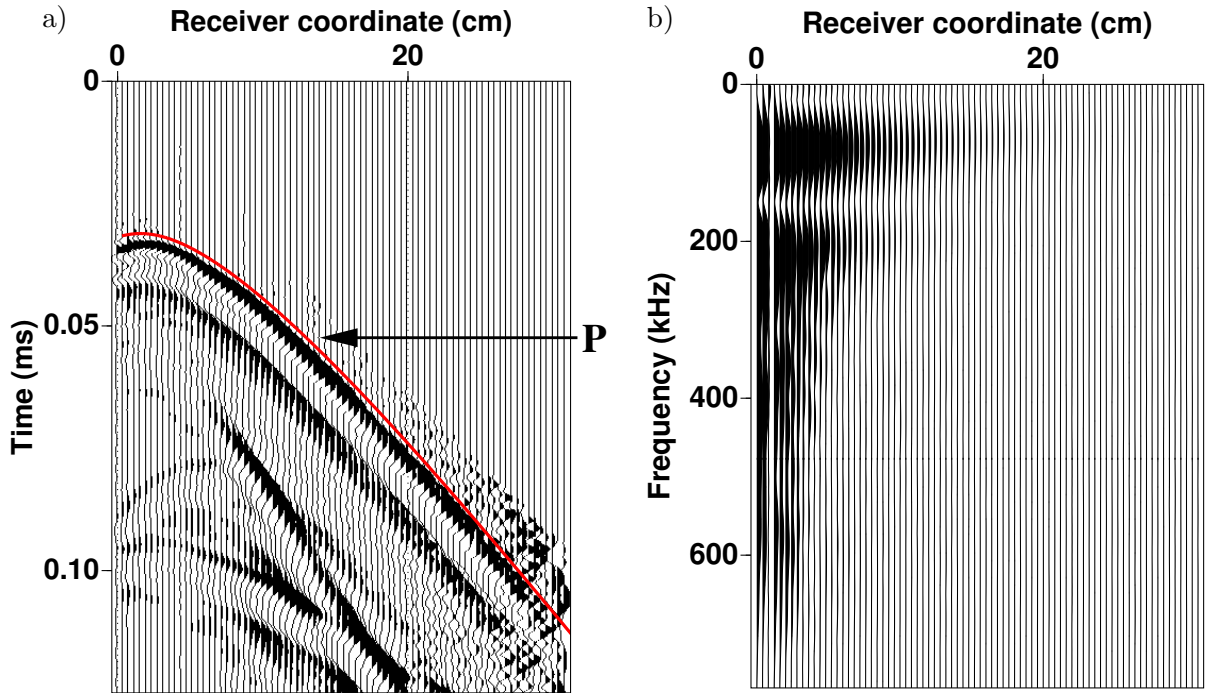


Figure 4.2. (a) Raw transmission data excited by a P-wave transducer in the phenolic sample, and (b) the amplitude spectrum of the windowed first arrival. The solid line is the P-wave traveltime modeled by Dewangan et al. (2006) using the inverted parameters from Figure 4.4. The time sampling interval is $2\mu\text{s}$, and the width of the Gaussian window is 40 samples.

frequency band (60–110 kHz) away from the spectral gaps. According to the spectral-ratio method described above, the relevant elements Q_{ij} in that frequency band are assumed to be constant.

4.5 Evaluation of attenuation anisotropy

The parameters of the TTI velocity model needed to process the attenuation measurements were obtained by Dewangan et al. (2006) from reflection PP and PS data (Figure 4.4). Tilted transverse isotropy is described by the the P- and S-wave velocities in the symmetry direction (V_{P0} and V_{S0} , respectively), Thomsen anisotropy parameters ϵ and δ defined with respect to the symmetry axis, the angle ν between the symmetry axis and the vertical, and the thickness z of the sample. The known values of $\nu = 70^\circ$ and $z = 10.8$ cm were accurately estimated from the reflection data, which confirms the robustness of the velocity-inversion

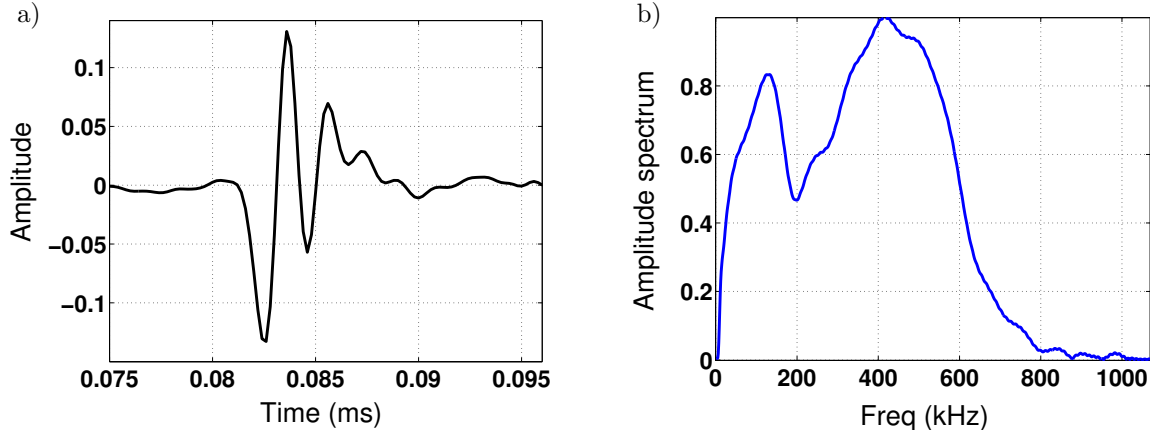


Figure 4.3. Reference trace for vertical propagation through an aluminum block (a), and its amplitude spectrum (b).

algorithm.

4.5.1 Estimation of the attenuation-anisotropy parameters

Using the computed slope of the function $k_G^I(\omega)$ for each receiver location and the velocity parameters of the sample (Figure 4.4), I found the normalized phase attenuation coefficient \mathcal{A} from equation 4.4. Note that the difference between the group and phase attenuation coefficients for this model does not exceed 6%. The coefficient \mathcal{A} exhibits an extremely pronounced variation between the slow (0°) and fast (90°) directions (Figure 4.5). The largest attenuation is observed along the symmetry axis ($\theta = 0^\circ$), where the P-wave phase velocity reaches its minimum value. Since the symmetry direction is orthogonal to the multiple thin layers bonded together to form the model, the rapid increase in attenuation toward $\theta = 0^\circ$ could be expected.

The polar plot of the attenuation coefficient (Figure 4.6) indicates that the symmetry axis of the function $\mathcal{A}(\theta)$ is close to that for the velocity measurements. Although I did not acquire data for angles exceeding 90° to reconstruct a more complete angle variation of \mathcal{A} , the direction orthogonal to the layering should indeed represent the symmetry axis for all physical properties of the model. To quantify the attenuation anisotropy, I used the Christoffel equation B.1 to estimate the best-fit parameters $\mathcal{A}_{P0} = 0.16$ ($Q_{33} = 3.2$), $\epsilon_Q = -0.92$, and $\delta_Q = -1.84$. The small-attenuation, weak-anisotropy approximation (2.36) yields similar values ($\mathcal{A}_{P0} = 0.16$, $\epsilon_Q = -0.86$, and $\delta_Q = -1.91$) despite the large magnitude of the angle variation of \mathcal{A} (Figure 4.6).

Whereas the fact that the largest attenuation coefficient for this model is observed at the velocity minimum is predictable, the extremely low value of $Q_{33} = 3.2$ is somewhat surprising. It should be mentioned, however, that the estimates of the attenuation coeffi-

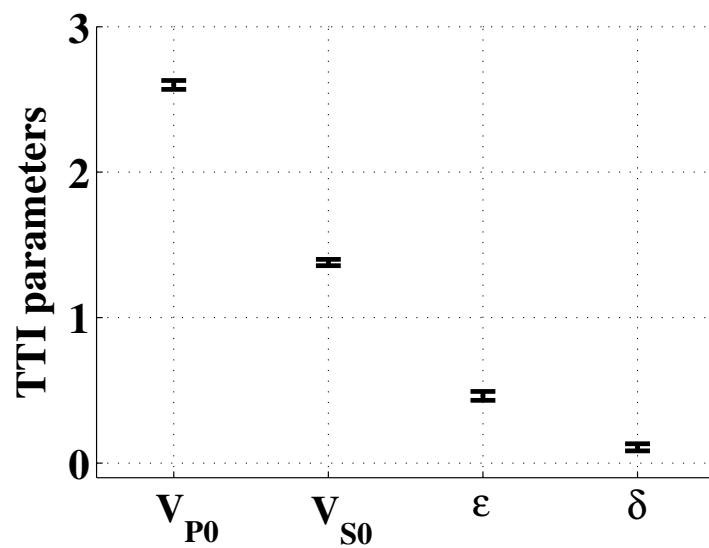


Figure 4.4. Velocity-anisotropy parameters of the TTI model estimated from reflection traveltimes of PP- and PS-waves in the symmetry-axis plane (after Dewangan et al., 2006). The mean values are $V_{P0} = 2.6$ km/s, $V_{S0} = 1.38$ km/s, $\epsilon = 0.46$, and $\delta = 0.11$. The error bars mark the standard deviations in each parameter obtained by applying the inversion algorithm to 200 realizations of input reflection traveltimes contaminated by Gaussian noise. The standard deviation of the noise was equal to $1/8$ of the dominant period of the reflection arrivals.

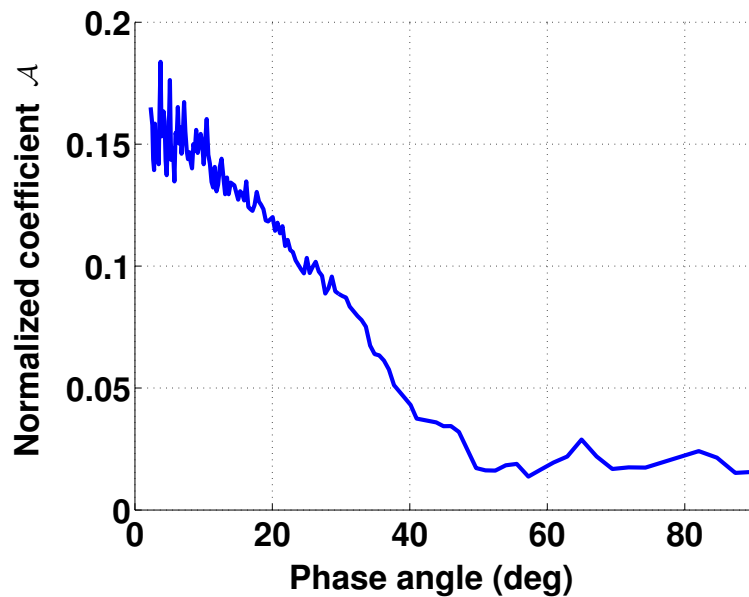


Figure 4.5. Measured normalized attenuation coefficient \mathcal{A} as a function of the phase angle θ with the symmetry axis.

cient near the symmetry axis may have been distorted by the relatively low reliability of amplitude measurements at long offsets corresponding to small angles θ (Figure 4.1). Problems in applying this methodology for large source-receiver distances may be related to such factors as the frequency-dependent geometrical spreading and the increased influence of heterogeneity.

An essential assumption behind the estimates of the attenuation-anisotropy parameters is that the inhomogeneity angle is negligibly small. Although the modeled attenuation coefficient provides a good fit to the measured curve, it is not clear how significant the inhomogeneity angle for this model may be and how it can influence the parameter-estimation results. Moreover, the coupling of the source with the reference aluminum block differs from that of the phenolic sample, which can influence the source spectra and cause errors in the attenuation estimation.

4.5.2 Uncertainty analysis

It is important to evaluate the uncertainty of the attenuation measurements caused by errors in the velocity-anisotropy parameters. Using the standard deviations in the parameters V_{P0} , ϵ , δ , and ν provided by Dewangan et al. (2006), I repeated the inversion procedure for 50 realizations of the input TTI velocity model (Figure 4.7). Although the variation of the estimated attenuation coefficients in some directions is substantial, the mean values of the attenuation-anisotropy parameters obtained from the best-fit curve $\mathcal{A}(\theta)$ are close to

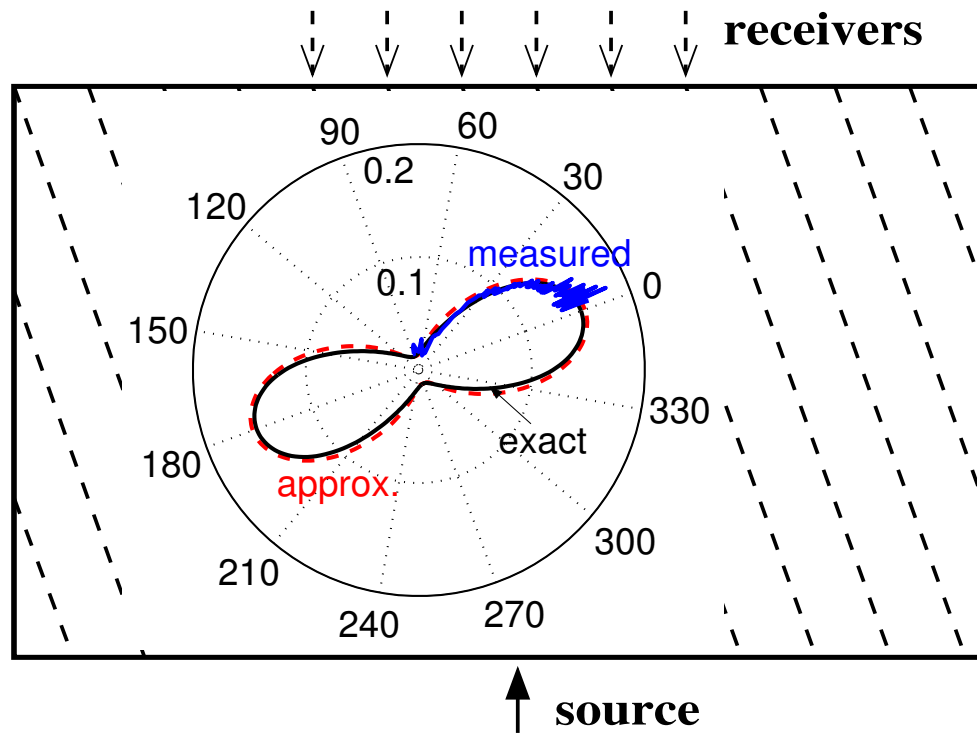


Figure 4.6. Polar plot of the attenuation coefficient against the background of the physical model. The estimated function $\mathcal{A}(\theta)$ from Figure 4.5 (blue curve) was used to find the best-fit attenuation coefficient from the Christoffel equation (black) and from approximation (2.36) (dashed). The numbers on the perimeter indicate the phase angle with the symmetry axis.

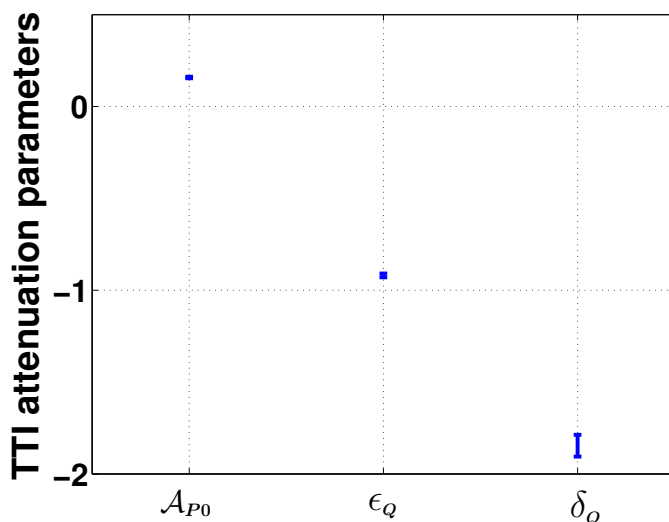


Figure 4.7. Influence of errors in the velocity model on the recovered attenuation parameters. The error bars mark the standard deviation in each parameter obtained by applying the inversion algorithm with 50 realizations of the input TTI velocity model. The standard deviations in the TTI parameters are taken from Dewangan et al. (2006).

those listed above. The standard deviations are 2% for \mathcal{A}_{P0} , 0.01 for ϵ_Q , and 0.06 for δ_Q , which indicates that the influence of moderate errors in the velocity field on these results is not significant.

Another potential source of uncertainty in the attenuation-anisotropy measurements is the choice of the frequency range used in the spectral-ratio method. Figure 4.8 shows the distribution of 50 realizations of the attenuation-anisotropy parameters obtained for variable upper and lower bounds of the frequency range. The mean values of the estimated parameters are $\mathcal{A}_{P0} = 0.16$ ($Q_{33} = 3.3$), $\epsilon_Q = -0.90$, and $\delta_Q = -1.94$, with the standard deviations equal to 3% for \mathcal{A}_{P0} , 0.06 for ϵ_Q , and 0.15 for δ_Q . Therefore, the sensitivity of the attenuation-anisotropy parameters to moderate variations in the bounds of the frequency band is not negligible.

In accordance with the spectral-ratio method, I assume the quality-factor components Q_{ij} to be frequency-independent within the frequency range used for the analysis. However, observed variations of the slope of the coefficient k_G^I in the frequency domain indicate that the attenuation-anisotropy parameters may vary with frequency.

4.6 Discussion

While the large difference between the attenuation coefficients in the two principal directions is unquestionable, the accuracy of the measurements strongly depends on several assumptions. First, the radiation pattern of the source and the geometrical spreading are

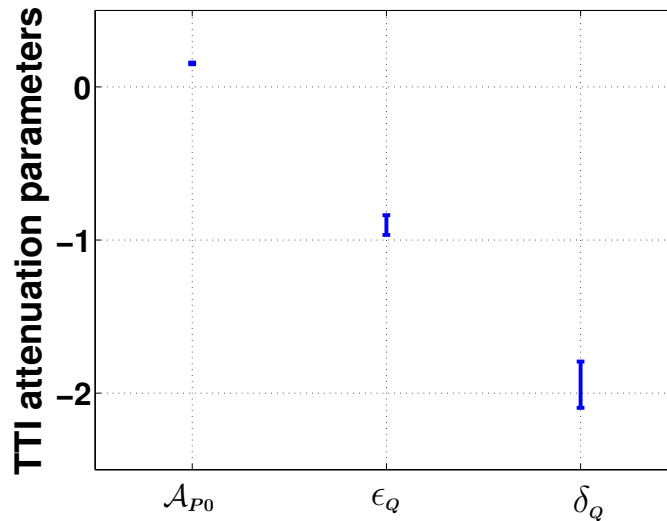


Figure 4.8. Influence of the frequency range used in the spectral-ratio method on the recovered attenuation parameters. The error bars mark the standard deviation in each parameter obtained by applying the inversion algorithm with 50 realizations of the upper and lower bounds of the frequency range. The upper bound was changed randomly between 88 kHz and 132 kHz, and the lower bound between 44 kHz and 66 kHz.

taken to be frequency-independent in the frequency range used in the spectral-ratio method. Because of the possible influence of heterogeneity, it is desirable to test the validity of this assumption, particularly for relatively large source-receiver offsets. For example, the experiment can be redesigned by making measurements on two different-size samples of the same phenolic material. Then it would be possible to compute the spectral ratios for arrivals propagating in the same direction and recorded at different distances from the source. Then, the potential frequency dependence of the radiation pattern would be removed from the attenuation measurement along with the spectrum of the source pulse, and no reference trace would be required.

Second, the analytic solutions for the attenuation coefficient are based on the assumption of homogeneous wave propagation (i.e., the inhomogeneity angle is assumed to be negligible). For strongly attenuative models with pronounced attenuation anisotropy, this assumption may cause errors in the interpretation of attenuation measurements. In particular, if the model is layered, the inhomogeneity angle is governed by the boundary conditions and can be significant even for moderate values of the attenuation coefficients (see Chapter 6). Hence, future work should include evaluation of the magnitude of the inhomogeneity angle and of its influence on the estimation of the attenuation-anisotropy parameters.

Third, the data-processing sequence did not include compensation for a possible attenuation-related frequency dependence of the reflection/transmission coefficients along the ray-path. Moreover, choice of the frequency band can change the results of attenuation analysis.

Finally, since this work was restricted to P-waves, I was unable to evaluate the strength of the shear-wave attenuation anisotropy and estimate the full set of Thomsen-style anisotropy parameters. A more complete characterization of attenuation anisotropy requires combining compressional data with either shear or mode-converted waves.

4.7 Conclusions

Since case studies involving attenuation measurements are scarce, physical modeling can provide valuable insights into the behavior of attenuation coefficients and the performance of seismic algorithms for attenuation analysis. Here, I extended the spectral-ratio method to anisotropic materials and applied it to P-waves transmitted through a transversely isotropic sample for a wide range of propagation angles. After estimating the group (effective) attenuation along the raypath, I computed the corresponding phase (plane-wave) attenuation coefficient \mathcal{A} using the known TI velocity model. The difference between the phase and group attenuation, caused by the influence of velocity anisotropy, has to be accounted for in the inversion for the attenuation-anisotropy parameters.

The angle-varying coefficient \mathcal{A} was used to estimate the Thomsen-style attenuation parameters \mathcal{A}_{P0} , ϵ_Q , and δ_Q . The large absolute values of both $\epsilon_Q = -0.92$ and $\delta_Q = -1.84$ reflect the extremely high magnitude of the attenuation anisotropy, with the Q -factor increasing from 3.2 in the slow (symmetry-axis) direction to almost 40 in the fast (isotropy-plane) direction. These results corroborate the conclusions of some previous experimental studies that attenuation is often more sensitive to anisotropy than are phase velocity or reflection coefficient. Perhaps, attenuation-anisotropy parameters will become valuable seismic attributes in characterization of fractured reservoirs.

4.8 Acknowledgments

I would like to express my gratitude to Dr. Ilya Tsvankin (CWP) and Dr. Pawan Dewangan (National Institute of Oceanography, India) for their contribution to this work. I am also grateful to Dr. Kasper van Wijk of the Physical Acoustics Laboratory (PAL, <http://acoustics.mines.edu/>) for acquiring the data and to Dr. Mike Batzle, Dr. Manika Prasad, and Ivan Vasconcelos (all of CSM) for useful discussions. The support for this work was provided by the Consortium Project on Seismic Inverse Methods for Complex Structures at CWP.

Chapter 5

Effective attenuation anisotropy of layered media

5.1 Summary

One of the factors responsible for effective anisotropy of seismic attenuation is interbedding of thin attenuative layers with different properties. Here, I apply Backus averaging to obtain the complex stiffness matrix for an effective medium formed by an arbitrary number of anisotropic, attenuative constituents. Unless the intrinsic attenuation is uncommonly strong, the effective velocity function is controlled by the real-valued stiffnesses (i.e., is independent of attenuation) and can be determined from the known equations for purely elastic media. Analysis of effective attenuation is more complicated because the attenuation parameters are influenced by coupling between the real and imaginary parts of the stiffness matrix.

The main focus of this chapter is on effective VTI models that include layers of isotropic and VTI constituents. Assuming that the stiffness contrasts, as well as the intrinsic velocity and attenuation anisotropy, are weak, I develop explicit first-order (linear) and second-order (quadratic) approximations for the attenuation-anisotropy parameters ϵ_Q , δ_Q , and γ_Q . Whereas the first-order approximation for each parameter is given simply by the volume-weighted average of its interval values, the second-order terms reflect the coupling between various factors related to both heterogeneity and intrinsic anisotropy. Interestingly, the effective attenuation for P- and SV-waves is anisotropic even for a medium composed of isotropic layers with no attenuation contrast, provided there is a velocity variation among the constituent layers. Contrasts in the intrinsic attenuation, however, do not create attenuation anisotropy, unless they are accompanied by velocity contrasts.

Extensive numerical testing shows that the second-order approximation for ϵ_Q , δ_Q , and γ_Q is close to the exact solution for most plausible subsurface models. The accuracy of the first-order approximation depends on the magnitude of the quadratic terms, which is largely governed by the strength of the velocity (rather than attenuation) contrasts and velocity anisotropy. The effective attenuation parameters for multiconstituent VTI models generally exhibit more variation than do the velocity parameters, with almost equal probability of positive and negative values. If some of the constituents are azimuthally anisotropic with misaligned vertical symmetry planes, the effective velocity and attenuation functions can have different symmetries and principal azimuthal directions.

5.2 Introduction

In addition to fluid flow in fractured or porous media, or directionally-dependent stress applied to the media, interbedding of thin layers with different attenuation coefficients is another possible cause of attenuation anisotropy. Long-wavelength velocity anisotropy of layered media has been discussed extensively in the literature (e.g., Backus, 1962; Berryman, 1979; Schoenberg and Muir, 1989; Shapiro and Hubral, 1996; Bakulin, 2003; Bakulin and Grechka, 2003). Although attenuation anisotropy usually accompanies velocity anisotropy (e.g., Tao and King, 1990; Arts and Rasolofosaon, 1992), much less attention has been devoted to studies of effective anisotropy of layered attenuative media. Sams (1995) measured effective attenuation coefficients partially resulting from apparent (layer-induced) attenuation, but his work is restricted to isotropic models. Molotkov and Bakulin (1998) discussed a matrix-averaging technique for stratified lossy porous medium and obtained an effective Biot medium with anisotropic viscosity and relaxation. By employing the correspondence principle (e.g., Bland, 1960) for thin-layered viscoelastic media, Carcione (1992) derived the complex stiffnesses of effective media composed of attenuative, isotropic constituent layers. This effective stiffness matrix can be used to quantify both velocity anisotropy and attenuation anisotropy.

Here I analyze the effective properties of a sequence of attenuative anisotropic layers. The discussion is focused primarily on transversely isotropic (TI) constituents with a vertical symmetry axis for both velocity and attenuation. First, the Backus averaging technique is used to obtain the exact stiffness matrix in the low-frequency limit. Then I develop the first- and second-order approximations for the effective velocity and attenuation anisotropy in terms of the interval anisotropy parameters and stiffness contrasts. The second-order (quadratic) solution is particularly helpful in evaluating the contributions of various factors to the effective attenuation-anisotropy parameters. Numerical tests demonstrate that the performance of the approximations is mostly influenced by the velocity field (i.e., by the real parts of the stiffness coefficients). Simulations for a representative set of randomly layered TI models help to estimate the bounds on the effective velocity and attenuation parameters. Finally, I consider azimuthally anisotropic constituent layers and discuss the possibility of misaligned symmetry directions for the velocity and attenuation functions.

5.3 Effective parameters of layered anisotropic attenuative media

The Backus (1962) averaging technique was originally introduced to compute the effective properties of a stack of elastic (non-attenuative) isotropic layers in the long-wavelength limit. Here, I derive the effective stiffness coefficients for stratified models composed of thin attenuative anisotropic layers.

The constitutive relationship for attenuative media can be expressed in the time domain as

$$\boldsymbol{\tau} = \mathcal{L}\mathbf{e}, \quad (5.1)$$

where $\boldsymbol{\tau}$ and \mathbf{e} are the real-valued stress and strain tensors, respectively. \mathcal{L} is a first-order

linear differential operator that reduces to the real-valued stiffness tensor for elastic media. For example, consider a 1-D standard linear solid model (also called the Zener model) used to characterize dissipative rocks and polymers (e.g., Ferry, 1980; Carcione, 2001). This model includes a spring combined with a unit consisting of another spring and a dashpot connected in parallel; its viscoelastic behavior is described by

$$\tau + \tau_\tau \partial_t \tau = M_R(\epsilon + \tau_e \partial_t \epsilon), \quad (5.2)$$

where τ_τ and τ_e are the two relaxation times for the mechanical system, and M_R is the *relaxed* modulus. For elastic media, the relaxation times vanish, and M_R reduces to a real-valued modulus.

Transforming the constitutive relationship from equation 5.1 into the frequency domain yields

$$\tilde{\tau} = \tilde{C} \tilde{\epsilon}, \quad (5.3)$$

where all quantities become complex-valued (denoted by $\tilde{}$); \tilde{C} is the complex stiffness tensor.

Suppose a thin-layered model includes N types of constituents, whose spatial distribution is stationary across all the layers. For simplicity, throughout this chapter the layering plane is assumed to be horizontal. The medium properties are constant within each layer but change across layer boundaries (medium interfaces). Different layers belong to the same constituent if they have identical medium properties including both velocity and attenuation. For example, it is possible to form a model with hundreds of thin layers by using just two interbedding constituents.

The Backus averaging technique for both elastic and attenuative media is applied in the long-wavelength limit, which means that the dominant wavelength is much larger than the thickness of all layers. Following Backus (1962) and Schoenberg and Muir (1989), I assume that in the time domain the components of the traction vector that acts across interfaces are the same for all layers:

$$\tau_{13}^{(k)} \equiv \tau_{13}, \quad \tau_{23}^{(k)} \equiv \tau_{23}, \quad \tau_{33}^{(k)} \equiv \tau_{33}, \quad (5.4)$$

where the superscript denotes the k -th constituent. The in-plane strain components are also supposed to be the same:

$$e_{11}^{(k)} \equiv e_{11}, \quad e_{22}^{(k)} \equiv e_{22}, \quad e_{12}^{(k)} \equiv e_{12}. \quad (5.5)$$

Equations 5.4 and 5.5 remain valid for the frequency-domain counterparts of the stress and strain elements:

$$\tilde{\tau}_{13}^{(k)} \equiv \tilde{\tau}_{13}, \quad \tilde{\tau}_{23}^{(k)} \equiv \tilde{\tau}_{23}, \quad \tilde{\tau}_{33}^{(k)} \equiv \tilde{\tau}_{33}, \quad (5.6)$$

and

$$\tilde{e}_{11}^{(k)} \equiv \tilde{e}_{11}, \quad \tilde{e}_{22}^{(k)} \equiv \tilde{e}_{22}, \quad \tilde{e}_{12}^{(k)} \equiv \tilde{e}_{12}. \quad (5.7)$$

When the frequency goes to zero, the imaginary parts of the complex stiffness components vanish, and the medium becomes non-attenuative.

Since all stress and strain components in equations 5.6 and 5.7 are just the complex counterparts of the corresponding quantities in equations 5.4 and 5.5, the effective stiffnesses for layered attenuative media can be obtained using the results of Schoenberg and Muir (1989) for purely elastic models:

$$\tilde{\mathbf{C}}_{NN} = \langle \tilde{\mathbf{C}}_{NN}^{-1} \rangle^{-1}, \quad (5.8)$$

$$\tilde{\mathbf{C}}_{TN} = \langle \tilde{\mathbf{C}}_{TN} \tilde{\mathbf{C}}_{NN}^{-1} \rangle \tilde{\mathbf{C}}_{NN}, \quad (5.9)$$

$$\tilde{\mathbf{C}}_{TT} = \langle \tilde{\mathbf{C}}_{TT} \rangle - \langle \tilde{\mathbf{C}}_{TN} \tilde{\mathbf{C}}_{NN}^{-1} \tilde{\mathbf{C}}_{NT} \rangle + \langle \tilde{\mathbf{C}}_{TN} \tilde{\mathbf{C}}_{NN}^{-1} \rangle \tilde{\mathbf{C}}_{NN} \langle \tilde{\mathbf{C}}_{NN}^{-1} \tilde{\mathbf{C}}_{NT} \rangle, \quad (5.10)$$

where $\langle \cdot \rangle$ denotes the volume-weighted average. The submatrices for each constituent have the following form:

$$\tilde{\mathbf{C}}_{NN}^{(k)} = \begin{bmatrix} \tilde{c}_{33} & \tilde{c}_{34} & \tilde{c}_{35} \\ \tilde{c}_{34} & \tilde{c}_{44} & \tilde{c}_{45} \\ \tilde{c}_{35} & \tilde{c}_{45} & \tilde{c}_{55} \end{bmatrix}, \quad (5.11)$$

$$\tilde{\mathbf{C}}_{TN}^{(k)} = \tilde{\mathbf{C}}_{NT}^{(k)T} = \begin{bmatrix} \tilde{c}_{13} & \tilde{c}_{14} & \tilde{c}_{15} \\ \tilde{c}_{23} & \tilde{c}_{24} & \tilde{c}_{25} \\ \tilde{c}_{36} & \tilde{c}_{46} & \tilde{c}_{56} \end{bmatrix}, \quad (5.12)$$

and

$$\tilde{\mathbf{C}}_{TT}^{(k)} = \begin{bmatrix} \tilde{c}_{11} & \tilde{c}_{12} & \tilde{c}_{16} \\ \tilde{c}_{12} & \tilde{c}_{22} & \tilde{c}_{26} \\ \tilde{c}_{16} & \tilde{c}_{26} & \tilde{c}_{66} \end{bmatrix}. \quad (5.13)$$

Equations 5.8-5.13 describe the effective properties for any number of constituents with arbitrary anisotropy in terms of both velocity and attenuation.

5.3.1 Effective stiffnesses for TI media

Transversely isotropic (TI) layers (primarily shales and shaly sands) are common for sedimentary basins (Sayers, 1994; Tsvankin, 2005). Here, I consider a layered medium composed of TI constituents with a vertical symmetry axis (VTI) for both velocity and attenuation. Substituting the complex stiffness matrix \tilde{c}_{ij} of the VTI constituent layers into equations 5.8-5.13 yields an effective attenuative VTI model with five independent complex stiffnesses:

$$\tilde{c}_{11} = \langle \tilde{c}_{11} \rangle - \langle (\tilde{c}_{13})^2 / \tilde{c}_{33} \rangle + \langle 1 / \tilde{c}_{33} \rangle^{-1} \langle \tilde{c}_{13} / \tilde{c}_{33} \rangle^2, \quad (5.14)$$

$$\tilde{c}_{33} = \langle 1 / \tilde{c}_{33} \rangle^{-1}, \quad (5.15)$$

$$\tilde{c}_{13} = \langle 1 / \tilde{c}_{33} \rangle^{-1} \langle \tilde{c}_{13} / \tilde{c}_{33} \rangle, \quad (5.16)$$

$$\tilde{c}_{55} = \langle 1 / \tilde{c}_{55} \rangle^{-1}, \quad (5.17)$$

$$\tilde{c}_{66} = \langle 1 / \tilde{c}_{66} \rangle^{-1}; \quad (5.18)$$

$\tilde{c}_{12} = \tilde{c}_{11} - 2\tilde{c}_{66}$. The effective velocity-anisotropy parameters in Thomsen's (1986) notation are obtained using the real parts c_{ij} of the effective stiffnesses from equations 5.14-5.18:

$$V_{P0} \equiv \sqrt{\frac{c_{33}}{\rho}}, \quad V_{S0} \equiv \sqrt{\frac{c_{55}}{\rho}}, \quad (5.19)$$

$$\epsilon \equiv \frac{c_{11} - c_{33}}{2c_{33}}, \quad (5.20)$$

$$\delta \equiv \frac{(c_{13} + c_{55})^2 - (c_{33} - c_{55})^2}{2c_{33}(c_{33} - c_{55})}, \quad (5.21)$$

$$\gamma \equiv \frac{c_{66} - c_{55}}{2c_{55}}, \quad (5.22)$$

where $\rho = \langle \rho \rangle$ is the volume-averaged density.

To characterize attenuative anisotropy, I employ the effective attenuation-anisotropy parameters defined in equations 2.28, 2.31, and 2.24:

$$\epsilon_Q \equiv \frac{Q_{33} - Q_{11}}{Q_{11}}, \quad (5.23)$$

$$\delta_Q \equiv \frac{\frac{Q_{33} - Q_{55}}{Q_{55}} c_{55} \frac{(c_{13} + c_{33})^2}{(c_{33} - c_{55})} + 2 \frac{Q_{33} - Q_{13}}{Q_{13}} c_{13} (c_{13} + c_{55})}{c_{33} (c_{33} - c_{55})}, \quad (5.24)$$

$$\gamma_Q \equiv \frac{Q_{55} - Q_{66}}{Q_{66}}, \quad (5.25)$$

where $Q_{ij} = c_{ij}/c_{ij}^I$ is the quality-factor matrix (no index summation is applied), and c_{ij}^I is the imaginary part of the stiffness \tilde{c}_{ij} . The notation of Zhu and Tsvankin (2006) also includes two reference parameters — the wavenumber-normalized attenuation coefficients for P- and S-waves in the symmetry (vertical) direction (see equations 2.22 and 2.23, respectively):

$$A_{P0} = Q_{33} \left(\sqrt{1 + 1/(Q_{33})^2} - 1 \right) \approx \frac{1}{2Q_{33}}, \quad (5.26)$$

$$A_{S0} = Q_{55} \left(\sqrt{1 + 1/(Q_{55})^2} - 1 \right) \approx \frac{1}{2Q_{55}}. \quad (5.27)$$

Note that equations 5.23–5.27 are defined through effective stiffness and Q components. The approximations in equations 5.26 and 5.27 are obtained in the weak-attenuation limit by keeping only the linear terms in the inverse components Q_{ii} ($i = 3, 5$).

5.4 Approximate attenuation parameters of effective VTI media

Explicit equations for the effective stiffnesses in terms of the interval parameters have a rather complicated form. Here, I present approximate expressions that help to evaluate the influence of different factors on the anisotropy of the effective medium. The approximations are developed under the assumption of weak intrinsic velocity and attenuation anisotropy,

as well as small contrasts in the stiffnesses between different constituents.

Unless the medium is strongly attenuative and has non-negligible dispersion, the influence of the quality-factor elements on phase velocity is of the second order and typically can be ignored (Červený and Pšenčík, 2005; Zhu and Tsvankin, 2006). Hence, the effective velocity-anisotropy parameters remain practically the same as those for the purely elastic model defined by the real parts of the stiffness elements. Since a detailed description of the velocity anisotropy of fine-layered VTI media can be found in Bakulin (2003), the discussion below is focused primarily on the attenuation-anisotropy parameters.

5.4.1 First-order approximation

Approximate effective parameters can be derived by expanding the exact equations in the small quantities (velocity- and attenuation-anisotropy parameters and the contrasts in the stiffnesses) and neglecting higher-order terms. To first-order (linear) approximation, the effective value of any anisotropy parameter is equal simply to its volume-weighted average (Bakulin and Grechka, 2003). For example, the linearized parameter ϵ can be written as

$$\epsilon = \langle \epsilon \rangle = \sum_{k=1}^N \phi^{(k)} \epsilon^{(k)}, \quad (5.28)$$

where $\phi^{(k)}$ is the volume fraction of each constituent. Similarly, the attenuation-anisotropy parameter ϵ_Q can be approximated as

$$\epsilon_Q = \langle \epsilon_Q \rangle = \sum_{k=1}^N \phi^{(k)} \epsilon_Q^{(k)}. \quad (5.29)$$

Clearly, the effective medium properties in the long-wavelength limit are independent of the spatial sequence of the constituents, which can be arranged in an arbitrary order.

5.4.2 Second-order approximation

The second-order approximation for the effective velocity-anisotropy parameters of two-constituent VTI media is given by Bakulin (2003). Here, I present a more general analysis that accounts for attenuation and allows for an arbitrary number of VTI constituents.

The parameters assumed to be small for each constituent k include $\hat{\Delta}c_{33}^{(k)}$, $\hat{\Delta}c_{55}^{(k)}$, $\hat{\Delta}Q_{33}^{(k)}$, $\hat{\Delta}Q_{55}^{(k)}$, $\epsilon^{(k)}$, $\delta^{(k)}$, $\gamma^{(k)}$, $\epsilon_Q^{(k)}$, $\delta_Q^{(k)}$, and $\gamma_Q^{(k)}$, where $\hat{\Delta}c_{ii}^{(k)}$ and $\hat{\Delta}Q_{ii}^{(k)}$ quantify the magnitude of property variations in the model:

$$\hat{\Delta}c_{ii}^{(k)} = \Delta c_{ii}^{(k)} / \bar{c}_{ii}, \quad (5.30)$$

$$\hat{\Delta}Q_{ii}^{(k)} = \Delta Q_{ii}^{(k)} / \bar{Q}_{ii}, \quad ii = 33 \text{ or } 55. \quad (5.31)$$

Here, $\bar{c}_{ii} = \frac{1}{N} \sum_{k=1}^N c_{ii}^{(k)}$ and $\bar{Q}_{ii} = \frac{1}{N} \sum_{k=1}^N Q_{ii}^{(k)}$ are the arithmetic averages of c_{ii} and Q_{ii}

among all N constituents, while $\Delta c_{ii}^{(k)} = c_{ii}^{(k)} - \bar{c}_{ii}$ and $\Delta Q_{ii}^{(k)} = Q_{ii}^{(k)} - \bar{Q}_{ii}$ denote the deviations from the average values. In the approximations discussed here, the squared vertical-velocity ratio $g = \frac{\bar{c}_{55}}{\bar{c}_{33}}$ and the vertical attenuation ratio $g_Q = \frac{\bar{Q}_{33}}{\bar{Q}_{55}}$ are not treated as small parameters. It is assumed, however, that the attenuation is not uncommonly strong so that quadratic and higher-order terms in $1/Q_{ii}$ can be neglected.

The approximate effective parameters for both velocity and attenuation anisotropy are given in Appendix F. For the special case of two constituents ($N=2$), the velocity-anisotropy parameters become identical to those given by Bakulin (2003). In principle, the exact effective velocity-anisotropy parameters depend on all possible factors including the quality-factor matrix that describes the intrinsic attenuation. However, unless the model has extremely high attenuation with some of the quality-factor components smaller than 10, the contribution of the attenuation parameters to the effective velocity anisotropy can be ignored.

In contrast, the effective attenuation anisotropy is influenced not just by the imaginary part of the stiffness matrix (i.e., by the intrinsic attenuation and the contrasts in the attenuation parameters), but also by the real parts of the stiffnesses (i.e., by the velocity parameters) and the coupling between various factors. The second-order approximations for the effective Thomsen-style attenuation parameters can be represented as (equations F.37, F.43, and F.15):

$$\epsilon_Q = \langle \epsilon_Q \rangle + \epsilon_Q^{(\text{is})} + \epsilon_Q^{(\text{is-Van})} + \epsilon_Q^{(\text{is-Qan})} + \epsilon_Q^{(\text{Van-Qan})}, \quad (5.32)$$

$$\delta_Q = \langle \delta_Q \rangle + \delta_Q^{(\text{is})} + \delta_Q^{(\text{is-Qan})} + \delta_Q^{(\text{Van-Qan})} + \delta_Q^{(\text{Van})}, \quad (5.33)$$

$$\gamma_Q = \langle \gamma_Q \rangle + \gamma_Q^{(\text{is})} + \gamma_Q^{(\text{is-Van})} + \gamma_Q^{(\text{is-Qan})} + \gamma_Q^{(\text{Van-Qan})}, \quad (5.34)$$

where $\langle \cdot \rangle$ is the first-order term equal to the volume-weighted average of the intrinsic parameter values, and the rest of the terms are quadratic (second-order) in the small parameters listed above. The superscript (is) refers to the contribution of the parameters $\Delta c_{ii}^{(k)}$ and $\Delta Q_{ii}^{(k)}$ ($i = 3, 5$), which quantify the heterogeneity (contrasts) of the *isotropic* quantities, while (Van) depends on the intrinsic velocity anisotropy. The superscripts (is-Van) , (is-Qan) , and (Van-Qan) denote the quadratic terms that represent (respectively) the coupling between the isotropic heterogeneity and intrinsic velocity anisotropy, between the isotropic heterogeneity and intrinsic attenuation anisotropy, and between the intrinsic velocity and attenuation anisotropy.

Note that there are no “Van”-terms (i.e., terms quadratic in the interval velocity-anisotropy parameters) in equation 5.32 for ϵ_Q and equation 5.34 for γ_Q . The parameter δ_Q in equation 5.33 does include the term $\delta_Q^{(\text{Van})}$ but not $\delta_Q^{(\text{is-Van})}$, which is similar to the

structure of equation F.32 for the velocity-anisotropy parameter δ . It is interesting that while the second-order approximations for ϵ_Q , δ_Q , and γ_Q depend on the coupling between the intrinsic attenuation anisotropy and other factors (the intrinsic velocity anisotropy and the isotropic heterogeneity), none of them contains the sole contribution of the intrinsic attenuation-anisotropy parameters (i.e., there are no terms with the superscript ‘‘Qan’’). The leading (first-order) term, however, is entirely controlled by the corresponding average attenuation-anisotropy parameter.

Explicit expressions for all second-order terms are listed in Appendix A. Equations F.43–F.48 show that the parameter δ_Q is independent of the intrinsic-anisotropy parameters $\epsilon^{(k)}$ and $\epsilon_Q^{(k)}$; this result follows directly from the exact equation 5.24. In contrast, ϵ_Q is influenced by all anisotropy parameters for P-SV waves ($\epsilon^{(k)}$, $\delta^{(k)}$, $\epsilon_Q^{(k)}$, and $\delta_Q^{(k)}$) because these parameters contribute to the effective values of c_{11} and Q_{11} (equation F.21).

According to equations F.39, F.45, and F.17, the isotropic-heterogeneity terms $\epsilon_Q^{(\text{is})}$, $\delta_Q^{(\text{is})}$ and $\gamma_Q^{(\text{is})}$ vanish when both $c_{55}^{(k)}$ and $Q_{55}^{(k)}$ are constant for all constituents. This is a generalization of the known result for the effective velocity anisotropy of elastic media (Postma, 1955; Bakulin, 2003): the heterogeneity terms $\epsilon^{(\text{is})} = \delta^{(\text{is})} = \gamma^{(\text{is})} = 0$ if $c_{55}^{(k)} = \text{const}$, $k = 1 \cdots N$.

As also pointed out by Bakulin (2003), $\delta^{(\text{is})}$ in equation F.34 vanishes if the vertical velocity ratio $V_{P0}^{(k)}/V_{S0}^{(k)}$ is constant for all constituents (i.e., $c_{55}^{(k)}/c_{33}^{(k)} = \text{const}$, $k = 1 \cdots N$), which means $\hat{\Delta}c_{55}/\bar{c}_{55} = \hat{\Delta}c_{33}/\bar{c}_{33}$. The parameter $\delta_Q^{(\text{is})}$ in equation F.45, however, does not preserve such a property: Even if $\hat{\Delta}c_{55}/\bar{c}_{55} = \hat{\Delta}c_{33}/\bar{c}_{33}$ and $\hat{\Delta}Q_{55}/\bar{Q}_{55} = \hat{\Delta}Q_{33}/\bar{Q}_{33}$, $\delta_Q^{(\text{is})}$ is not zero unless $\bar{g}_Q = 1$, which means identical quality factors for all constituents ($Q_{33}^{(k)} = Q_{55}^{(k)}$, $k = 1 \cdots N$).

5.4.3 Velocity contrast versus attenuation contrast

As extensively discussed in the literature, velocity contrasts between thin layers cause effective velocity anisotropy in the long-wavelength limit (e.g., Backus, 1962; Brittan et al., 1995; Werner and Shapiro, 1999; Bakulin and Grechka, 2003). The nature of the contribution of the velocity contrasts to the effective attenuation anisotropy, however, is much less obvious. In this section, I compare the influence of the velocity and attenuation contrasts on the effective attenuation-anisotropy parameters.

The second-order approximations help to separate the contributions of the velocity parameters from those of the attenuation contrasts and intrinsic attenuation anisotropy. Indeed, the attenuation-anisotropy parameters ϵ_Q and δ_Q (equations F.37–F.42 and F.43–F.48) contain several terms controlled entirely by the contrasts in the real-valued stiffnesses c_{33} and c_{55} and by the intrinsic velocity anisotropy. For example, the approximate ϵ_Q depends on $\frac{\Delta c_{33}^{(k,l)}}{\bar{c}_{33}} \frac{\Delta c_{55}^{(k,l)}}{\bar{c}_{55}}$ and $\left(\frac{\Delta c_{55}^{(k,l)}}{\bar{c}_{55}}\right)^2$ (see equation F.39; k and l denote different

constituents), as well as on $\frac{\Delta c_{55}^{(k,l)}}{\bar{c}_{55}} \Delta \delta^{(k,l)}$ (equation F.40). This means that the velocity parameters can create effective attenuation anisotropy for P- and SV-waves even without any attenuation contrasts or intrinsic attenuation anisotropy. Still, for the attenuation-anisotropy parameters to have finite values, the constituents need to be attenuative. If the medium is purely elastic and all intrinsic Q_{ij} components are infinite, the parameters ϵ_Q , δ_Q , and γ_Q become undefined (equations 5.23–5.25).

To explore this issue further, let me consider the analytical expressions for the effective quality-factor components for a medium composed of constituents with the isotropic normalized attenuation coefficient \mathcal{A} , in which $\epsilon_Q^{(k)} = \delta_Q^{(k)} = \gamma_Q^{(k)} = 0$ for all k . The quality-factor matrix for each constituent is described by two independent components (Carcione, 2001; Zhu and Tsvankin, 2006), which is assume to be constant for the whole model: $Q_{11}^{(k)} = Q_{33}^{(k)} \equiv Q_P$ and $Q_{55}^{(k)} = Q_{66}^{(k)} \equiv Q_S$, where Q_P and Q_S are the quality factors for P- and S-waves, respectively. Then, as discussed by Zhu and Tsvankin (2006), the normalized attenuation coefficients in all layers will be identical and isotropic (independent of angle). Note that if the real-valued stiffnesses vary among the constituents, the quality-factor component $Q_{13}^{(k)}$ (unlike Q_P and Q_S) will not necessarily be constant. According to the definition of δ_Q (equation 5.24), $Q_{13}^{(k)}$ is given by

$$Q_{13}^{(k)} = Q_P \left/ \left[1 - \frac{(g_Q - 1)c_{55}^{(k)}(c_{13}^{(k)} + c_{33}^{(k)})^2}{2c_{13}^{(k)}(c_{13}^{(k)} + c_{55}^{(k)})(c_{33}^{(k)} - c_{55}^{(k)})} \right] \right., \quad (5.35)$$

where $g_Q \equiv Q_P/Q_S$.

The effective Q_{ij} components for this model can be obtained from equations F.21–F.23, F.2, and F.5:

$$Q_{11} = Q_P \mathcal{F} \left(c_{11}^{(k)}, c_{33}^{(k)}, \xi^{(k)}, \xi_Q^{(k)} \right), \quad (5.36)$$

$$Q_{33} = Q_P, \quad (5.37)$$

$$Q_{55} = Q_{66} = Q_S, \quad (5.38)$$

and

$$Q_{13} = Q_P \frac{\sum_{k=1}^N \phi^{(k)} \xi^{(k)}}{N \sum_{k=1}^N \phi^{(k)} \xi^{(k)} \xi_Q^{(k)}}, \quad (5.39)$$

where $\xi^{(k)} \equiv c_{13}^{(k)}/c_{33}^{(k)}$ and $\xi_Q^{(k)} \equiv Q_P/Q_{13}^{(k)}$. Since the expression for Q_{11} is rather lengthy, I

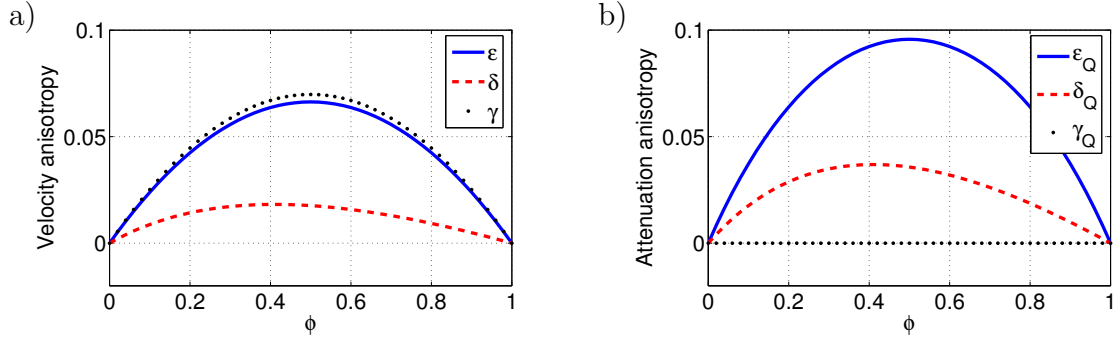


Figure 5.1. Exact effective anisotropy parameters computed from equations 5.20-5.25 for a layered model composed of two constituents with identical isotropic attenuation ($Q_{33}^{(1)} = Q_{33}^{(2)} = 100$; $Q_{55}^{(1)} = Q_{55}^{(2)} = 50$) and different isotropic velocity functions. The velocity contrasts are defined by $\Delta c_{33}/\bar{c}_{33} = 90\%$ and $\Delta c_{55}/\bar{c}_{55} = 70\%$; for the first constituent, $V_{P0}^{(1)} = 3.2$ km/s, $V_{S0}^{(1)} = 1.55$ km/s, and $\rho^{(1)} = 2.45$ g/cm³. The horizontal axis represents the volume fraction of the first constituent ($\phi = \phi_1$).

omit the explicit form of the function \mathcal{F} .

Although the attenuation of all constituents is identical and isotropic, the dependence of Q_{11} and Q_{13} on the real-valued stiffnesses makes the effective attenuation for P- and SV-waves angle-dependent (i.e., $\epsilon_Q \neq 0$ and $\delta_Q \neq 0$). The normalized attenuation coefficient of SH-waves, however, is isotropic because the effective parameter γ_Q goes to zero.

For the special case of equal quality factors for P- and S-waves ($Q_P = Q_S$ and $g_Q = 1$), the element Q_{13} is constant for all constituents ($Q_{13}^{(k)} = Q_P$), and $\xi_Q^{(k)} \equiv 1$. Then $\epsilon_Q = 0$ and $\delta_Q = 0$ because all effective quality-factor components are identical ($Q_{11} = Q_{33} = Q_{13} = Q_{55} = Q_{66}$). This means that for $Q_P = Q_S$ the effective attenuation is isotropic no matter how significant are the velocity contrasts and intrinsic velocity anisotropy.

The magnitude of the velocity-induced attenuation anisotropy for a two-constituent model is illustrated in Figure 5.1. Both constituents have isotropic velocity functions and the same isotropic attenuation (with $Q_{33} \neq Q_{55}$). The substantial contrasts in the P- and S-wave velocities, however, create non-negligible velocity and attenuation anisotropy for P- and SV-waves. In particular, the parameter ϵ_Q reaches values close to 0.1 when the volume fractions of the constituents are equal to each other.

Next, I analyze the influence of the attenuation contrasts on the effective attenuation anisotropy by assuming that the velocity field is homogeneous and all five velocity parameters are constant: $\hat{\Delta}c_{33}^{(k)} = \hat{\Delta}c_{55}^{(k)} = 0$ and $\Delta\epsilon^{(k)} = \Delta\delta^{(k)} = \Delta\gamma^{(k)} = 0$ for all constituents k .

The effective quality-factor components then have the same form:

$$Q_{ij} = \frac{1}{\sum_{k=1}^N \phi^{(k)} / Q_{ij}^{(k)}}, \quad (5.40)$$

where $ij = 11, 33, 13, 55$, or 66 . When the intrinsic attenuation is isotropic (i.e., $\epsilon_Q^{(k)} = \delta_Q^{(k)} = \gamma_Q^{(k)} = 0$), the only quantities that vary among the constituents are $Q_{33}^{(k)}$ and $Q_{55}^{(k)}$. Since for isotropic intrinsic attenuation $Q_{11}^{(k)} = Q_{33}^{(k)}$ and $Q_{55}^{(k)} = Q_{66}^{(k)}$, the effective parameters ϵ_Q and $\gamma_Q = 0$ vanish. Also, the element $Q_{13}^{(k)}$ becomes

$$Q_{13}^{(k)} = \frac{Q_{33}^{(k)}}{1 - \frac{c_{55}(c_{13} + c_{33})^2}{2c_{13}(c_{13} + c_{55})(c_{33} - c_{55})} \left(\frac{Q_{33}^{(k)}}{Q_{55}^{(k)}} - 1 \right)}, \quad (5.41)$$

where $c_{ij}^{(k)} = c_{ij}$ because the velocity field is homogeneous. The effective Q_{13} component is then given by

$$Q_{13} = \frac{Q_{33}}{1 - \frac{c_{55}(c_{13} + c_{33})^2}{2c_{13}(c_{13} + c_{55})(c_{33} - c_{55})} \left(\frac{Q_{33}}{Q_{55}} - 1 \right)}. \quad (5.42)$$

Substituting equations 5.40 and 5.42 into equation 5.24 yields $\delta_Q = 0$. Hence, if the velocity field is homogeneous, the contrasts in isotropic attenuation do not produce effective attenuation anisotropy.

This conclusion is supported by the 2D finite-difference simulation of SH-wave propagation in Figure 5.2. The model is made up of two VTI constituents with the thicknesses less than $1/20$ of the predominant wavelength, so the medium can be characterized as effectively homogeneous. Both constituents have isotropic attenuation and the same VTI velocity parameters, but there is a large contrast in the SH-wave quality-factor component Q_{55} . A snapshot of the SH-wavefront from a point source located at the center of the model is shown in Figure 5.2a. As pointed out by Tsvankin (2005), for 2D elastic TI models the amplitude along the SH-wavefront is constant (see the dashed circle in Figure 5.2b). Therefore, if the effective attenuation is directionally dependent, it should cause a deviation of the picked amplitude from a circle. However, despite some distortions produced by the automatic picking procedure, the amplitude variation along the wavefront in the attenuative model is almost negligible (Figure 5.2b). Clearly, the attenuation contrast does not result in effective attenuation anisotropy if it is not accompanied by a velocity contrast.

5.5 Accuracy of the approximations

To test the accuracy of the approximations introduced above, I first use a model formed by two VTI constituent layers. The velocity parameters listed in Table 5.1 are taken from

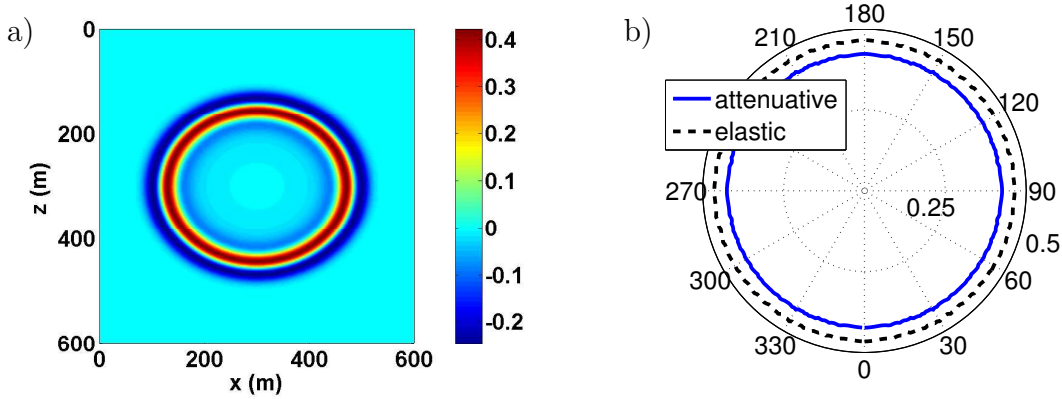


Figure 5.2. a) Snapshot of the SH-wavefront computed by 2D finite differences for a layered attenuative medium (the time $t=0.3$ s). The model includes two constituents with the same VTI velocity parameters and density: $V_S = 1500$ m/s, $\gamma = 0.2$, and $\rho = 2400$ kg/m³. The intrinsic attenuation is isotropic; for the first constituent, $Q_{55} = Q_{66} = 20$ and the volume percentage $\phi = 33.3\%$; for the second constituent, $Q_{55} = Q_{66} = 50$. b) Polar plot of the picked amplitude along the wavefront (solid curve) and the corresponding amplitude for the elastic model with $Q_{55} = Q_{66} = \infty$ (dashed curve).

Bakulin (2003). The maximum magnitude of the velocity-anisotropy parameters is 0.25, while the contrast in c_{33} and c_{55} reaches 30%. Since the strength of attenuation anisotropy often exceeds that of velocity anisotropy, I take each attenuation-anisotropy parameter to be twice as large by absolute value as the corresponding velocity parameter (e.g., $|\epsilon_Q| = |2\epsilon|$). Also, in accordance with the experimental results of Zhu et al. (2006), all attenuation-anisotropy parameters are negative. The contrast in the quality-factor elements Q_{33} and Q_{55} (60%) is also twice that in c_{33} and c_{55} , which means that the value of Q_{33} for the second constituent is nearly doubled compared to that for the first constituent, while Q_{55} is almost halved.

The numerical results in Figure 5.3 demonstrate that the linear (first-order) approximation (dashed lines) generally follows the trend of the exact effective parameters (solid lines). The maximum error for the velocity-anisotropy parameters, which occurs when the constituents occupy nearly equal volumes ($\phi = \phi^{(1)} \approx 0.5$), does not exceed 0.03. The accuracy of the linear approximation is much smaller for the attenuation-anisotropy parameters, especially for δ_Q . The error in δ_Q reaches 0.3, and the linear solution even predicts the wrong sign of this parameter for a wide range of the volume ratios ($0.3 < \phi < 1$).

Despite the substantial velocity and attenuation contrast between the two constituents, the second-order approximations in Figure 5.3 (dotted lines) are sufficiently close to the exact values. The maximum error does not exceed 0.005 for the velocity-anisotropy parameters and 0.04 for the attenuation-anisotropy parameters.

$\frac{\Delta c_{33}}{\bar{c}_{33}}$	$\frac{\Delta c_{55}}{\bar{c}_{55}}$	$\epsilon(1)$	$\epsilon(2)$	$\delta(1)$	$\delta(2)$	$\gamma(1)$	$\gamma(2)$
30%	-30%	0.05	0.25	0	0.2	0.05	0.25
$\frac{\Delta Q_{33}}{\bar{Q}_{33}}$	$\frac{\Delta Q_{55}}{\bar{Q}_{55}}$	$\epsilon_Q(1)$	$\epsilon_Q(2)$	$\delta_Q(1)$	$\delta_Q(2)$	$\gamma_Q(1)$	$\gamma_Q(2)$
60%	-60%	-0.1	-0.5	0	-0.4	-0.1	-0.5

Table 5.1. Parameters of a two-constituent attenuative VTI model. For the first constituent, $V_{P0} = 3$ km/s, $V_{S0} = 1.5$ km/s, $\rho = 2.4$ g/cm³, $Q_{33} = 100$, and $Q_{55} = 80$.

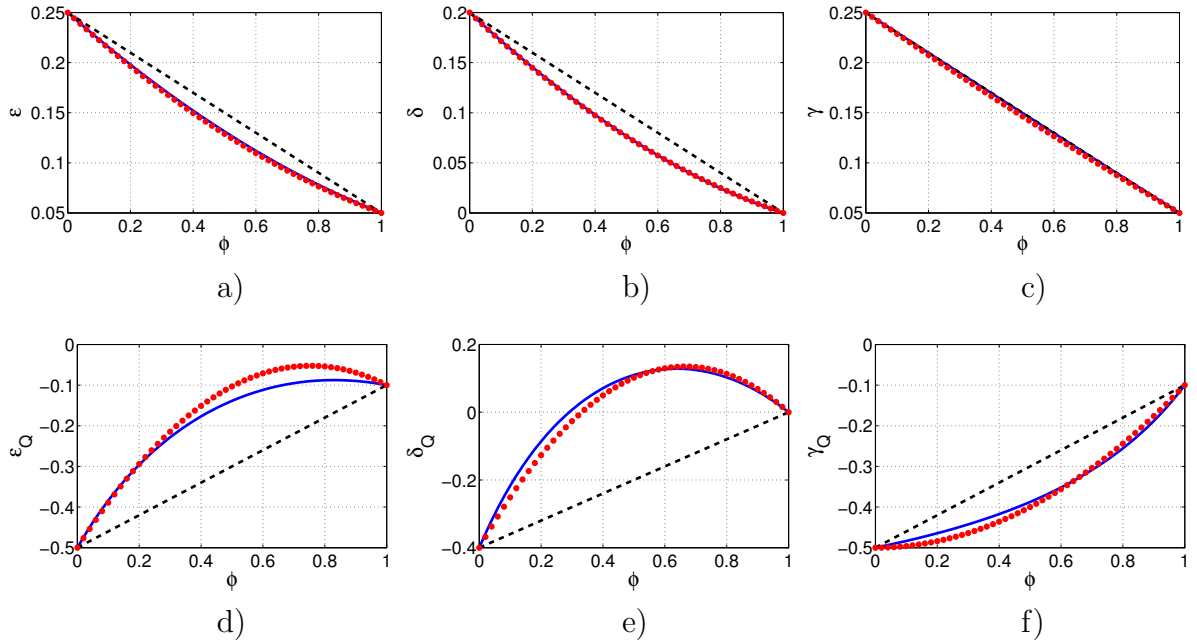


Figure 5.3. Effective velocity-anisotropy (a-c) and attenuation-anisotropy (d-f) parameters for the two-constituent VTI model from Table 5.1. The horizontal axis represents the volume fraction of the first constituent ($\phi = \phi_1$). The exact parameters (solid lines) are plotted along with the first-order linear approximations (dashed) and the second-order approximations (dotted).

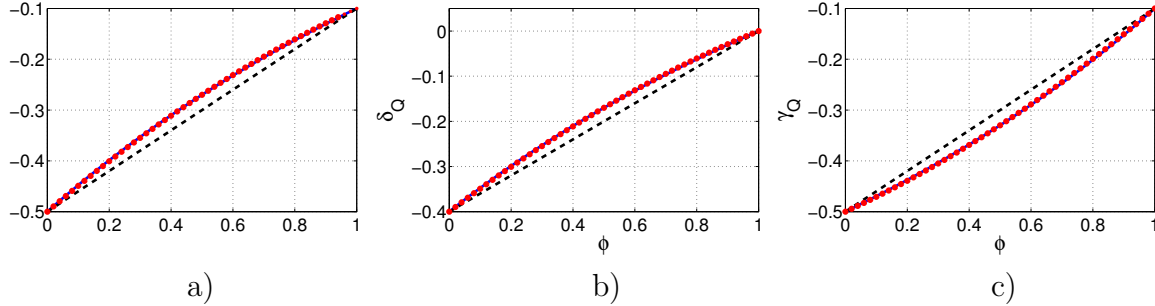


Figure 5.4. Effective attenuation anisotropy for a model with the same attenuation parameters as those in Figure 5.3, but both constituents have identical isotropic velocity functions ($\epsilon^{(1)} = \epsilon^{(2)} = \delta^{(1)} = \delta^{(2)} = \gamma^{(1)} = \gamma^{(2)} = \Delta c_{33}/\bar{c}_{33} = \Delta c_{55}/\bar{c}_{55} = 0$). Compare with Figures 5.3d,e,f.

Next, to analyze the relative contribution of the attenuation parameters to the effective attenuation anisotropy, I change the model by making the velocity functions of both constituents isotropic and eliminating the velocity contrast between them. In agreement with the theoretical analysis in the previous section, the second-order terms for such a model become much smaller, which substantially increases the accuracy of the linear approximation (Figure 5.4). The only remaining second-order terms for this model are related to the coupling between the attenuation contrasts and intrinsic attenuation anisotropy.

The second-order solution for all parameters in Figure 5.4 virtually coincides with the exact result, which indicates that the accuracy of this approximation is mostly governed by the velocity contrasts and intrinsic velocity anisotropy. This is further confirmed by the test in Figure 5.5, which shows that the error of the second-order approximation remains practically negligible even for large absolute values of the attenuation-anisotropy parameters, as long as the velocity field is homogeneous and isotropic.

While the second-order approximation is adequate for a wide range of typical subsurface models, it deteriorates for uncommonly large velocity and attenuation contrasts (Figure 5.6). The error is particularly significant for the parameter ϵ_Q because the second-order solution produces distorted values of the quality-factor element Q_{11} .

To test the performance of the approximations for a more complicated, multi-constituent medium, I generate multiple realizations of a layered VTI model with intrinsic VTI attenuation (Figure 5.7). The vertical velocities (V_{P0} and V_{S0}) are computed using the $1/f^\alpha$ distribution with $\alpha = 0.3$. The vertical Q components Q_{33} varies between 70 and 125, while Q_{55} varies between 40 and 90. The density and interval anisotropy parameters follow normal random distributions with the following mean values: $\bar{\rho} = 2.49 \text{ g/cm}^3$, $\bar{\epsilon} = 0.2$, $\bar{\delta} = 0.08$, $\bar{\gamma} = 0.15$, $\bar{\epsilon}_Q = -0.4$, $\bar{\delta}_Q = -0.16$ and $\bar{\gamma}_Q = -0.3$. The standard deviations are $\text{std}(\rho) = 20 \text{ kg/m}^3$, $\text{std}(\epsilon) = \text{std}(\delta) = \text{std}(\gamma) = 0.09$, and $\text{std}(\epsilon_Q) = \text{std}(\delta_Q) = \text{std}(\gamma_Q) = 0.2$.

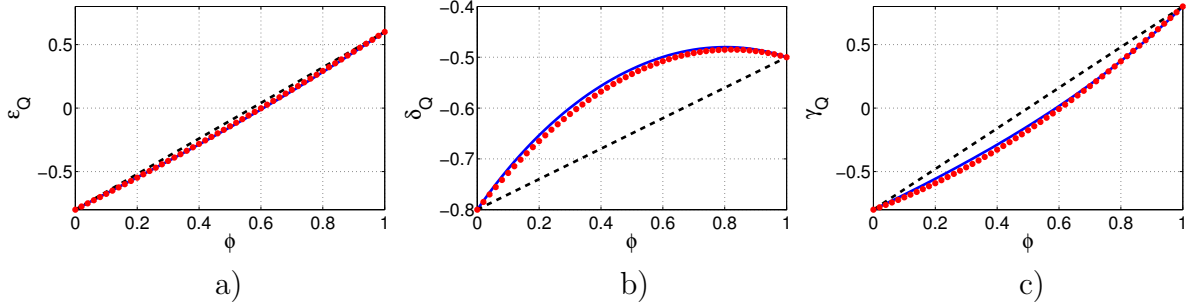


Figure 5.5. Effective attenuation anisotropy for a model with the same velocity parameters and contrasts in Q_{33} and Q_{55} as those in Figure 5.3, but the intrinsic attenuation anisotropy is more pronounced: $\epsilon_Q^{(1)} = 0.6$, $\epsilon_Q^{(2)} = -0.8$, $\delta_Q^{(1)} = -0.5$, $\delta_Q^{(2)} = -0.8$, $\gamma_Q^{(1)} = 0.8$, and $\gamma_Q^{(2)} = -0.8$. As before, the exact parameters (solid lines) are plotted along with the first-order linear approximations (dashed) and the second-order approximations (dotted).

This model is similar to the one used by Bakulin and Grechka (2003), who show that the first-order (linear) approximation is surprisingly accurate for the effective velocity-anisotropy parameters of typical layered media with moderate intrinsic anisotropy. In other words, the effective velocity anisotropy is primarily determined by the mean values of the interval parameters ϵ , δ , and γ .

The test in Figure 5.8 demonstrates that this result also applies to effective attenuation anisotropy. After computing the exact effective parameters for 2000 realizations of the model, I can compare their ranges (bars) with the mean values (crosses) listed above. Although some of the mean values are biased, they give a generally good prediction of the effective parameters. Therefore, despite the substantial property contrasts in the model realizations, the magnitude of the second-order terms in such multiconstituent models with random parameter distributions is relatively small, and all velocity- and attenuation-anisotropy parameters are close to the mean of the corresponding interval values.

5.5.1 Magnitude of attenuation anisotropy

For purposes of seismic processing and inversion, it is important to evaluate the upper and lower bounds of the parameters ϵ_Q , δ_Q , and γ_Q . Let me start with the SH-wave parameter γ_Q , which has a relatively simple analytic representation.

If a model is composed of isotropic constituents (in terms of both velocity and attenuation), the effective attenuation anisotropy is caused just by the heterogeneity. The SH-wave

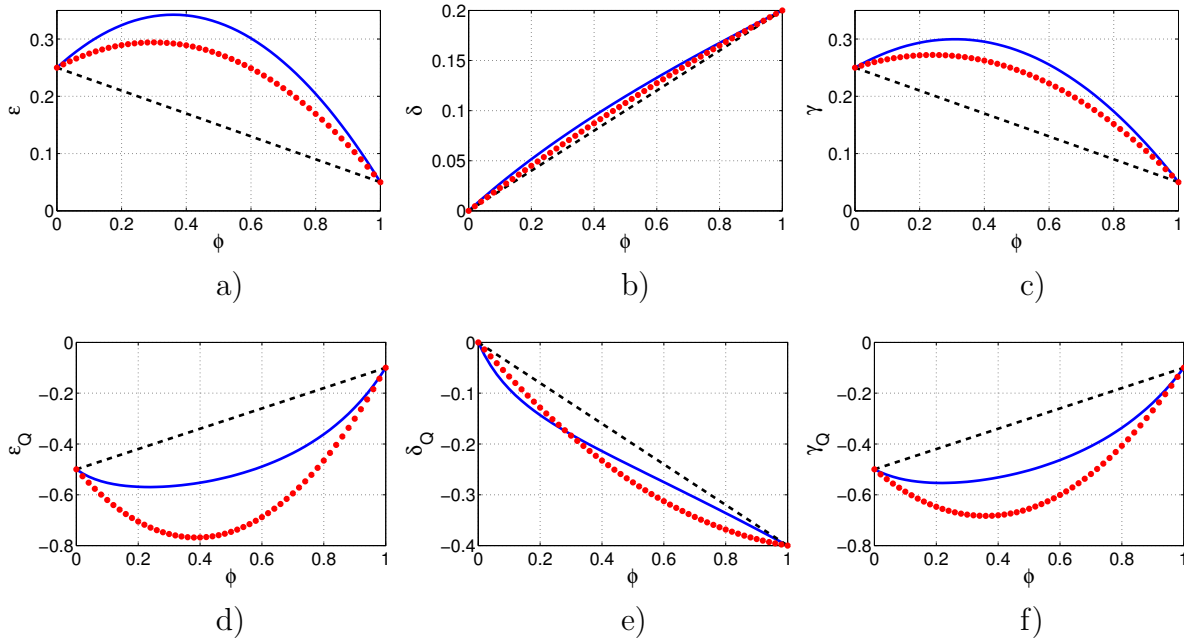


Figure 5.6. Effective velocity-anisotropy (a-c) and attenuation-anisotropy (d-f) parameters for a model with the same values of $\epsilon^{(1,2)}$, $\delta^{(1,2)}$, $\gamma^{(1,2)}$, $\epsilon_Q^{(1,2)}$, $\delta_Q^{(1,2)}$, and $\gamma_Q^{(1,2)}$ as those in Figure 5.3 (Table 5.1), but for much higher contrasts in the stiffnesses: $\Delta c_{33}/\bar{c}_{33} = \Delta Q_{33}/\bar{Q}_{33} = 90\%$ and $\Delta c_{55}/\bar{c}_{55} = \Delta Q_{55}/\bar{Q}_{55} = 70\%$. For the first constituent, $V_{P0}^{(1)} = 3.2$ km/s, $V_{S0}^{(1)} = 1.55$ km/s, $\rho^{(1)} = 2.45$ g/cm³, $Q_{33}^{(1)} = 100$, and $Q_{55}^{(1)} = 80$. The exact parameters (solid lines) are plotted along with the first-order linear approximations (dashed) and the second-order approximations (dotted).

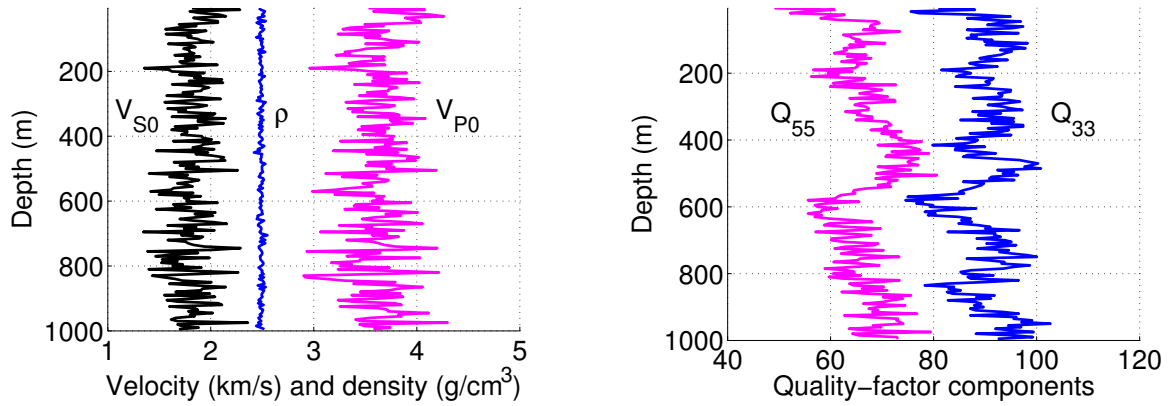


Figure 5.7. Vertical velocities, density, and the quality-factor components Q_{33} and Q_{55} of one realization of a model composed of VTI layers with VTI attenuation. The sampling interval is 5 m.

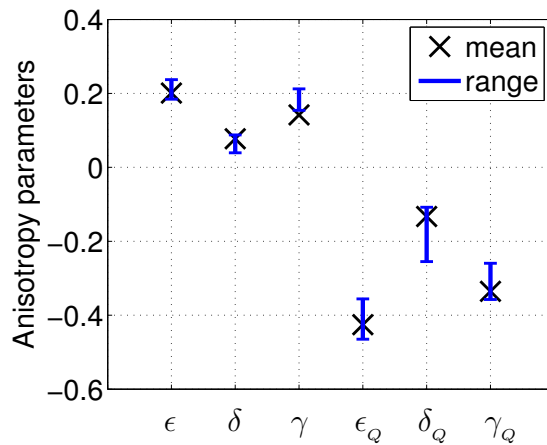


Figure 5.8. Mean values (crosses) of the interval anisotropy parameters and ranges (bars) of the exact effective parameters computed for 2000 realizations of the model from Figure 5.7. The standard deviations of all model parameters are listed in the text.

effective anisotropy parameters for a two-constituent isotropic model are given by

$$\gamma = 2\phi(1 - \phi) \frac{x^2}{1 - x^2}, \quad (5.43)$$

$$\begin{aligned} \gamma_Q &= -8\phi(1 - \phi)xx_Q \\ &\quad / [\phi(1 + x)(1 + x_Q) + (1 - \phi)(1 - x)(1 - x_Q)] \\ &\quad / [\phi(1 - x) + (1 - \phi)(1 + x)], \end{aligned} \quad (5.44)$$

where ϕ is the volume fraction of the first constituent, while $x \equiv (c_{55}^{(2)} - c_{55}^{(1)}) / (c_{55}^{(2)} + c_{55}^{(1)})$ and $x_Q \equiv (Q_{55}^{(2)} - Q_{55}^{(1)}) / (Q_{55}^{(2)} + Q_{55}^{(1)})$ denote the property contrasts between the constituents. In agreement with the discussion above, equation 5.44 shows that a contrast in the attenuation parameter Q_{55} is not sufficient to produce attenuation anisotropy. The parameter γ_Q also vanishes if the velocity contrast is not accompanied by an attenuation contrast, which is not the case for the parameters ϵ_Q and δ_Q .

It is clear from equation 5.43 that the velocity parameter γ is always positive and finite for layered media composed of two different isotropic constituents. This result remains valid for any number of constituents. The possible range of values of γ_Q is not immediately obvious from equation 5.44. For the special case $\phi = 50\%$, γ_Q has to be greater than -1, but this lower bound directly follows from the definition of the parameters γ_Q and ϵ_Q (equations 2.24 and 2.28). It is difficult to estimate the upper and lower bounds of the parameter δ_Q analytically even for the simple two-constituent model.

Therefore, to study the distribution of the effective parameters for a representative set of more complicated models composed of multiple isotropic (for both velocity and attenuation) constituents, I perform numerical simulations. First, I compute the anisotropy parameters of 2000 models using uniform random distributions for the interval velocities and density. The histograms of the effective anisotropy parameters for a relatively small number of constituents (two to five) are displayed in Figure 5.9. As expected, the velocity-anisotropy parameters ϵ and γ are predominantly positive with the exception of a few realizations, and generally do not exceed 0.5. Another velocity-anisotropy parameter, δ , can be either positive or negative with the mean value close to zero. This is consistent with the results of Monte Carlo simulations that positive and negative δ are equally likely for finely layered media (Berryman et al., 1999). In contrast to ϵ and γ , all three effective attenuation-anisotropy parameters have an almost even distribution around the zero value and a much wider variation. For example, δ_Q can take large negative values approaching -2. However, the vast majority of the attenuation-anisotropy parameters fall within the range $[-1, 1]$.

In the next simulation (Figure 5.10), the maximum number of constituents is increased to 200 (the minimum number is still two). The most noticeable change in the histograms is a much more narrow distribution of both velocity-anisotropy and attenuation-anisotropy parameters, which suggests that the contributions of multiple random constituents partially cancel each other. As a result, the absolute values of the attenuation-anisotropy parameters do not exceed 0.5. Also, the distribution peaks of the parameters ϵ and γ (but not δ) are shifted toward positive values.

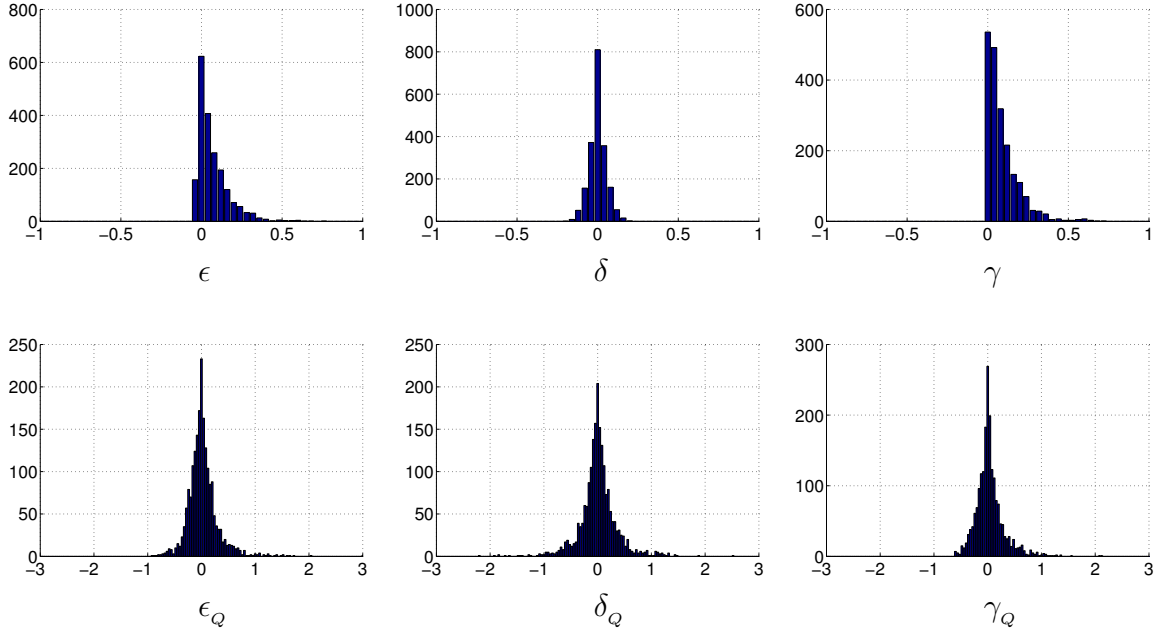


Figure 5.9. Histograms of the effective anisotropy parameters computed for 2000 randomly chosen models composed of isotropic (for both velocity and attenuation) constituents. The vertical axis shows the frequency of the parameter values. The ranges of the interval parameters are: $V_{P0} = 2000 - 6000$ m/s, $V_{S0} = 1000 - 3000$ m/s (the vertical P-to-SV velocity ratio was kept between 1.5 and 2.5), $\rho = 2000 - 4000$ kg/m³, $Q_{33} = 30 - 300$, and $Q_{55} = 30 - 300$. The number of constituents is randomly chosen between two and five.

It should be emphasized that the tests described above were performed for models without intrinsic velocity or attenuation anisotropy. The numerical analysis shows that making the constituents anisotropic not only moves the distribution peaks (especially, if the average value of the parameter is not zero), but also changes the shape of the histograms.

5.6 Effective symmetry for azimuthally anisotropic media

The examples in the previous sections were generated for purely isotropic or VTI constituents, in which both velocity and attenuation are independent of azimuth. The effective velocity and attenuation functions in such models are also azimuthally isotropic, and the equivalent homogeneous medium has VTI symmetry.

The general averaging equations 5.8-5.13, however, hold for any symmetry of the interval stiffness matrix and can be used to study layered azimuthally anisotropic media. An interesting issue that arises for such models is whether or not the effective velocity and attenuation anisotropy have different principal symmetry directions (i.e., different azimuths of

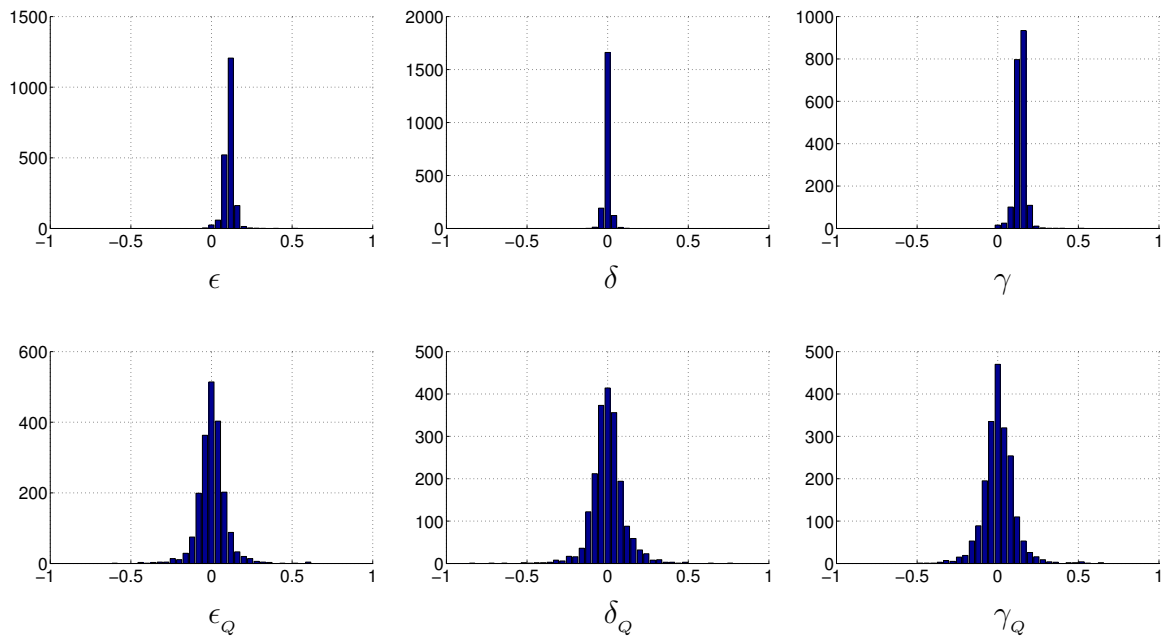


Figure 5.10. Same as Figure 5.9, but the number of constituents is randomly chosen between two and 200.

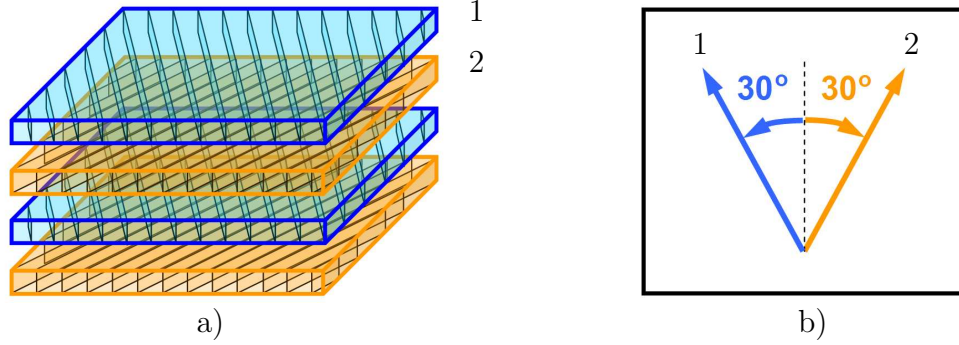


Figure 5.11. a) Layered model composed of two HTI constituents with the same volume ($\phi_1 = \phi_2 = 50\%$), one of which is elastic while the other one has HTI attenuation. b) Plan view of the symmetry-plane directions. The azimuth of the symmetry plane for the first (elastic) constituent is 30° toward northwest (NW); for the second constituent, the azimuth is 30° NE. The velocity parameters for both constituents are: $\rho = 2000 \text{ g/cm}^3$, $V_{P0} = 3 \text{ km/s}$, $V_{S0} = 2 \text{ km/s}$, $\epsilon = 0.2$, $\delta = 0.05$, and $\gamma = 0.2$. For the second constituent, the attenuation parameters are: $Q_{33}^{(2)} = 100$, $Q_{55}^{(2)} = 80$, $\epsilon_Q^{(2)} = -0.4$, $\delta_Q^{(2)} = -0.1$, and $\gamma_Q^{(2)} = -0.4$.

the vertical symmetry planes). Here, without attempting to give a comprehensive analysis of this problem, I discuss a numerical example for the simple model in Figure 5.11, which includes two constituents with HTI symmetry. The first constituent is purely elastic, while the second has HTI attenuation with the same symmetry axis as that for the velocity function. The velocity parameters (i.e., the real part of the stiffness matrix) of both constituents are identical, but the symmetry axes have different orientations (Figure 5.11b).

The effective P-wave phase velocity and normalized attenuation coefficient \mathcal{A} were computed from the Christoffel equation using the effective stiffnesses given by equations 5.8-5.13. The coefficient \mathcal{A} was obtained under the assumption of homogeneous wave propagation (i.e., the planes of constant amplitude are taken to be parallel to the planes of constant phase). Since both HTI constituents in this model have identical velocity parameters and the same volume, the real part of the effective stiffness matrix should have orthorhombic symmetry. This conclusion is confirmed by the computation of the effective phase-velocity function in the horizontal plane and two vertical coordinate planes, one of which bisects (with the azimuth 90°) the symmetry-plane directions (see Figure 5.11). The shape of the phase-velocity curves in Figures 5.12a,c shows that the symmetry planes of the effective orthorhombic velocity surface are aligned with the coordinate planes.

In contrast to the velocity surface, the effective normalized attenuation coefficient is not symmetric with respect to any vertical plane (Figure 5.12b). Because of the coupling between the the real and imaginary parts of the effective stiffness matrix, the effective at-

tenuation has a lower symmetry close to monoclinic. Also the extrema of the coefficient \mathcal{A} in the horizontal plane do not correspond to the symmetry planes of the effective velocity surface. The minimum value of \mathcal{A} occurs at an azimuth of 65° , while the maximum at 175° . Since the layering in this model is horizontal and both constituents have a horizontal symmetry axis, the monoclinic symmetry system for the effective attenuation has a horizontal symmetry plane (Figure 5.12d).

Next, I modify the model by reducing the magnitude of the intrinsic attenuation anisotropy ($\epsilon_Q^{(2)} = -0.1$, $\delta_Q^{(2)} = 0.03$, and $\gamma_Q^{(2)} = -0.1$; the other model parameters are the same as those in Figure 5.11). Since the real-values stiffnesses are kept unchanged, the effective velocity function practically coincides with that in Figures 5.12a,c. The horizontal and vertical cross-sections of the coefficient \mathcal{A} (Figure 5.13) show that the effective attenuation in this model is well described by orthorhombic, rather than monoclinic, symmetry. Hence, the effective velocity and attenuation for this model have the same symmetry. Their vertical symmetry planes, however, are misaligned by about 36° .

5.7 Discussion and conclusions

Interpretation of seismic amplitude measurements requires understanding of the physical reasons for attenuation in the seismic frequency band and, in particular, of the main factors responsible for attenuation anisotropy. Similar to velocity anisotropy, the effective attenuation coefficient can become directionally dependent due to interbedding of thin layers with different velocity and attenuation. Here, I studied the relationship between the effective Thomsen-style attenuation-anisotropy parameters (ϵ_Q , δ_Q , and γ_Q) and the properties of thin-layered media composed of attenuative isotropic or TI constituents.

The exact equations for the effective stiffness components in the long-wavelength limit were obtained using the Backus averaging technique. For attenuative media, the effective stiffnesses are complex, and the attenuation anisotropy depends on both the real and imaginary parts of the stiffness matrix. In contrast, the effective velocity function is almost entirely governed by the real-valued stiffnesses and, unless the attenuation is uncommonly strong, does not depend on the intrinsic attenuation parameters. Therefore, existing results on the effective velocity anisotropy of layered media remain valid for typical attenuative subsurface models.

To gain insight into the behavior of the attenuation-anisotropy parameters for thin-layered VTI media, I developed approximate solutions by assuming that the velocity and attenuation contrasts, as well as the interval velocity- and attenuation-anisotropy parameters, are small in absolute value. As is the case for velocity anisotropy, the first-order (linear in the small quantities) term in these approximations is given simply by the volume-weighted average of the corresponding interval parameter. The second-order (quadratic) terms reflect the coupling between different factors responsible for the effective attenuation anisotropy, such as that between the intrinsic anisotropy and heterogeneity. The second-order approximation, which includes both linear and quadratic terms, remains sufficiently accurate for models with strong property contrasts and pronounced intrinsic anisotropy.

It is noteworthy that even for models with isotropic constituents that have identical

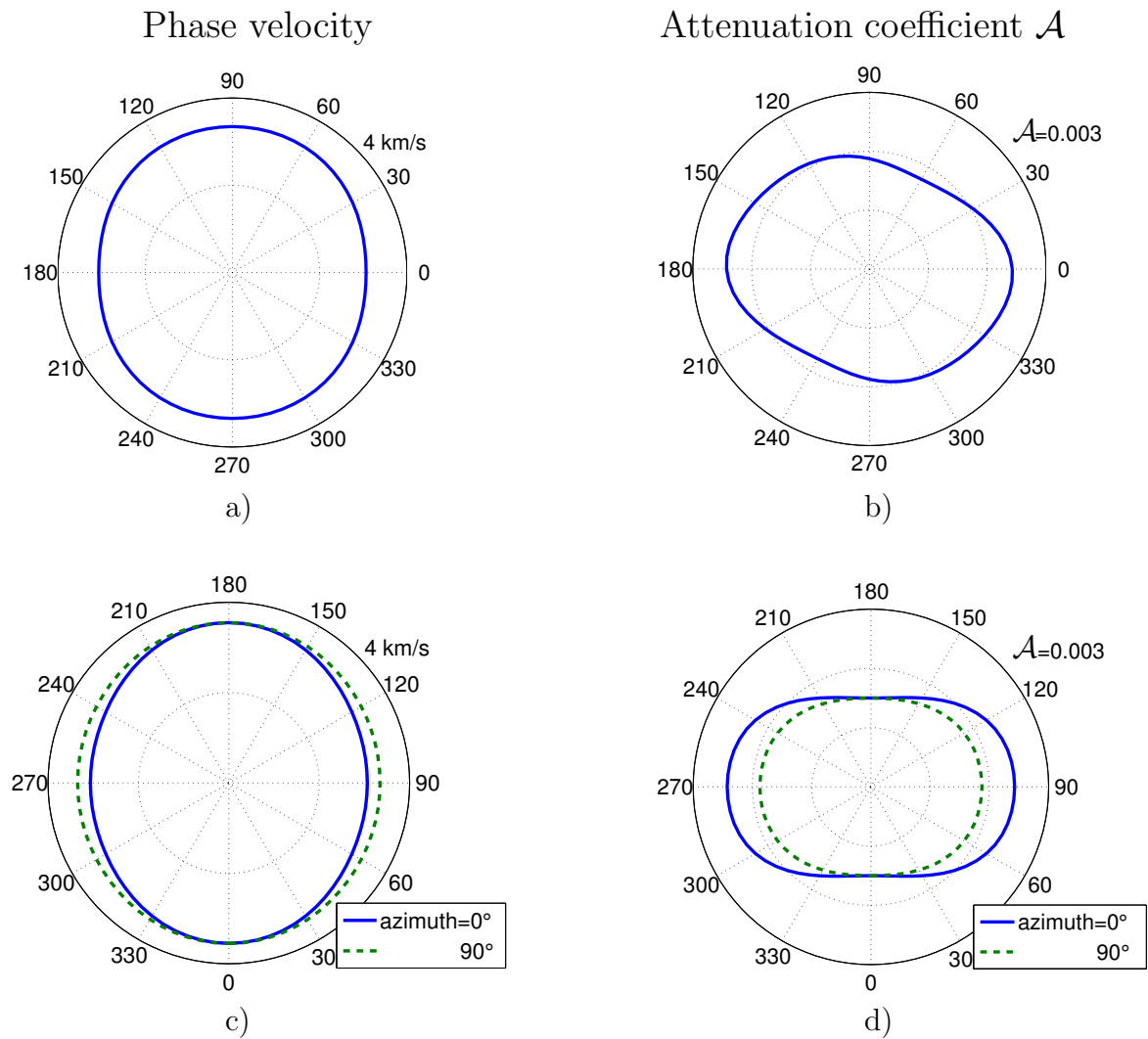


Figure 5.12. Effective P-wave phase velocity (left) and normalized attenuation coefficient (right) for the model from Figure 5.11. The velocity and attenuation are plotted in: (a,b) the horizontal plane as functions of the azimuthal phase angle; (c,d) the two vertical coordinate planes as functions of the polar phase angle.

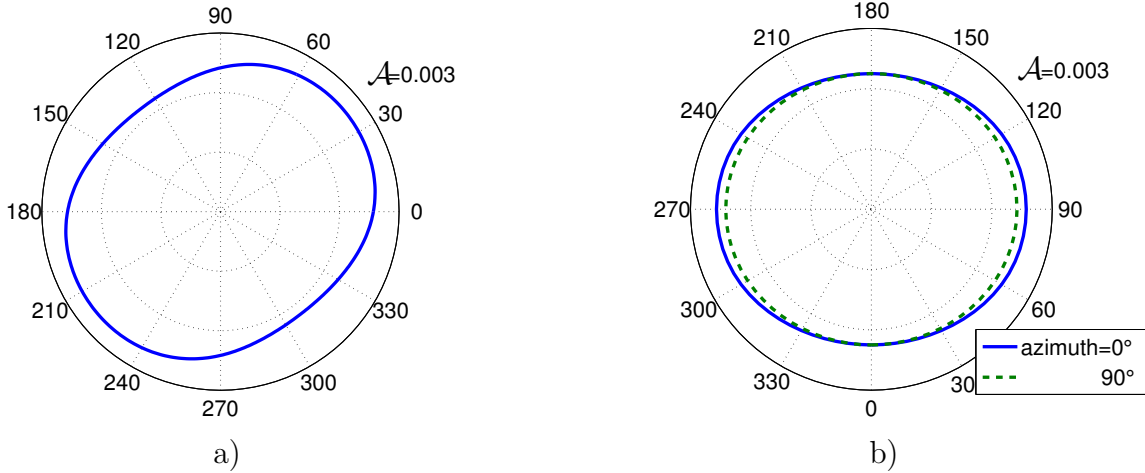


Figure 5.13. Horizontal (a) and vertical (b) cross-sections of the effective normalized attenuation coefficient for a model with relatively weak attenuation anisotropy. The model parameters are the same as those in Figure 5.11, except for $\epsilon_Q^{(2)} = -0.1$, $\delta_Q^{(2)} = 0.03$, and $\gamma_Q^{(2)} = -0.1$.

attenuation coefficients, the effective attenuation of P- and SV-waves is anisotropic, if the interval velocity changes across layer boundaries. However, jumps in the interval attenuation alone (i.e., not accompanied by a velocity contrast between isotropic constituent layers) do not create effective attenuation anisotropy. Because of the large contribution of the velocity contrasts to the quadratic attenuation terms, the accuracy of the linear (first-order) approximation for the attenuation-anisotropy parameters is primarily controlled by the strength of the interval velocity variations. For the same reason, the total contribution of the second-order terms tends to be higher for the attenuation parameters than for the velocity parameters. The relative magnitude of the overall velocity and attenuation anisotropy, however, is primarily dependent on the average values of the corresponding interval parameters (i.e., on the first-order term).

In addition to several tests for two-constituent models, I performed extensive numerical simulations for more complicated media composed of up to 200 constituents. To evaluate the upper and lower bounds of the attenuation anisotropy caused entirely by heterogeneity, all constituents were isotropic in terms of both velocity and attenuation. While the distributions of the parameters ϵ_Q , δ_Q , and γ_Q are centered at zero, their values cover a wider range (at least from -0.5 to 0.5) than that for the velocity-anisotropy parameters.

Although this chapter is mainly devoted to azimuthally isotropic models, I also evaluated the effective anisotropy for an HTI medium that includes two constituents with different azimuths of the symmetry axis. Such changes in the symmetry direction are often related

to variations of the dominant fracture azimuth with depth. If the intrinsic attenuation anisotropy is sufficiently strong, the velocity and attenuation functions of the effective medium may have different symmetries (e.g., orthorhombic versus monoclinic). Even when both velocity and attenuation are described by orthorhombic models, their vertical symmetry planes may be misaligned. These results have to be taken into account in field measurements of attenuation over fractured reservoirs.

Chapter 6

Far-field radiation from seismic sources in 2D attenuative anisotropic media

6.1 Summary

In this chapter, I present an asymptotic (far-field) study of 2D radiation patterns for media with anisotropic velocity and attenuation functions. Application of saddle-point integration helps to evaluate the inhomogeneity angle and test the common assumption of homogeneous wave propagation, which ignores the misalignment of the wave and attenuation vectors. For transversely isotropic media, the inhomogeneity angle vanishes in the symmetry directions and remains small if the model has weak attenuation and weak velocity and attenuation anisotropy. Reflection and transmission at medium interfaces, however, can substantially increase the inhomogeneity angle, which has an impact on both the attenuation coefficients and radiation patterns. Numerical analysis indicates that the attenuation vector deviates from the wave vector toward the direction of increasing attenuation.

The combined influence of angle-dependent velocity and attenuation results in pronounced distortions of radiation patterns, with the contribution of attenuation anisotropy rapidly increasing as the wave propagates away the source. The asymptotic solution also helps to establish the relationship between the phase and group parameters when wave propagation cannot be treated as homogeneous. Whereas the phase and group velocities are almost independent of attenuation, the inhomogeneity angle has to be taken into account in the relationship between the phase and group attenuation coefficients.

6.2 Introduction

To avoid complications associated with the inhomogeneity angle, wave propagation is often treated as homogeneous (Chapters 2–4). For layered media or models with strong attenuation anisotropy, however, the influence of the inhomogeneity angle on the wave propagation needs to be taken into account.

For plane waves in attenuative media, a wide range of values of inhomogeneity angle satisfy the Christoffel equation, except for certain *forbidden* directions (Krebes and Le, 1994; Carcione and Cavallini, 1995; Červený and Pšenčík, 2005). Because different choices of the inhomogeneity angle yield different plane-wave properties, the inhomogeneity angle is an important free parameter for plane-wave propagation. The energy (hence the attenuation behavior) of a wave excited by a seismic source, however, is determined by the boundary

conditions, so the inhomogeneity angle is constrained as well. For reflected and transmitted waves, the inhomogeneity angle can be found from Snell's law, which requires that the projection of the complex wave vector onto the interface is preserved (e.g., Hearn and Krebs, 1990; Carcione, 2001). Point-source radiation patterns in elastic anisotropic media, based on high-frequency asymptotics, have been extensively discussed in the literature (e.g. Tsvankin and Chesnokov, 1990; Gajewski, 1993). Hearn and Krebs (1990) describe ray tracing for inhomogeneous wave propagation in a medium consisting of a stack of isotropic attenuative layers, with the inhomogeneity angle obtained by the method of steepest descent for the stationary rays (i.e, the rays that satisfy Fermat's principle). Krebs and Slawinski (1991) find that method more accurate than an alternative approach that assigns parameters for the initial ray segment emerging from the source in a non-attenuative region.

In this chapter, I extend the steepest descent method to wavefields from seismic sources in 2D homogeneous media with anisotropic velocity and attenuation functions. To evaluate the far-field displacement represented with a contour integral, I apply the saddle-point condition to the phase function expressed through the polar angle. This asymptotic solution and numerical examples allow us to evaluate the magnitude of the inhomogeneity angle and its influence on the radiation patterns and phase and group attenuation coefficients.

6.3 Inhomogeneity angle

The wavefield in 2D attenuative anisotropic media can be represented through an integral in the frequency-wavenumber domain (equation G.2). In the high-frequency limit, this integral can be evaluated using the steepest-descent method. In the polar coordinate system, the saddle-point condition for the phase function (equation G.7) yields a complex value $\tilde{\theta}_s$ of the polar angle (the $\tilde{}$ sign denotes a complex value). The expression for the saddle point $\tilde{\theta}_s$ (equation G.8) is a generalization of the corresponding elastic case; the real-valued polar angle and slowness are replaced by their complex counterparts. Thereafter, I will call the imaginary part of the wave vector \mathbf{k} the *attenuation vector*, and the real part of \mathbf{k} simply the *wave vector*. The wave vector and attenuation vector are then determined from $\tilde{\theta}_s$ and the complex slowness \tilde{p}_s . The latter is obtained from the Christoffel equation for attenuative media.

Note that neither the real nor imaginary part of $\tilde{\theta}_s$ is the angle of either the wave vector or the attenuation vector. Similarly, neither the real nor imaginary part of \tilde{p}_s is the magnitude of either the wave vector or the attenuation vector. The angle and magnitude of both the wave vector and the attenuation vector can be obtained from $\tilde{\theta}_s$ and \tilde{p}_s in the following way.

I denote the magnitude of the real-valued slowness vector by $p = \frac{k}{\omega}$ and the magnitude of the frequency-normalized attenuation vector by $p^I = \frac{k^I}{\omega}$, where ω is the angular frequency, $k = |\mathbf{k}|$ is the magnitude of the wave vector \mathbf{k} , and $k^I = |\mathbf{k}^I|$ is the magnitude of the attenuation vector \mathbf{k}^I . The components of \tilde{p}_s are then rewritten as

$$\tilde{p}_1 = p \sin \theta + ip^I \sin \theta^I; \quad \tilde{p}_3 = p \cos \theta + ip^I \cos \theta^I, \quad (6.1)$$

where θ and θ^I are the angles between vertical and the wave and attenuation vectors, respectively. Jointly solving equations 6.1 and G.9 yields

$$p = \pm \sqrt{p_s^2 \cosh^2 \theta_s^I + (p_s^I)^2 \sinh^2 \theta_s^I}, \quad (6.2)$$

$$p^I = \pm \sqrt{(p_s^I)^2 \cosh^2 \theta_s^I + p_s^2 \sinh^2 \theta_s^I}, \quad (6.3)$$

$$\tan \theta = \frac{p_s \sin \theta_s \cosh \theta_s^I - p_s^I \cos \theta_s \sinh \theta_s^I}{p_s \cos \theta_s \cosh \theta_s^I + p_s^I \sin \theta_s \sinh \theta_s^I}, \quad (6.4)$$

$$\tan \theta^I = \frac{p_s^I \sin \theta_s \cosh \theta_s^I + p_s \cos \theta_s \sinh \theta_s^I}{p_s^I \cos \theta_s \cosh \theta_s^I - p_s \sin \theta_s \sinh \theta_s^I}, \quad (6.5)$$

where $p_s = \text{Re}[\tilde{p}_s]$, $p_s^I = \text{Im}[\tilde{p}_s]$, $\theta_s = \text{Re}[\tilde{\theta}_s]$, and $\theta_s^I = \text{Im}[\tilde{\theta}_s]$. The inhomogeneity angle is then given by $\theta^I - \theta$. For elastic media, both \tilde{p}_s and $\tilde{\theta}_s$ are real and equations 6.4 and 6.5 yield $\theta^I - \theta = 90^\circ$.

When the medium is not just attenuative, but also anisotropic, the complex slowness varies with respect to the complex polar angle at the saddle point ($\left. \frac{d\tilde{p}_s}{d\theta} \right|_{\theta=\tilde{\theta}_s} \neq 0$). If the medium is homogeneous and isotropic for both velocity and attenuation, equation G.8 has a real-valued solution

$$\tilde{\theta}_s = \frac{x_1}{x_3}, \quad (6.6)$$

so that $\theta_s = \frac{x_1}{x_3}$ and $\theta_s^I = 0$. I then find from equations 6.4 and 6.5 that $\theta = \theta^I = \theta_s$, which implies the inhomogeneity angle in homogeneous media with isotropic velocity and attenuation is always zero.

6.4 VTI media with VTI attenuation

6.4.1 SH-waves

For attenuative media with an anisotropic velocity function, the inhomogeneity angle generally does not vanish. The exact saddle-point condition for SH-waves in VTI (transverse isotropy with a vertical symmetry axis) media with VTI attenuation takes the form

$$\tan \tilde{\theta}_s = \frac{x_1}{x_3(1+2\gamma)} \frac{1 - \frac{i}{Q_{55}}}{1 - i \frac{1 + \gamma_Q}{Q_{55}}}, \quad (6.7)$$

where γ_Q is the SH-wave attenuation-anisotropy parameter (equation 2.24). Clearly, $\gamma_Q = 0$ yields a real-valued $\tilde{\theta}_s$ and results in homogeneous wave propagation. Equation 6.7 (as well as equations 6.10 and 6.11 below) shows that the imaginary part of $\tilde{\theta}_s$ is generally a small quantity proportional to the inverse Q factor.

Using equations G.9, 6.1, and 6.7, I find for the inhomogeneity angle of the SH-wave:

$$\sin \theta \cos \theta + \mathcal{A}_{SH}^2 \sin \theta^I \cos \theta^I = \mathcal{A}_{SH} \sin(\theta^I - \theta) \frac{1 - (1 + \gamma_Q)/Q_{55}^2}{\gamma_Q/Q_{55}}, \quad (6.8)$$

where the normalized phase attenuation coefficient $\mathcal{A} \equiv \frac{k^I}{k} = \frac{p^I}{p}$ itself is a function of inhomogeneity angle (equation A.6). It is noteworthy that the attenuation anisotropy parameters, although originally designed for homogeneous wave propagation, can be used to characterize attenuation anisotropy for non-zero values of the inhomogeneity angle. For weakly attenuative media ($1/Q_{55} \ll 1$) with weak velocity and attenuation anisotropy ($|\gamma| \ll 1$ and $|\gamma_Q| \ll 1$), the inhomogeneity angle can be simplified by dropping all quadratic terms in Q_{55} , γ , and γ_Q :

$$\theta^I - \theta = \tan^{-1}(\gamma_Q \sin 2\theta). \quad (6.9)$$

The largest inhomogeneity angle occurs at, e.g., $\theta = 45^\circ$. Note that the sign of the inhomogeneity angle is governed by the attenuation-anisotropy parameter γ_Q and the phase angle θ . For example, positive γ_Q yields positive inhomogeneity angles for $0^\circ < \theta < 90^\circ$, while negative γ_Q produces negative inhomogeneity angles. Analysis of the sign of $\theta^I - \theta$ for the whole range of phase directions reveals that the attenuation vector of the SH-wave deviates toward higher-attenuation directions.

Equation 6.9 also shows that for weak attenuation anisotropy ($|\gamma_Q| \ll 1$), the inhomogeneity angle for SH-waves is small. Then the SH-wave attenuation can be approximately found using the expression for homogeneous wave propagation (equation 2.27).

6.4.2 P- and SV-waves

The saddle point $\tilde{\theta}_s$ for P- and SV-waves in VTI media with VTI attenuation has a more complicated form. In the limit of weak attenuation and weak anisotropy for both velocity and attenuation, the saddle-point condition for P-waves can be simplified by dropping quadratic terms in $1/Q_{33}$, $1/Q_{55}$, ϵ , δ , ϵ_Q , and δ_Q :

$$\tan \tilde{\theta}_s = \frac{x_1}{x_3} \left[1 - 2\epsilon + 2(\epsilon - \delta) \cos 2\tilde{\theta}_s + i \frac{\epsilon_Q - (\epsilon_Q - \delta_Q) \cos 2\tilde{\theta}_s}{Q_{33}} \right], \quad (6.10)$$

where ϵ_Q and δ_Q are the attenuation-anisotropy parameters for P- and SV-waves (equations 2.28 and 2.31). The corresponding expression for SV-waves is

$$\tan \tilde{\theta}_s = \frac{x_1}{x_3} \left(1 - 2\sigma \cos 2\tilde{\theta}_s + i \frac{\sigma_Q \cos 2\tilde{\theta}_s}{Q_{55}} \right), \quad (6.11)$$

where g and g_Q are given, respectively, in equations 2.33 and 2.39. The velocity- and attenuation-anisotropy parameters for SV-waves, σ and σ_Q , are given in equations 2.40 and

Model #	ϵ	δ	ϵ_Q	δ_Q
1	0.1	0.05	-0.2	-0.1
2	0.4	0.25	-0.45	-0.5
3	0.1	0.05	0	0
4	0.4	0.25	0	0
5	0	0	-0.2	-0.1
6	0	0	-0.45	-0.5

Table 6.1. Attenuative VTI models with $V_{P0} = 3$ km/s, $V_{S0} = 1.5$ km/s, $\rho = 2.4$ g/cm³, $Q_{33} = 100$, and $Q_{55} = 60$.

2.42, respectively. It is noteworthy that the condition for SV-waves (equation 6.11) can be obtained directly from that for P-waves using the following substitutions: $\epsilon \rightarrow 0$, $\delta \rightarrow \sigma$, $\epsilon_Q \rightarrow 0$, $\delta_Q \rightarrow \sigma_Q$, and $Q_{33} \rightarrow Q_{55}$.

Although the imaginary terms $i \frac{\epsilon_Q - (\epsilon_Q - \delta_Q) \cos 2\tilde{\theta}_s}{Q_{33}}$ in equation 6.10 and $i \frac{\sigma_Q \cos 2\tilde{\theta}_s}{Q_{55}}$ in equation 6.11 involve only attenuation-anisotropy parameters, the dependence of $\tilde{\theta}_s$ on the real terms makes $\theta_s^I = \text{Im}[\tilde{\theta}_s]$ a function of the anisotropy parameters for both velocity and attenuation. The angle $\tilde{\theta}_s$ for P- and SV-waves is real only when the imaginary terms in equations 6.10 and 6.11, respectively, are equal to zero. For P-waves, this requires that the normalized attenuation coefficient be isotropic ($\epsilon_Q = \delta_Q = 0$). SV-wave propagation becomes homogeneous if the normalized attenuation coefficient is elliptical ($\sigma_Q = 0$). For general attenuative VTI models, $\tilde{\theta}_s$ in equations 6.10 and 6.11 can be calculated in iterative fashion. The inhomogeneity angle is then obtained from equations 6.2–6.5, as illustrated by numerical examples below.

6.4.3 Numerical examples

To evaluate the magnitude of the inhomogeneity angle for homogeneous attenuative VTI media, I use models 1 and 2 from Table 6.1. Figure 6.1 displays the wave vector \mathbf{k} (thin arrows) and the attenuation vector \mathbf{k}^I (thick arrows) for models 1 and 2. Both \mathbf{k} and \mathbf{k}^I are calculated with a constant increment in the group angle and displayed on the group-velocity curves (wavefronts). Notice that the wave vector remains perpendicular to the wavefront since the influence of the attenuation on the velocity function is of the second order. The attenuation vector, however, deviates from the normal to the wavefront because of the combined influence of the velocity and attenuation anisotropy. The angle between the wave vector and the corresponding attenuation vector is equal to the inhomogeneity angle. Clearly, the inhomogeneity angle does not vanish away from the symmetry axis and isotropy plane.

The exact inhomogeneity angle computed from equation G.8 is shown in Figure 6.2. For

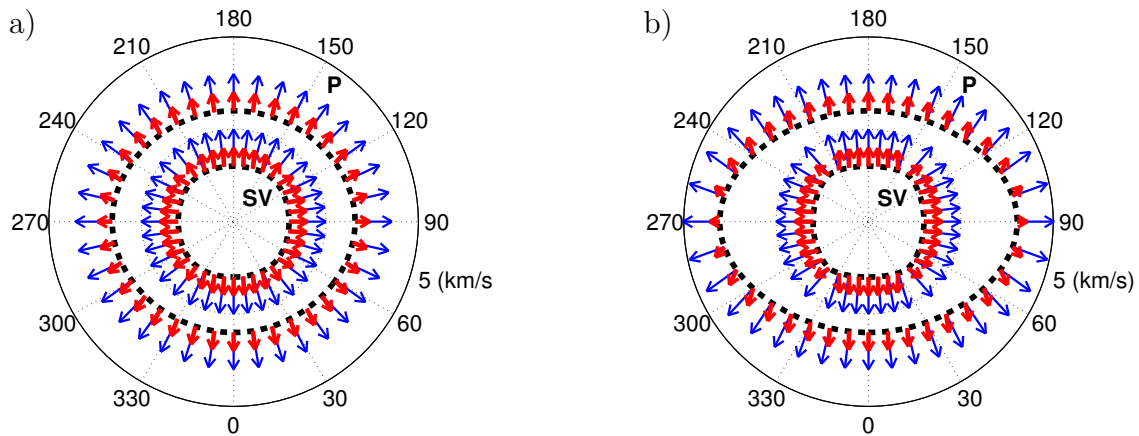


Figure 6.1. Polar plots of the wave vector \mathbf{k} (thin black arrows) and the attenuation vector \mathbf{k}^I (thick gray arrows) associated with the group-velocity curves (dashed) of P- and SV-waves for two VTI models from Table 6.1: a) model 1; b) model 2.

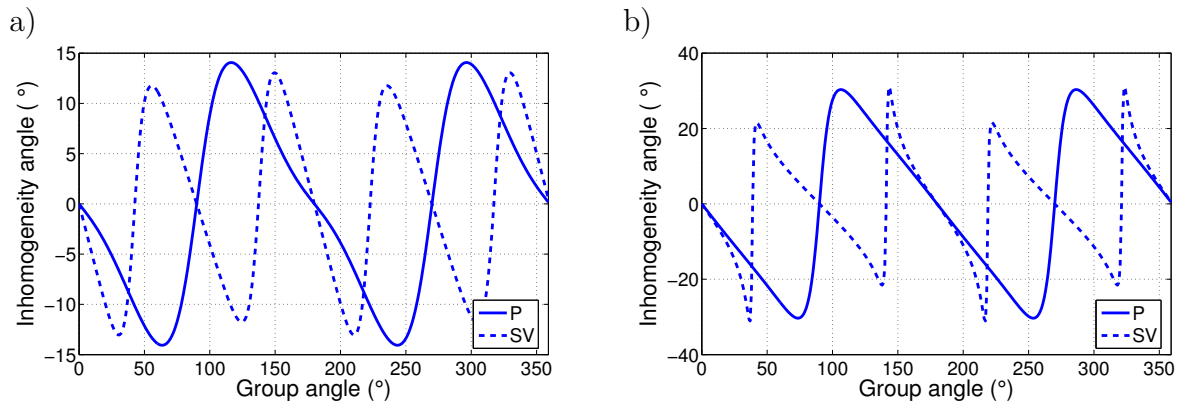


Figure 6.2. Exact inhomogeneity angles of P- and SV-waves for a) model 1; and b) model 2.

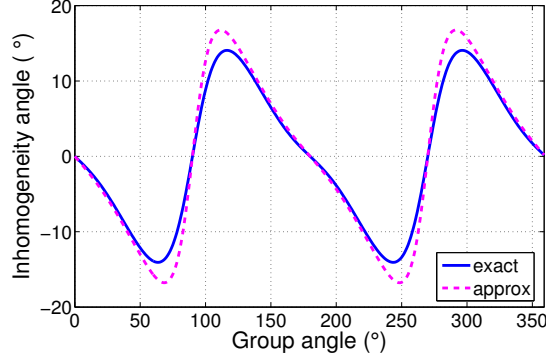


Figure 6.3. Comparison of the exact and approximate inhomogeneity angles for P-waves in model 1.

model 1, the inhomogeneity angles for both P- and SV-waves are less than 15° (Figure 6.2a). Since model 2 has stronger anisotropy for both velocity and attenuation, the inhomogeneity angles for it is larger (Figure 6.2b). For 2D homogeneous VTI model, the inhomogeneity angle always vanishes in the symmetry directions (0° and 90°). Figure 6.2b also shows that the inhomogeneity angle for SV-waves in model 2 changes rapidly near the velocity maximum at 45° , where the SV-wave wavefront becomes almost rhomb-shaped due to the large value of $\sigma = 0.6$.

Both models have negative ϵ_Q and δ_Q , which implies that the normalized attenuation for P-waves decreases monotonically from the vertical toward the horizontal direction. The P-wave attenuation vectors in Figure 6.1 are closer to the vertical direction than are the associated wave vectors. For SV-waves the attenuation vectors in model 2 deviate from the associated wave vectors toward the vertical in the range $0^\circ - 40^\circ$, where the attenuation coefficient decreases with the angle. For group angles between 50° and 90° , the opposite is true. This example, along with other numerical tests, suggests that the attenuation vector deviates from the wave vector toward the directions of increasing attenuation.

To test the accuracy of the approximate saddle-point condition for P-waves (equation 6.10), I compared it with the exact solution (Figure 6.3). The approximation generally provides sufficient accuracy, except for the directions where the term $\left. \frac{d\tilde{p}_s}{d\theta} \right|_{\theta=\tilde{\theta}_s}$ in equation G.8 becomes relatively large. The overall error, however, does not exceed 4° because of the weak velocity and attenuation anisotropy for this model. Predictably, increasing the anisotropy for either the velocity or attenuation reduces the accuracy of the approximate solution.

6.5 Radiation patterns

Consider the wavefield from a line source in 2D attenuative anisotropic media described in the $[x_1, x_3]$ -plane, where the source array function is independent of the x_2 coordinate. The spectrum of the particle displacement in the high-frequency limit, given in Appendix G, is similar to that for elastic media, but the slowness and stationary polar angle are complex. According to equation G.12, anisotropic attenuation alters the radiation patterns through the geometrical spreading factor in the denominator and an exponential decay term.

The influence of attenuation on the real and imaginary parts of the slowness \tilde{p}_s is of the second- and first-order, respectively, in the inverse Q factors. As a result, the geometrical spreading factor depends only on quadratic and higher-order terms in the inverse Q components.

6.5.1 Phase and group properties

The contribution of attenuation to the radiation pattern is mostly contained in the exponentially decaying term $\exp[-\omega p^I(\sin \theta^I x_1 + \cos \theta^I x_3)]$ (equation G.12). By analyzing this exponential term, I obtain the general relationship between the phase and group velocities as well as that between the phase- and group-attenuation coefficients:

$$V_G = \frac{\omega}{k_s \cos(\phi - \theta_s) \cosh \theta_s^I - k_s^I \sin(\phi - \theta_s) \sinh \theta_s^I}, \quad (6.12)$$

$$k_G^I = k_s \sin(\phi - \theta_s) \sinh \theta_s^I + k_s^I \cos(\phi - \theta_s) \cosh \theta_s^I, \quad (6.13)$$

where $k_s = \omega/p_s$, $k_s^I = \omega/p_s^I$, and ϕ is the group angle.

For homogeneous wave propagation ($\theta_s^I = 0$), the phase angle $\theta = \theta_s$ (equation 6.4) and the real slowness $p = p_s$ (equation 6.2). Hence, equations 6.12 and 6.13 reduces to (Zhu and Tsvankin, 2004)

$$V_G = \frac{V}{\cos(\phi - \theta)}, \quad (6.14)$$

$$k_G^I = k^I \cos(\phi - \theta), \quad (6.15)$$

where $V = \omega/k$ is the phase velocity. Hence, the group attenuation coefficient for homogeneous wave propagation is equal to the phase attenuation coefficient multiplied (rather than divided, as is the case for phase velocity) by the cosine of the angle between the phase and group directions. If both functions are isotropic, the phase direction is identical to the corresponding group direction, and there is no difference between the phase and group quantities.

Since both k_s^I and θ_s^I are relatively small quantities proportional to the inverse Q factor, the influence of the inhomogeneity angle on the group velocity is of the second order in the inverse Q and can be ignored. Hence, equation 6.14 for the group velocity remains accurate for any value of the inhomogeneity angle. The influence of the inhomogeneity angle on the group attenuation coefficient, however, is of the first order in the inverse Q and can be

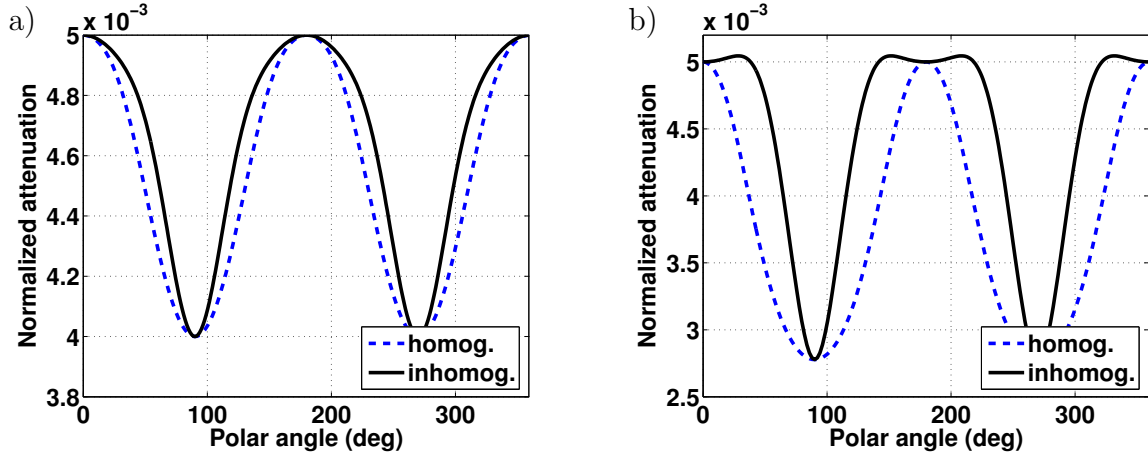


Figure 6.4. P-wave attenuation coefficients for a) model 1; and b) model 2. The solid curves are computed with the inhomogeneity angle from Figure 6.2, the dashed curves with the inhomogeneity angle set to zero for all propagation directions.

significant.

6.5.2 Numerical examples

To examine the influence of the inhomogeneity angle on the radiation patterns and the angular variation of the phase and group attenuation coefficients as well as radiation patterns, I use VTI models from Table 6.1. The contribution of the inhomogeneity angle to the P-wave attenuation coefficient is illustrated in Figure 6.4. The solid curves are calculated using the inhomogeneity angles obtained from Figure 6.2, while the dashed curves correspond to homogeneous wave propagation (i.e., zero inhomogeneity angle). Since model 1 is weakly anisotropic for both velocity and attenuation, the inhomogeneity angle is relatively small and has a small impact on attenuation coefficients (Figure 6.4a). In contrast, the larger inhomogeneity angles for model 2 result in a more pronounced error in the attenuation coefficients computed for homogeneous wave propagation.

The group attenuation coefficient is also influenced by the inhomogeneity angle (Figure 6.5). For model 2, the attenuation coefficient computed with the actual inhomogeneity angle (equation 6.13) deviates by up to 20% from that for homogeneous wave propagation (equation 6.15).

To analyze the radiation patterns in the presence of attenuation anisotropy, I compute the particle displacement of P- and SV-waves from a vertical single force for models 1 and 2 (Figure 6.6). The stronger anisotropy for both velocity and attenuation in model 2 creates a more pronounced directional dependence of the radiation patterns compared to that in model 1.

Since both models have the same Q_{33} and Q_{55} values, the vertical attenuation coeffi-

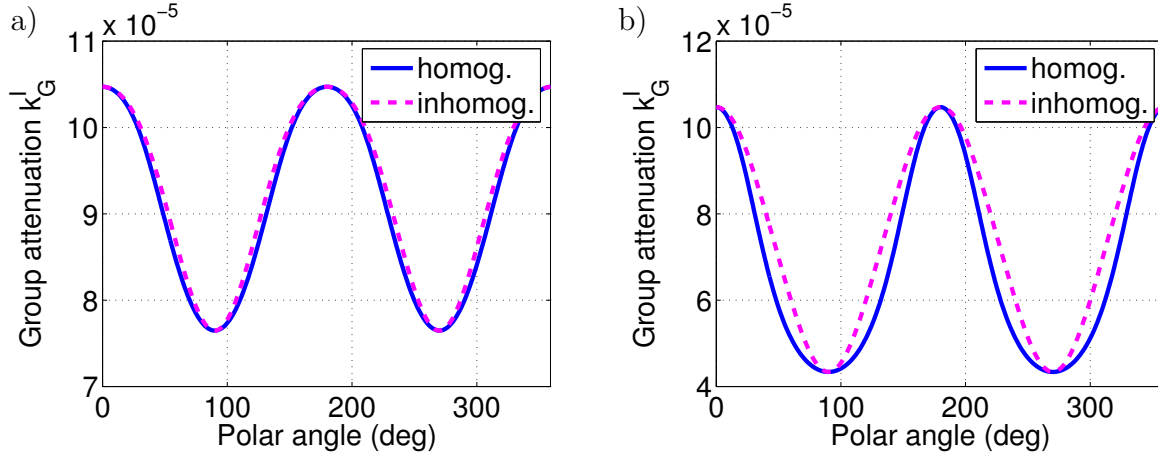


Figure 6.5. Group attenuation coefficients for a) model 1; and b) model 2.

coefficients are also the same. However, the difference between the parameter δ in the two models changes the term $\left. \frac{d^2 \tilde{p}_s}{d\theta^2} \right|_{\theta=\tilde{\theta}_s}$ in equation G.12 and, therefore, the magnitude of the particle displacement in the vertical symmetry direction (Tsvankin, 2005).

Although the attenuation-anisotropy parameter δ_Q also contributes to the term $\left. \frac{d^2 \tilde{p}_s}{d\theta^2} \right|_{\theta=\tilde{\theta}_s}$, its influence on the geometrical-spreading factor in the symmetry direction is practically negligible.

To understand the relative influence of the velocity and attenuation anisotropy on the radiation patterns, I compare the particle displacement of P- and SV-waves excited by the same vertical single force in models 3–6 of Table 6.1. The directional dependence of the radiation patterns for both P- and SV-waves remains pronounced even without attenuation anisotropy (Figures 6.7, solid curves). The radiation patterns deviate significantly from the reference isotropic values, especially for model 4, which has a particularly strong velocity anisotropy. A more detailed analysis of the P- and SV-wave radiation patterns in TI media can be found in Tsvankin (2005, Chapter 2). The directional dependence of the radiation patterns becomes much less pronounced in the absence of velocity anisotropy (Figures 6.7, dashed curves).

This numerical analysis confirms the known fact that the influence of velocity anisotropy on radiation patterns remains almost the same for different source-receiver distances. In contrast, the distortions of the radiation patterns caused by attenuation anisotropy become much more pronounced with distance because the decaying term $\exp[-\omega p^I(\sin \theta^I x_1 + \cos \theta^I x_3)]$ in equation G.12 varies with the spatial coordinates (compare the dashed curves in Figure 6.7c,d and Figure 6.8).

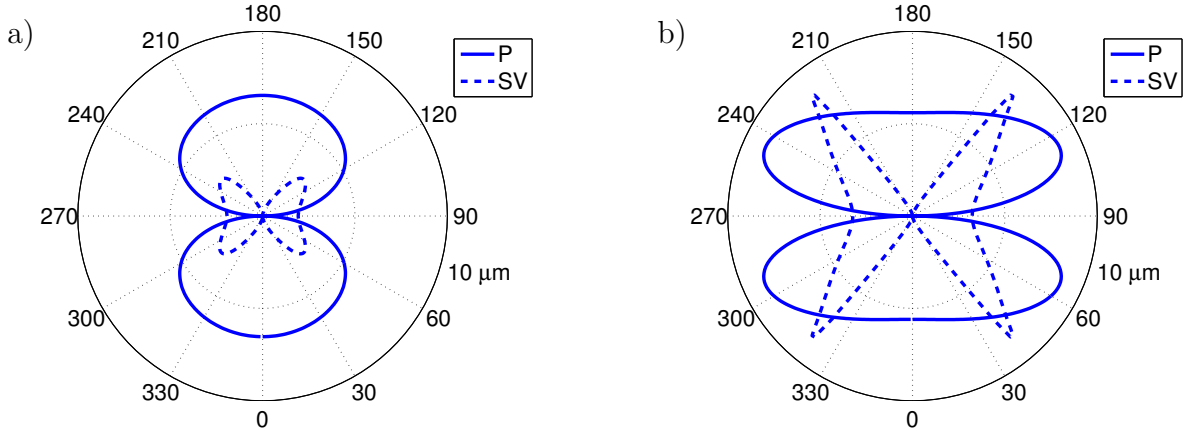


Figure 6.6. Radiation patterns of P-waves (solid curves) and SV-waves (dashed) from a vertical force ($f_3 = 10^5$ N) in a) model 1; and b) model 2. The magnitude of the particle displacement is computed at a distance of 1000 m away from the force; the frequency is 100 Hz.

6.6 Discussion and conclusions

The inhomogeneity angle plays an essential role in wavefield simulation for attenuative media, especially if the velocity and attenuation functions are anisotropic. Here, I analyze the inhomogeneity angle in the far field of a line source (i.e., independent of the x_2 direction) by applying the saddle-point (stationary-phase) condition to the plane-wave decomposition of the wavefield.

The discussion is largely devoted to homogeneous media with constant velocity and attenuation, where the inhomogeneity angle can be studied analytically. Although the inhomogeneity angle vanishes only in the symmetry directions, its magnitude is relatively small for weakly attenuative media with weak anisotropy for both velocity and attenuation. Therefore, for such models the attenuation coefficient can be computed under the simplifying assumption of homogeneous wave propagation. For media with VTI symmetry for both velocity and attenuation the phase attenuation direction is shifted from that of the wave vector toward increasing attenuation.

For layered models, the take-off inhomogeneity angle at the source location can substantially change during reflection/transmission at medium interfaces. The wave vectors of reflected and transmitted waves are determined jointly by the Christoffel equation and Snell's law for attenuative media. The resulting inhomogeneity angle can be large even if the layers are weakly attenuative and are characterized by weak anisotropy for both velocity and attenuation. If a wave is transmitted from a purely elastic medium into an attenuative layer, the attenuation vector is always perpendicular to the interface. For example, the inhomogeneity angle of waves transmitted through the ocean bottom into the underwa-

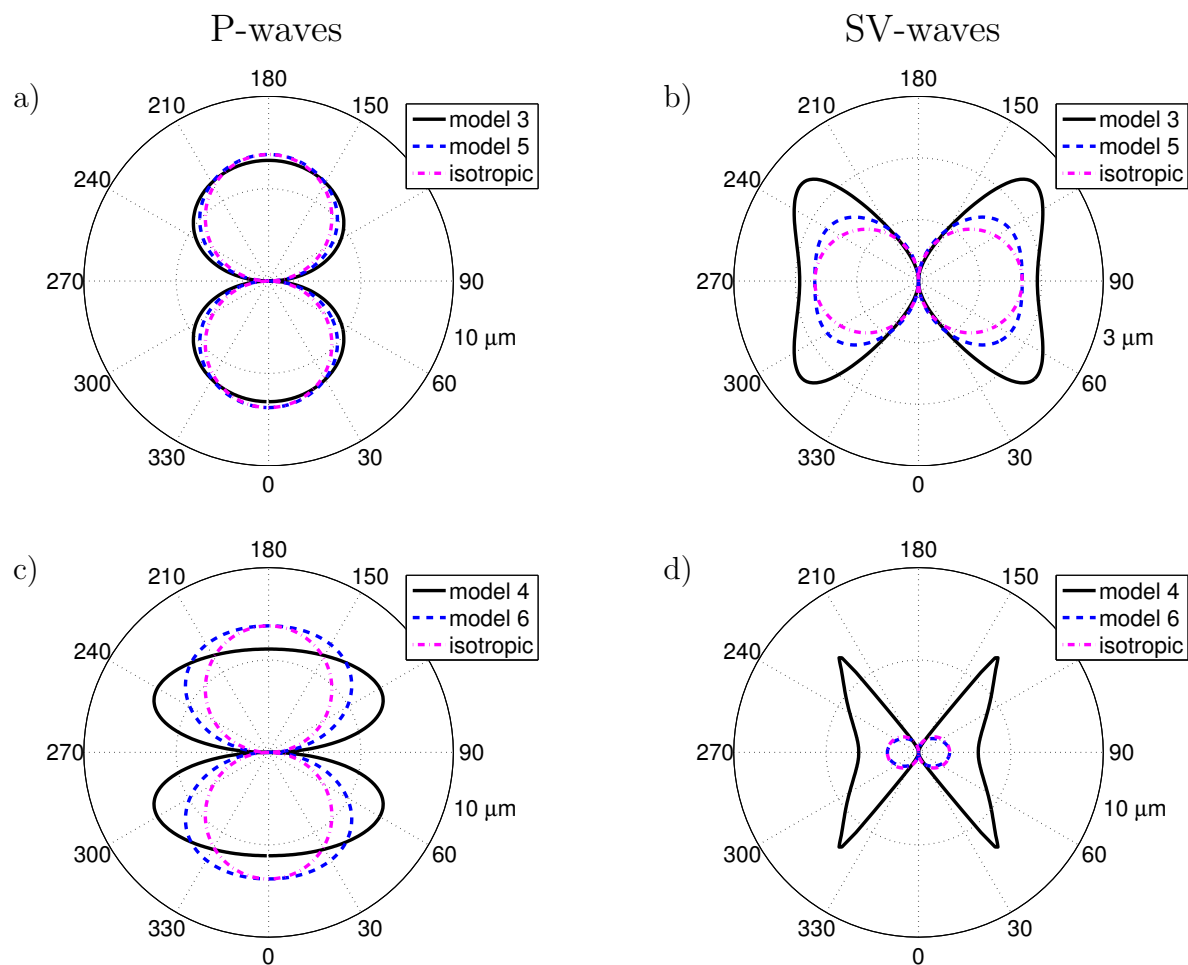


Figure 6.7. Radiation patterns of P- waves (left) and SV-waves (right) from a vertical force ($f_3 = 10^5 \text{ N}$). The solid and dotted curves mark, respectively, the radiation patterns of P- and SV-waves for a,b) models 3 and 5 (Table 6.1); and c,d) models 4 and 6. The dash-dotted curves correspond to the reference isotropic models with isotropic attenuation (i.e., for $\epsilon = \delta = \epsilon_Q = \delta_Q = 0$ with the other parameters kept fixed). The source-receiver distance is 1000 m; the frequency is 100 Hz.

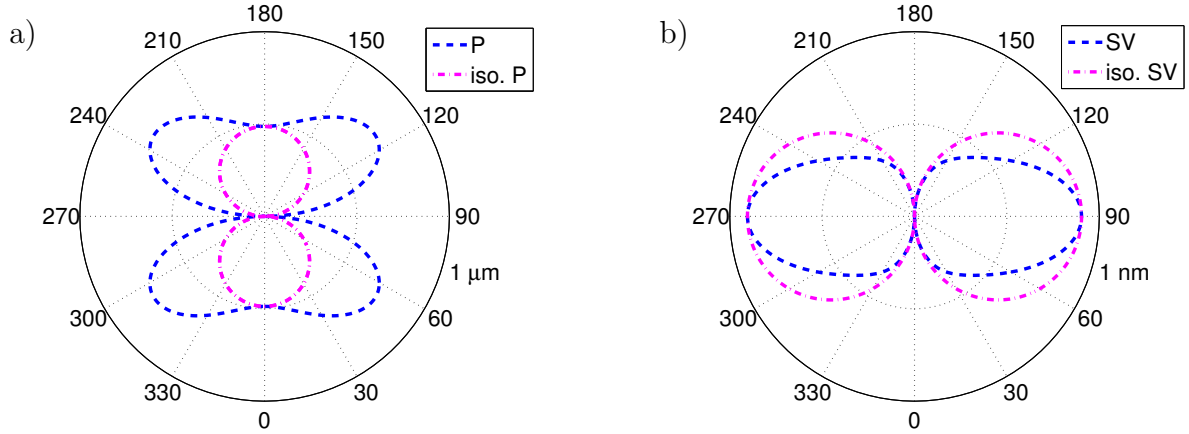


Figure 6.8. Radiation patterns of a) P- waves and b) SV-waves for model 6 computed at a distance of 3000 m away from the source. The dash-dotted and dotted curves mark, respectively, the radiation patterns of P- and SV-waves for the corresponding isotropic models with isotropic attenuation.

ter layer with non-negligible attenuation coincides with the transmission angle (Carcione, 1999).

Along with anisotropic geometrical spreading, anisotropic attenuation in the overburden may distort the AVO response of reflected waves. The numerical examples in this chapter illustrate the influence of both velocity and attenuation anisotropy on the radiation patterns. Whereas the directional amplitude variations caused by velocity anisotropy can be substantial, they do not change with source-receiver distance. In contrast, since the magnitude of the attenuation factor increases with distance, so do the amplitude distortions caused by attenuation anisotropy.

To process seismic data from attenuative media, it is necessary to relate the phase attenuation coefficient to the group (effective) attenuation along seismic rays that can be measured from recorded amplitudes. For homogeneous wave propagation, the phase velocity is equal to the projection of the corresponding group-velocity vector onto the phase direction. The relationship between the phase and group attenuation involves the same factor (the cosine of the angle between the two vectors), but it is the group attenuation that is equal to the projection of the corresponding phase-attenuation vector onto the group direction. If the inhomogeneity angle is not zero, the group velocity and attenuation depend on both the wave and phase-attenuation vectors. Still, the relationship between group and phase velocity is accurately represented by equation 6.14 for homogeneous wave propagation. The group attenuation coefficient, however, is described by a more complicated expression that reduces to the projection of the phase-attenuation coefficient onto the group direction only for a small inhomogeneity angle.

The analysis here was limited to 2D media in which the attenuation vector is confined to the vertical propagation plane and governed by a single (polar) angle. The results of this chapter should be valid for any vertical plane in azimuthally isotropic homogeneous media and symmetry planes of azimuthally anisotropic media. In general, the attenuation vector in either heterogeneous or azimuthally anisotropic media is described not just by the polar angle θ^I , but also by the azimuthal angle ϕ^I . Therefore, rigorous 3D treatment of radiation patterns in anisotropic attenuative media requires application of a higher-dimensional version of the steepest-descent method.

Chapter 7

Conclusions and recommendations

7.1 Conclusions

Directional variation of attenuation, along with that of velocity, can strongly distort the amplitudes and polarizations of seismic waves and, therefore, has serious implications for AVO analysis. In this thesis I developed a consistent treatment of attenuation anisotropy in the presence of velocity anisotropy. To analyze wave propagation in attenuative anisotropic media, both the stiffness coefficients and wave vectors have to be treated as complex quantities. Attenuation anisotropy is characterized by the quality-factor matrix \mathbf{Q} , with each element defined as the ratio of the real and imaginary parts of the corresponding stiffness element. Then the anisotropic velocity function and attenuation coefficients are obtained from the Christoffel equation in terms of the real stiffness components and quality-factor components. For attenuative media with negligible dispersion, the influence of the quality-factor components on phase velocity is of the second order and typically can be ignored. Hence, velocity analysis can generally be performed using algorithms designed for elastic media.

To facilitate the description of TI attenuation, I follow the idea of Thomsen's (1986) notation for velocity anisotropy and replace the quality-factor components by two reference isotropic quantities (wavenumber-normalized attenuation coefficients for P- and SV-waves along the symmetry axis) and three dimensionless anisotropic parameters (ϵ_Q , δ_Q , and γ_Q). This new notation reflects the coupling between the velocity and attenuation anisotropy. For fracture reservoirs that are often characterized by HTI or orthorhombic symmetry, I extended the notation of attenuation anisotropy from attenuative TI media by employing the principle of Tsvankin's (1997) notation for orthorhombic velocity. The analysis of plane-wave attenuation for TI and orthorhombic media is limited to homogeneous wave propagation in models with aligned symmetry directions for the velocity and attenuation functions.

To gain analytical insight into the plane-wave propagation in attenuative TI and orthorhombic media, I developed approximate solutions for the attenuation coefficients by assuming that attenuation and anisotropy (for both velocity and attenuation) are weak. Approximate normalized attenuation coefficients for P-, SV-, and SH-waves in TI media, as well as those of P-waves for orthorhombic media, have the same form as the corresponding linearized phase-velocity function. Moreover, similar to the P-wave phase-velocity function, attenuation coefficients for P-waves are governed by a reduced set of parameters. Because of the non-negligible influence of the velocity anisotropy on attenuation coefficients, however,

accurate inversion of attenuation measurements requires prior anisotropic velocity analysis.

Since case studies involving anisotropic attenuation measurements are scarce, I measured the P-wave attenuation coefficients on a synthetic model for a wide range of propagation angles. To account for the difference between the phase and group attenuation coefficients, I extended the spectral-ratio method to anisotropic materials. Laboratory measurements not only corroborate the conclusions of previous experimental studies that attenuation is often more sensitive to anisotropy than are phase velocity or reflection coefficient, but also indicates the potential of anisotropic attenuation measurements for field data applications.

To explore physical reasons for attenuation anisotropy, I studied the effective parameters of finely layered attenuative media. Approximate solutions are used to analyze the influence of various factors (such as heterogeneity and intrinsic anisotropy for both velocity and attenuation) on effective attenuation anisotropy. Interestingly, the effective attenuation for P- and SV-waves is anisotropic even for a medium composed of isotropic layers with no attenuation contrast, provided there is velocity variation among the constituent layers. Contrasts in the intrinsic isotropic attenuation, however, do not create attenuation anisotropy, unless they are accompanied by velocity contrasts. Extensive numerical simulations for layered models composed of various number of isotropic (in terms of both velocity and attenuation) constituents demonstrate that the distributions of the parameters ϵ_Q , δ_Q , and γ_Q are centered at zero, while their values cover a wider range than that for the velocity-anisotropy parameters.

I also studied far-field radiation from seismic sources in 2D attenuative anisotropic media. Whereas the influence of velocity anisotropy on radiation patterns remains almost the same for different source-receiver distances, distortion of radiation patterns caused by attenuation anisotropy can change significantly with distance.

Comprehensive analysis of wave propagation in attenuative media requires taking the inhomogeneity angle into account. The inhomogeneity angle is generally small for weakly attenuative, homogeneous media with weak anisotropy for both velocity and attenuation, and reduces to zero in the symmetry directions. Moreover, for general attenuative anisotropic media, the difference between the phase and group attenuation coefficients has a strong impact on the attenuation-anisotropy parameters obtained from field measurement of attenuation.

7.2 Recommendations

Still, this thesis did not address a number of important theoretical issues. For example, analysis of reflection/transmission coefficients in attenuative anisotropic media would help both AVO analysis and forward-modeling algorithms such as ray tracing (e.g., Carcione, 1997). Linearized expressions for reflection/transmission coefficients in terms of the velocity and attenuation contrasts, as well as velocity- and attenuation-anisotropy parameters, can provide physical insight into the behavior of the reflected/transmitted waves.

I have tested the validity of two assumptions used in Chapters 2–4: identical symmetry orientation for velocity and attenuation, and homogeneous wave propagation (the

inhomogeneity angle set to zero). If a model is composed of two alternating attenuative HTI constituents (thin layers) with different azimuths of the symmetry axis, the symmetry direction of the effective velocity function can differ from that of the effective attenuation coefficient. The issue of different symmetry systems for velocity and attenuation has to be explored further, especially for models with depth-varying fracture direction.

For weakly attenuative, homogeneous media with weak anisotropy for both velocity and attenuation, the assumption of negligible inhomogeneity angle is sufficiently accurate. For layered media, the inhomogeneity angle can change substantially during reflection/transmission at medium interfaces. This can strongly distort reflection/transmission coefficients, especially for large incidence angles.

Since this thesis is mainly focused on theoretical aspects (in addition to one chapter related to experimental measurements) of attenuation anisotropy, of importance for future work are the complications of field-data application of the analytical results.

Because of the scarcity of current case studies on anisotropic attenuation, a conclusive field-data application of anisotropic attenuation would greatly contribute to the study on this topic. For attenuative media without azimuthal variation (e.g., VTI), a 2D seismic line with sufficiently large offset-to-depth ratios can be used for estimating attenuation-anisotropic parameters based on, for example, the anisotropic spectral-ratio method discussed in Chapter 4. For azimuthally anisotropic attenuative media, wide-azimuth data are required to identify the principal directions of the attenuation coefficient and invert for the attenuation-anisotropy parameters. Since anisotropic attenuation can have significant influence on the amplitude of the wavefield, high-quality data are important for the success of attenuation anisotropy analysis. Moreover, a careful choice of the frequency band is critical for interpreting the magnitude of the attenuation-anisotropy parameters.

Perhaps the central question is how to use attenuation anisotropy as an attribute for lithology discrimination. Although attenuation is considered to be a key factor in estimating permeability (e.g., Akbar et al., 1993), the relationship between attenuation anisotropy and permeability anisotropy has not been established yet. As pointed out by Brown (2004), attenuation is not widely used yet as a major interpretation attribute but in the future it might yield more meaningful information on permeability. Perhaps, with the advancement of technology of seismic data acquisition and processing and the improvement of our understanding of the physical mechanisms of anisotropic attenuation, attenuation-anisotropy parameters will become valuable attributes in characterization of fractured reservoirs. To achieve this goal, we need to better understand the relationship between fracture parameters and attenuation, and improve methods of estimating attenuation from field measurements.

References

- Akbar, N., J. Dvorkin, and A. Nur, 1993, Relating P-wave attenuation to permeability: *Geophysics*, **58**, 20–29.
- Alford, R. M., 1986, Shear data in the presence of azimuthal anisotropy: 56th Annual International Meeting, Expanded Abstracts, 476–479.
- Alkhalifah, T. and I. Tsvankin, 1995, Velocity analysis for transversely isotropic media: *Geophysics*, **60**, 1550–1566.
- Arts, R. J. and P. N. J. Rasolofosaon, 1992, Approximation of velocity and attenuation in general anisotropic rocks: 62nd Annual International Meeting, Expanded Abstracts, 640–643.
- Backus, G. E., 1962, Long wave elastic anisotropy produced by horizontal layering: *J. Geophys. Res.*, **67**, 4427–4440.
- Bakulin, A., 2003, Intrinsic and layer-induced vertical transverse isotropy: *Geophysics*, **68**, 1708–1713.
- Bakulin, A. and V. Grechka, 2003, Effective anisotropy of layered media: *Geophysics*, **68**, 1817–1821.
- Bakulin, A., V. Grechka, and I. Tsvankin, 2000a, Estimation of fracture parameters from reflection seismic data - Part I: HTI model due to a single fracture set: *Geophysics*, **65**, 1788–1802.
- 2000b, Estimation of fracture parameters from reflection seismic data - Part II: Fractured models with orthorhombic symmetry: *Geophysics*, **65**, 1803–1817.
- 2000c, Estimation of fracture parameters from reflection seismic data - Part III: Fractured models with monoclinic symmetry: *Geophysics*, **65**, 1818–1830.
- Bakulin, A. and L. A. Molotkov, 1998, Application of complex Biot densities for the description of attenuation and dispersion in porous rocks: 60th Meeting, Expanded Abstracts, P085.
- Ben-Menahem, A. and S. J. Singh, 1981, *Seismic waves and sources*: Springer-Verlag.
- Bergman, M. I., 1997, Measurements of electric anisotropy due to solidification texturing and the implications for the Earth's inner core: *Nature*, **389**, 60–63.
- Berryman, J. G., 1979, Long-wave elastic anisotropy in transversely isotropic media: *Geophysics*, **44**, 896–917.
- Berryman, J. G., V. Y. Grechka, and P. Berge, 1999, Analysis of Thomsen parameters for finely layered VTI media: *Geophysical Prospecting*, **47**, 959–978.

- Best, A. I., 1994, Seismic attenuation anisotropy in reservoir sedimentary rocks: 64th Annual International Meeting, Expanded Abstracts, 822–825.
- Biot, M. A., 1956, Theory of propagation of elastic waves in a fluid-saturated porous solid, low- and higher-frequency range: *Journal of the Acoustical Society of America*, **28**, 168–191.
- 1962, Mechanics of deformation and acoustic propagation in porous media: *Journal of Applied Physics*, **33**, 1482–1498.
- Bland, D., 1960, *The theory of linear viscoelasticity*: Pergamon Press Inc.
- Blangy, J. P., 1994, AVO in transversely Isotropic media—An overview: *Geophysics*, **49**, 775–781.
- Borcherdt, R. D., G. Glassmoyer, and L. Wennerberg, 1986, Influence of welded boundaries in anelastic media on energy flow, and characteristics of P, S-I, and S-II waves: Observational evidence for inhomogeneous body waves in low-loss solids: *Journal of Geophysical Research*, **91**, 11503–11518.
- Borcherdt, R. D. and L. Wennerberg, 1985, General P, type-I S, and type-II S waves in anelastic solids: Inhomogeneous wave fields in low-loss solids: *Bulletin of the Seismological Society of America*, **75**, 1729–1763.
- Brajanovski, M., B. Gurevich, and M. Schoenberg, 2005, A model for P-wave attenuation and dispersion in a porous medium permeated by aligned fractures: *Geophysical Journal International*, **163**, 372–384.
- Brittan, J., M. Warner, and G. Pratt, 1995, Anisotropic parameters of layered media in terms of composite elastic properties: *Geophysics*, **60**, 1243–1248.
- Brown, A. R., 2004, *Interpretation of three-dimensional seismic data*: American Association of Petroleum Geologists and the Society of Exploration Geophysicists.
- Carcione, J. M., 1992, Anisotropic Q and velocity dispersion of finely layered media: *Geophysical Prospecting*, **40**, 761–783.
- 1997, Reflection and transmission of qP-qS plane waves at a plane boundary between viscoelastic transversely isotropic media: *Geophysical Journal International*, **129**, 669–680.
- 1999, Effects of vector attenuation on AVO of the offshore reflections: *Geophysics*, **64**, 815–819.
- 2001, *Wave fields in real media: Wave propagation in anisotropic, anelastic, and porous media*: Pergamon Press.
- Carcione, J. M. and F. Cavallini, 1995, On the acoustic-electromagnetic analogy: *Wave Motion*, **21**, 149–162.
- Červený, V. and I. Pšenčík, 2005, Plane waves in viscoelastic anisotropic media – I. Theory: *Geophysical Journal International*, **161**, 197–212.
- Chapman, M., 2003, Frequency dependent anisotropy due to meso-scale fractures in the presence of equant porosity: *Geophysical Prospecting*, **51**, 369–379.

- Chichinina, T., V. Sabinin, and G. Ronquillo-Jarrillo, 2004, P-wave attenuation anisotropy for fracture characterization: numerical modeling for reflection data: 74th Annual International Meeting, Expanded Abstracts, 143–146.
- Crampin, S., 1981, A review of wave motion in anisotropic and cracked media: *Wave Motion*, **3**, 349–391.
- 1991, Effects of singularities on shear-wave propagation in sedimentary basins: *Geophysical Journal International*, **107**, 531–543.
- Crampin, S. and S. Peacock, 2005, A review of shear-wave splitting in the compliant crack-critical anisotropic earth: *Wave Motion*, **41**, 59–77.
- Dewangan, P., 2004, Processing and inversion of mode-converted waves using the PP+PS=SS method: PhD thesis, Colorado School of Mines.
- Dewangan, P., I. Tsvankin, M. Batzle, K. van Wijk, and M. Haney, 2006, PS-wave moveout inversion for tilted TI media: A physical-modeling study: *Geophysics*, in print (July–August).
- Dvorkin, J., G. Mavko, and A. Nur, 1995, Squirt flow in fully saturated rocks: *Geophysics*, **60**, 97–107.
- Ferry, J. D., 1980, *Viscoelastic properties of polymers*: John Wiley & Sons.
- Gajewski, D., 1993, Radiation from point sources in general anisotropic media: *Geophysical Journal International*, **113**, 299–317.
- Gautam, K., M. Batzle, and R. Hofmann, 2003, Effect of fluids on attenuation of elastic waves: 73rd Annual International Meeting, Expanded Abstracts, 1592–1595.
- Gelinsky, S. and S. A. Shapiro, 1994, Poroelastic velocity and attenuation in media with anisotropic permeability: 64th Annual International Meeting, Expanded Abstracts, 818–821.
- Grechka, V., S. Theophanis, and I. Tsvankin, 1999, Joint inversion of P- and PS-waves in orthorhombic media: Theory and a physical-modeling study: *Geophysics*, **64**, 146–161.
- Grechka, V. and I. Tsvankin, 1999, 3-D moveout velocity analysis and parameter estimation for orthorhombic media: *Geophysics*, **64**, 820–837.
- 2002a, PP + PS = SS: *Geophysics*, **67**, 1961–1971.
- 2002b, Processing-induced anisotropy: *Geophysics*, **67**, 1920–1928.
- Hearn, D. J. and E. S. Krebes, 1990, On computing ray-synthetic seismograms for anelastic media using complex rays: *Geophysics*, **55**, 422–432.
- Helbig, K. and L. Thomsen, 2005, 75-plus years of anisotropy in exploration and reservoir seismics: A historical review of concepts and methods: *Geophysics*, **70**, 9ND23ND.
- Hiramatsu, Y. M. A., 1995, Attenuation anisotropy beneath the subduction zones in Japan: *Geophysical Research Letters*, **22**, 1653–1656.

- Hosten, B., M. Deschamps, and B. R. Tittmann, 1987, Inhomogeneous wave generation and propagation in lossy anisotropic solids: application to the characterization of viscoelastic composite materials: *Journal of the Acoustical Society of America*, **82**, 1763–1770.
- Johnston, D. H., 1981, Attenuation anisotropy in oil shale at ultrasonic frequencies: 51st Annual International Meeting, Expanded Abstracts, 101.
- Johnston, D. H. and M. N. Toksöz, 1981, Definitions and terminology, *in* D. H. Johnston, and M. N. Toksöz, ed., *Seismic wave attenuation*, Geophysics reprinted series 2, 1–5. Society of Exploration Geophysicists.
- Kibblewhite, A. C., 1989, Attenuation of sound in marine sediments: A review with emphasis on new low-frequency data: *Journal of the Acoustical Society of America*, **86**, 716–738.
- King, M., 2005, Rock-physics developments in seismic exploration: A personal 50-year perspective: *Geophysics*, **70**, 3ND–8ND.
- Krebes, E. S. and L. H. T. Le, 1994, Inhomogeneous plane waves and cylindrical waves in anisotropic anelastic media: *Journal of Geophysical Research*, **99**, 23899–23919.
- Krebes, E. S. and M. A. Slawinski, 1991, On raytracing in an elastic–anelastic medium: *Bulletin of the Seismological Society of America*, **81**, 667–686.
- Liu, E., S. Crampin, J. H. Queen, and W. D. Rizer, 1993, Velocity and attenuation anisotropy caused by microcracks and microfractures in a multiazimuth reverse VSP: *Canadian Journal of Exploration Geophysics*, **29**, 177–188.
- Lynn, H. and W. Beckham, 1998, P-wave azimuthal variations in attenuation, amplitude, and velocity in 3D field data: Implications for mapping horizontal permeability anisotropy: 68th Annual International Meeting, Expanded Abstracts, 193–196.
- Lynn, H. B., D. Campagna, K. M. Simon, and W. E. Beckham, 1999, Relationship of P-wave seismic attributes, azimuthal anisotropy, and commercial gas pay in 3-D P-wave multiazimuth data, Rulison Field, Piceance Basin, Colorado: *Geophysics*, **64**, 1293–1311.
- MacBeth, C., 1999, Azimuthal variation in P-wave signatures due to fluid flow: *Geophysics*, **64**, 1181–1192.
- Martin, N. W. and R. J. Brown, 1995, Estimating anisotropic permeability from attenuation anisotropy using 3C-2D data: Technical report, University of Calgary.
- Mateeva, A., 2003, Quantifying the uncertainties in absorption estimates from VSP spectral ratios: CWP Project Review, Colorado School of Mines, CWP–457.
- Maultzsch, S., M. Chapman, E. Liu, and X. Y. Li, 2003a, Modelling frequency-dependent seismic anisotropy in fluid-saturated rock with aligned fractures: Implication of fracture size estimation from anisotropic measurements: *Geophysical Prospecting*, **51**, 381–392.
- Maultzsch, S., S. Horne, S. Archer, and H. Burkhardt, 2003b, Effects of an anisotropic overburden on azimuthal amplitude analysis in horizontal transverse isotropic media: *Geophysical Prospecting*, **51**, 61–74.

- Mavko, G. M. and A. Nur, 1979, Wave attenuation in partially saturated rocks: *Geophysics*, **44**, 161–178.
- Molotkov, L. and A. Bakulin, 1998, Attenuation in the effective model of finely layered porous Biot media: 60th Meeting, Expanded Abstracts, P156.
- Parra, J. O., 1997, The transversely isotropic poroelastic wave equation including the Biot and the squirt mechanisms: Theory and application: *Geophysics*, **62**, 309–318.
- Pointer, T., E. Liu, and J. A. Hudson, 2000, Seismic wave propagation in cracked porous media: *Geophysical Journal International*, **142**, 199–231.
- Postma, G. W., 1955, Wave propagation in a stratified medium: *Geophysics*, **XX**, 780–806.
- Prasad, M. and A. Nur, 2003, Velocity and attenuation anisotropy in reservoir rocks: 73rd Annual International Meeting, Expanded Abstracts, 1652–1655.
- Sams, M. S., 1995, Attenuation and anisotropy: The effect of extra fine layering: *Geophysics*, **60**, 1646–1655.
- Sayers, C. M., 1994, The elastic anisotropy of shales: *Journal of Geophysics Research*, **99**, 767–774.
- Schoenberg, M. and K. Helbig, 1997, Orthorhombic media: Modeling elastic wave behavior in a vertically fractured earth: *Geophysics*, **62**, 1954–1974.
- Schoenberg, M. and F. K. Levin, 1974, Apparent attenuation due to intrabed multiples: *Geophysics*, **39**, 278–291.
- Schoenberg, M. and F. Muir, 1989, A calculus for finely layered anisotropic media: *Geophysics*, **54**, 581–589.
- Shapiro, S. A. and P. Hubral, 1996, Elastic waves in finely layered sediments: The equivalent medium and generalized Q'Doherty-Anstey formulas: *Geophysics*, **61**, 1282–1300.
- Shi, G. and J. Deng, 2005, The attenuation anisotropy of mudstones and shales in subsurface formations: *Science in China Series D—Earth Sciences*, **48**, 1882–1890.
- Souriau, A. and B. Romanowicz, 1996, Anisotropy in inner core attenuation: a new type of data to constrain the nature of the solid core: *Geophysical Research Letters*, **23**, 1–4.
- Stanley, D. and N. I. Christensen, 2001, Attenuation anisotropy in shale at elevated confining pressure: *International Journal of Rock Mechanics & Mining Sciences*, **38**, 1047–1056.
- Tao, G. and M. S. King, 1990, Shear-wave velocity and Q anisotropy in rocks: A laboratory study: *International Journal of Rock Mechanics and Mining Sciences and Geomechanics Abstracts*, **27**, 353–361.
- Thomsen, L., 1986, Weak elastic anisotropy: *Geophysics*, **51**, 1954–1966.
- Tsvankin, I., 1997, Anisotropic parameters and P-wave velocity for orthorhombic media: *Geophysics*, **62**, 1292–1309.
- 2005, *Seismic signatures and analysis of reflection data in anisotropic media*: Elsevier Science Publisher.

- Tsvankin, I. and E. M. Chesnokov, 1990, Synthesis of body wave seismograms from point sources in anisotropic media: *Journal of Geophysical Research*, **95**, 11317–11331.
- Upadhyay, S. K., 2004, *Seismic reflection processing: with special reference to anisotropy*: Springer.
- Vasconcelos, I. and E. Jenner, 2005, Estimation of azimuthally varying attenuation from surface seismic data: CWP Project Review, Colorado School of Mines, CWP-504.
- Wang, Z., 2002, Seismic anisotropy in sedimentary rocks, part 2: Laboratory data: *Geophysics*, **67**, 1423–1440.
- Werner, U. and S. A. Shapiro, 1999, Frequency-dependent shear-wave splitting in thinly layered media with intrinsic anisotropy: *Geophysics*, **64**, 604–608.
- White, J. E., 1975, Computed seismic speeds and attenuation in rocks with partial gas saturation: *Geophysics*, **40**, 224–232.
- Willis, M., R. Rao, D. Burns, J. Byun, and L. Vetri, 2004, Spatial orientation and distribution of reservoir fractures from scattered seismic energy: 74th Annual International Meeting, Expanded Abstracts, 1535–1538.
- Zhu, Y. and I. Tsvankin, 2004, Plane-wave propagation and radiation patterns in attenuative TI media: 74th Annual International Meeting, Expanded Abstracts, 139–142.
- 2006, Plane-wave propagation in attenuative TI media: *Geophysics*, **71**, T17–T30.
- Zhu, Y., I. Tsvankin, and P. Dewangan, 2006, Physical modeling and analysis of P-wave attenuation anisotropy in transversely isotropic media: *Geophysics*, under review.

Appendix A

Plane SH-waves in attenuative VTI media

The Christoffel equation for a plane SH-wave propagating in an attenuative VTI medium yields

$$\tilde{c}_{66}\tilde{k}_1^2 + \tilde{c}_{55}\tilde{k}_3^2 - \rho\omega^2 = 0, \quad (\text{A.1})$$

where $\tilde{c}_{ij} = c_{ij} + ic_{ij}^I$ are the complex stiffness coefficients. The complex wavenumber is represented as $\tilde{k}_i = k_i - ik_i^I$, where $k^I = \sqrt{k_1^{I2} + k_2^{I2} + k_3^{I2}}$ is the attenuation coefficient.

A.1 VTI \mathbf{Q} matrix: Inhomogeneous wave propagation

First, consider the general case of inhomogeneous wave propagation and allow the vectors \mathbf{k} and \mathbf{k}^I to make different angles (θ and θ^I , respectively) with the vertical symmetry axis. If the \mathbf{Q} matrix has VTI symmetry, equation (A.1) becomes

$$c_{66} \left(1 + \frac{i}{Q_{66}}\right) (k \sin \theta - ik^I \sin \theta^I)^2 + c_{55} \left(1 + \frac{i}{Q_{55}}\right) (k \cos \theta - ik^I \cos \theta^I)^2 - \rho\omega^2 = 0. \quad (\text{A.2})$$

Equation (A.2) can be separated into the real part,

$$c_{66} \left[k^2 \sin^2 \theta - (k^I)^2 \sin^2 \theta^I + \frac{1}{Q_{66}} 2kk^I \sin \theta \sin \theta^I \right] + c_{55} \left[k^2 \cos^2 \theta - (k^I)^2 \cos^2 \theta^I + \frac{1}{Q_{55}} 2kk^I \cos \theta \cos \theta^I \right] - \rho\omega^2 = 0, \quad (\text{A.3})$$

and the imaginary part,

$$c_{66} \left[\frac{1}{Q_{66}} (k^2 \sin^2 \theta - (k^I)^2 \sin^2 \theta^I) - 2kk^I \sin \theta \sin \theta^I \right] + c_{55} \left[\frac{1}{Q_{55}} (k^2 \cos^2 \theta - (k^I)^2 \cos^2 \theta^I) - 2kk^I \cos \theta \cos \theta^I \right] = 0. \quad (\text{A.4})$$

By introducing the SH-wave velocity-anisotropy parameter $\gamma \equiv (c_{66} - c_{55})/(2c_{55})$

(Thomsen, 1986), equation (A.4) can be rewritten as

$$k^2 \left[(1 + 2\gamma) \frac{Q_{55}}{Q_{66}} \sin^2 \theta + \cos^2 \theta \right] - (k^I)^2 \left[(1 + 2\gamma) \frac{Q_{55}}{Q_{66}} \sin^2 \theta^I + \cos^2 \theta^I \right] - 2kk^I Q_{55} [(1 + 2\gamma) \sin \theta \sin \theta^I + \cos \theta \cos \theta^I] = 0. \quad (\text{A.5})$$

The only physically meaningful solution of equation (A.5) is given by

$$\frac{k^I}{k} = \left\{ \sqrt{1 + \frac{\left[(1 + 2\gamma) \frac{Q_{55}}{Q_{66}} \sin^2 \theta + \cos^2 \theta \right] \left[(1 + 2\gamma) \frac{Q_{55}}{Q_{66}} \sin^2 \theta^I + \cos^2 \theta^I \right]}{Q_{55}^2 [\cos(\theta^I - \theta) + 2\gamma \sin \theta \sin \theta^I]^2}} - 1 \right\} \times \frac{Q_{55} [\cos(\theta^I - \theta) + 2\gamma \sin \theta \sin \theta^I]}{\left[(1 + 2\gamma) \frac{Q_{55}}{Q_{66}} \sin^2 \theta^I + \cos^2 \theta^I \right]}. \quad (\text{A.6})$$

For weakly attenuative media with $Q_{55} \rightarrow \infty$, the term $Q_{55} |\cos(\theta^I - \theta)|$ is much greater than unity, if the inhomogeneity angle $\theta^I - \theta \neq \pm 90^\circ$. Although it is possible for the conditions $Q_{55} \rightarrow \infty$ and $\theta^I - \theta = \pm 90^\circ$ to be satisfied simultaneously, models of this kind are not typical (Krebes and Slawinski, 1991). Therefore the square-root in equation (A.6) can be expanded in the small parameter $1/[Q_{55}^2 \cos^2(\theta^I - \theta)]$. Retaining only the linear term in this parameter yields

$$\frac{k^I}{k} = \frac{1}{2Q_{55}} \frac{(1 + 2\gamma) \frac{Q_{55}}{Q_{66}} \sin^2 \theta + \cos^2 \theta}{\cos(\theta^I - \theta) + 2\gamma \sin \theta \sin \theta^I}. \quad (\text{A.7})$$

If attenuation is weak $\left(\frac{1}{Q_{55}} \ll 1 \text{ and } \frac{1}{Q_{66}} \ll 1 \right)$, the inhomogeneity angle $\theta^I - \theta$ that appears in problems involving point sources in homogeneous media is small, so that $|\sin(\theta^I - \theta)| \ll 1$ (Ben-Menahem and Singh, 1981). Then, the contribution of the inhomogeneity angle in equation (A.7) is of the second order. Indeed, $\cos(\theta^I - \theta) \approx 1 - (\theta^I - \theta)^2/2$, while $\sin \theta^I$ can be represented as

$$\sin \theta^I = \sin \theta \cos(\theta^I - \theta) + \cos \theta \sin(\theta^I - \theta). \quad (\text{A.8})$$

Note that in equation (A.7) $\sin \theta^I$ is multiplied with Thomsen parameter γ . Therefore, if the velocity anisotropy is weak ($|\gamma| \ll 1$), all terms involving the inhomogeneity angle in the denominator of equation (A.7) are quadratic or higher-order in the small parameters. By further assuming that the attenuation anisotropy is weak ($|(Q_{55} - Q_{66})/Q_{66}| \ll 1$), equation (A.7) can be simplified by dropping all terms quadratic in the parameters $\sin(\theta^I - \theta)$

θ), γ , and $(Q_{55} - Q_{66})/Q_{66}$, yielding

$$\frac{k^I}{k} = \frac{1}{2Q_{55}} \left(1 + \frac{Q_{55} - Q_{66}}{Q_{66}} \sin^2 \theta \right). \quad (\text{A.9})$$

Analysis of the phase-velocity function [equation (A.3)] in the limit of small attenuation and weak attenuation and velocity anisotropy (not shown here) leads to a similar result: as long as the inhomogeneity angle is small, it contributes only to second-order terms.

A.2 VTI Q matrix: Homogeneous wave propagation

For homogeneous wave propagation ($\theta^I = \theta$), equation (A.5) takes a much simpler form:

$$k^2 - (k^I)^2 - 2Q_{55}\alpha k k^I = 0, \quad (\text{A.10})$$

where

$$\alpha \equiv \frac{(1 + 2\gamma) \sin^2 \theta + \cos^2 \theta}{(1 + 2\gamma) \frac{Q_{55}}{Q_{66}} \sin^2 \theta + \cos^2 \theta}. \quad (\text{A.11})$$

The physically meaningful solution is

$$\frac{k^I}{k} = \sqrt{1 + (Q_{55}\alpha)^2} - Q_{55}\alpha. \quad (\text{A.12})$$

The real part of the Christoffel equation [equation (A.3)] then reduces to

$$(c_{66} \sin^2 \theta + c_{55} \cos^2 \theta) \left[k^2 - (k^I)^2 + \frac{2kk^I}{Q_{55}\alpha} \right] - \rho\omega^2 = 0. \quad (\text{A.13})$$

The phase velocity of SH-waves is found as

$$V_{SH} = \frac{\omega}{k} = \xi_Q V_{SH}^{\text{elast}}, \quad (\text{A.14})$$

where V_{SH}^{elast} is the phase velocity in purely elastic VTI media,

$$V_{SH}^{\text{elast}} = \sqrt{\frac{c_{66} \sin^2 \theta + c_{55} \cos^2 \theta}{\rho}}, \quad (\text{A.15})$$

and ξ_Q is the factor responsible for the influence of the anisotropic attenuation:

$$\xi_Q \equiv \sqrt{\frac{2 \left(\sqrt{1 + (Q_{55}\alpha)^2} - Q_{55}\alpha \right) (1 + (Q_{55}\alpha)^2)}{Q_{55}\alpha}}. \quad (\text{A.16})$$

For weak attenuation, $\xi_Q \approx 1 + \frac{1}{2(Q_{55}\alpha)^2}$.

A.3 Isotropic Q matrix

Isotropic Q for the SH-wave propagation implies $Q_{55} = Q_{66}$. Taking into account that $\alpha = 1$, the imaginary part of equation (A.1) reduces to

$$k^2 - (k^I)^2 - 2Qkk^I = 0, \quad (\text{A.17})$$

Hence, for isotropic Q one finds

$$k^I = k(\sqrt{1 + Q^2} - Q), \quad (\text{A.18})$$

and

$$\xi_Q = \sqrt{\frac{2(\sqrt{1 + Q^2} - Q)(1 + Q^2)}{Q}}. \quad (\text{A.19})$$

Appendix B

Plane P- and SV-waves in attenuative VTI media

For P- and SV-waves, the Christoffel equation (2.6) can be written as

$$(\tilde{c}_{11}\tilde{k}_1^2 + \tilde{c}_{55}\tilde{k}_3^2 - \rho\omega^2)(\tilde{c}_{55}\tilde{k}_1^2 + \tilde{c}_{33}\tilde{k}_3^2 - \rho\omega^2) - [(\tilde{c}_{13} + \tilde{c}_{55})\tilde{k}_1\tilde{k}_3]^2 = 0. \quad (\text{B.1})$$

Analysis of the attenuation coefficients and phase velocities of P- and SV-waves in the limit of small attenuation and weak velocity and attenuation anisotropy shows that the inhomogeneity angle contributes only to second-order terms (see the analysis for SH-waves in Appendix A). Hence, the discussion here is limited to homogeneous P- and SV-wave propagation.

B.1 VTI Q-matrix

When the **Q**-matrix has VTI symmetry, equation (B.1) yields

$$\begin{aligned} & \{[(c_{11} + ic_{11}^I)\sin^2\theta + (c_{55} + ic_{55}^I)\cos^2\theta](k - ik^I)^2 - \rho\omega^2\} \\ & \{[(c_{55} + ic_{55}^I)\sin^2\theta + (c_{33} + ic_{33}^I)\cos^2\theta](k - ik^I)^2 - \rho\omega^2\} \\ & \{[(c_{13} + c_{55}) + i(c_{13}^I + c_{55}^I)]\sin\theta\cos\theta k k^I\}^2 = 0. \end{aligned} \quad (\text{B.2})$$

The real and the imaginary parts are given, respectively, by

$$\begin{aligned} & [(c_{11}\sin^2\theta + c_{55}\cos^2\theta)\mathcal{K}_1^a - \rho\omega^2][(c_{55}\sin^2\theta + c_{33}\cos^2\theta)\mathcal{K}_1^b - \rho\omega^2] \\ & - (c_{11}\sin^2\theta + c_{55}\cos^2\theta)(c_{55}\sin^2\theta + c_{33}\cos^2\theta)\mathcal{K}_2^a\mathcal{K}_2^b \\ & - (c_{13} + c_{55})^2\sin^2\theta\cos^2\theta[(\mathcal{K}_1^c)^2 - (\mathcal{K}_2^c)^2] = 0, \end{aligned} \quad (\text{B.3})$$

and

$$\begin{aligned} & (c_{11}\sin^2\theta + c_{55}\cos^2\theta)\mathcal{K}_2^a[(c_{55}\sin^2\theta + c_{33}\cos^2\theta)\mathcal{K}_1^b - \rho\omega^2] + \\ & (c_{55}\sin^2\theta + c_{33}\cos^2\theta)\mathcal{K}_2^b[(c_{11}\sin^2\theta + c_{55}\cos^2\theta)\mathcal{K}_1^a - \rho\omega^2] \\ & - (c_{13} + c_{55})^2\sin^2\theta\cos^2\theta 2\mathcal{K}_1^c\mathcal{K}_2^c = 0, \end{aligned} \quad (\text{B.4})$$

where

$$\begin{aligned}\mathcal{K}_1^a &= \mathcal{K}_1 + \frac{\Delta^a}{Q_{33}} 2kk^I, \quad \mathcal{K}_2^a = \mathcal{K}_2 - \frac{\Delta^a}{Q_{33}} [k^2 - (k^I)^2], \\ \mathcal{K}_1^b &= \mathcal{K}_1 + \frac{\Delta^b}{Q_{33}} 2kk^I, \quad \mathcal{K}_2^b = \mathcal{K}_2 - \frac{\Delta^b}{Q_{33}} [k^2 - (k^I)^2], \\ \mathcal{K}_1^c &= \mathcal{K}_1 + \frac{\Delta^c}{Q_{33}} 2kk^I, \quad \mathcal{K}_2^c = \mathcal{K}_2 - \frac{\Delta^c}{Q_{33}} [k^2 - (k^I)^2],\end{aligned}\tag{B.5}$$

$$\mathcal{K}_1 = k^2 - (k^I)^2 + \frac{2kk^I}{Q_{33}},\tag{B.6}$$

$$\mathcal{K}_2 = \frac{1}{Q_{33}} [k^2 - (k^I)^2] - 2kk^I,\tag{B.7}$$

and

$$\begin{aligned}\Delta^a &= \frac{c_{11} \sin^2 \theta}{c_{11} \sin^2 \theta + c_{55} \cos^2 \theta} \frac{Q_{33} - Q_{11}}{Q_{11}} + \frac{c_{55} \cos^2 \theta}{c_{11} \sin^2 \theta + c_{55} \cos^2 \theta} \frac{Q_{33} - Q_{55}}{Q_{55}}, \\ \Delta^b &= \frac{c_{55} \sin^2 \theta}{c_{55} \sin^2 \theta + c_{33} \cos^2 \theta} \frac{Q_{33} - Q_{55}}{Q_{55}}, \\ \Delta^c &= \frac{c_{13}}{c_{13} + c_{55}} \frac{Q_{33} - Q_{13}}{Q_{13}} + \frac{c_{55}}{c_{13} + c_{55}} \frac{Q_{33} - Q_{55}}{Q_{55}}.\end{aligned}\tag{B.8}$$

Using equation (B.4), we find

$$\mathcal{K}_2 = -\frac{A\Delta^a + B\Delta^b - C\Delta^c [k^2 - (k^I)^2]}{A + B - C} \frac{1}{Q_{33}},\tag{B.9}$$

where

$$\begin{aligned}A &= (c_{11} \sin^2 \theta + c_{55} \cos^2 \theta) [(c_{55} \sin^2 \theta + c_{33} \cos^2 \theta) \mathcal{K}_1^b - \rho\omega^2], \\ B &= (c_{55} \sin^2 \theta + c_{33} \cos^2 \theta) [(c_{11} \sin^2 \theta + c_{55} \cos^2 \theta) \mathcal{K}_1^a - \rho\omega^2], \\ C &= 2(c_{13} + c_{55})^2 \sin^2 \theta \cos^2 \theta \mathcal{K}_1^c.\end{aligned}\tag{B.10}$$

Equations (B.7) and (B.9) can be combined to solve for the normalized attenuation coefficient $\mathcal{A} \equiv k^I/k$. As shown in Appendix C, equation (B.9) can be simplified by assuming weak attenuation and weak attenuation anisotropy.

B.2 Special case: $Q_{ij} \equiv Q$

For the special case of identical Q components, $\frac{c_{11}}{c_{11}^I} = \frac{c_{33}}{c_{33}^I} = \frac{c_{13}}{c_{13}^I} = \frac{c_{55}}{c_{55}^I} = Q$, equation (B.1) becomes

$$\begin{aligned} & [(c_{11} \sin^2 \theta + c_{55} \cos^2 \theta) \mathcal{K}_1 - \rho \omega^2 + i(c_{11} \sin^2 \theta + c_{55} \cos^2 \theta) \mathcal{K}_2] \cdot \\ & [(c_{55} \sin^2 \theta + c_{33} \cos^2 \theta) \mathcal{K}_1 - \rho \omega^2 + i(c_{55} \sin^2 \theta + c_{33} \cos^2 \theta) \mathcal{K}_2] \\ & - [(c_{13} + c_{55}) \sin \theta \cos \theta (\mathcal{K}_1 + i \mathcal{K}_2)]^2 = 0, \end{aligned} \quad (\text{B.11})$$

where \mathcal{K}_1 and \mathcal{K}_2 are defined in equations (B.6) and (B.7) with Q_{33} replaced by Q .

The only physically meaningful solution of the imaginary part of equation (B.11) is $\mathcal{K}_2 = 0$, which then yields the same isotropic expression for k^I as that in equation (A.18).

Solving the real part of equation (B.11), I obtain the phase velocities in the form

$$V_{\{P,SV\}} = \xi_Q V_{\{P,SV\}}^{\text{elast}}, \quad (\text{B.12})$$

where ξ_Q is given in equation (A.19), and $V_{\{P,SV\}}^{\text{elast}}$ is the P- or SV-wave phase velocity in the reference purely-elastic VTI medium:

$$\begin{aligned} V_{\{P,SV\}}^{\text{elast}} &= \frac{1}{\sqrt{2\rho}} \left\{ (c_{11} + c_{55}) \sin^2 \theta + (c_{33} + c_{55}) \cos^2 \theta \right. \\ &\quad \left. \pm \sqrt{[(c_{11} - c_{55}) \sin^2 \theta - (c_{33} - c_{55}) \cos^2 \theta]^2 + 4(c_{13} + c_{55})^2 \sin^2 \theta \cos^2 \theta} \right\}^{1/2}. \end{aligned} \quad (\text{B.13})$$

Appendix C

Approximate solutions for weak attenuation and weak attenuation anisotropy

Here I simplify the attenuation coefficient derived in Appendix B for homogeneous wave propagation under the assumption of weak attenuation and weak attenuation anisotropy.

C.0.1 Attenuation coefficients for P- and SV-waves

For weak attenuation ($k^I \ll k$), the term $(k^I)^2$ in the difference $k^2 - (k^I)^2$ can be dropped. If the attenuation anisotropy is weak, then the fractional difference between the P-wave attenuation coefficients in the horizontal and vertical directions is small, and $\left| \frac{Q_{33} - Q_{11}}{Q_{11}} \right| \ll 1$. When Q_{33} and Q_{55} are comparable (a common case), the assumption of weak attenuation anisotropy implies that Q_{13} is comparable to (i.e., of the same order as) Q_{33} and Q_{55} . This follows from the definition of the parameter δ_Q . Hence, the magnitude of the terms Δ^a , Δ^b , and Δ^c in equation (B.8) is not much larger than unity. Then the terms $\frac{\Delta^a}{Q_{33}} 2kk^I$, $\frac{\Delta^b}{Q_{33}} 2kk^I$, and $\frac{\Delta^c}{Q_{33}} 2kk^I$ in equations (B.5) are of the second order compared to k^2 , and $\mathcal{K}_1^a \approx \mathcal{K}_1^b \approx \mathcal{K}_1^c \approx \mathcal{K}_1$. It follows from equation (B.6) that for weak attenuation $\mathcal{K}_1 \approx k^2$, which helps to represent equations (B.10) as

$$\begin{aligned} A &= (c_{11} \sin^2 \theta + c_{55} \cos^2 \theta)[(c_{55} \sin^2 \theta + c_{33} \cos^2 \theta) k^2 - \rho\omega^2], \\ B &= (c_{55} \sin^2 \theta + c_{33} \cos^2 \theta)[(c_{11} \sin^2 \theta + c_{55} \cos^2 \theta) k^2 - \rho\omega^2], \\ C &= 2(c_{13} + c_{55})^2 \sin^2 \theta \cos^2 \theta k^2. \end{aligned} \quad (\text{C.1})$$

Combining equations (B.7) and (B.9) in the limit of weak attenuation gives

$$k^2 - 2Q_{33}kk^I = -\frac{A\Delta^a + B\Delta^b - C\Delta^c}{A + B - C} k^2. \quad (\text{C.2})$$

Substituting equations (C.1) into equation (C.2) yields

$$\mathcal{A} = \frac{1}{2Q_{33}}(1 + \mathcal{H}), \quad (\text{C.3})$$

where

$$\mathcal{H} \equiv \frac{A\Delta^a + B\Delta^b - C\Delta^c}{A + B - C}. \quad (\text{C.4})$$

C.0.2 Parameter δ_Q

The attenuation-anisotropy parameter δ_Q is defined through the second derivative of the normalized P-wave attenuation coefficient \mathcal{A}_P with respect to the phase angle θ at vertical incidence:

$$\left. \frac{d^2 \mathcal{A}_P}{d\theta^2} \right|_{\theta=0} = 2 \mathcal{A}_{P0} \delta_Q. \quad (\text{C.5})$$

Substitution of \mathcal{A}_P from equation (C.3) leads to the following expression for δ_Q under the assumption of weak attenuation and weak attenuation anisotropy:

$$\delta_Q = \frac{1}{2} \left. \frac{d^2 \mathcal{H}}{d\theta^2} \right|_{\theta=0}. \quad (\text{C.6})$$

By evaluating $\left. \frac{d^2 \mathcal{H}}{d\theta^2} \right|_{\theta=0}$ and taking into account that for P-waves $\mathcal{H}|_{\theta=0} = 0$ and $\left. \frac{\partial \mathcal{H}}{\partial \theta} \right|_{\theta=0} = 0$, one obtains

$$\delta_Q = \frac{\frac{Q_{33} - Q_{55}}{Q_{55}} c_{55} \frac{(c_{13} + c_{33})^2}{(c_{33} - c_{55})} + 2 \frac{Q_{33} - Q_{13}}{Q_{13}} c_{13} (c_{13} + c_{55})}{c_{33} (c_{33} - c_{55})}. \quad (\text{C.7})$$

Appendix D

Isotropic conditions for the attenuation coefficient k^I

In the main text of Chapter 2, I discuss the conditions needed to make the *normalized* attenuation coefficient \mathcal{A} isotropic (independent of angle). For completeness, here I introduce the isotropic conditions for the imaginary wavenumber (attenuation coefficient) k^I . The attenuation and velocity anisotropy, as well as the attenuation itself, are assumed to be weak.

D.0.3 SH-wave

The SH-wave attenuation coefficient can be approximated by substituting the SH-wave phase velocity V_{SH} as a function of the phase angle θ into equation (2.27):

$$k_{SH}^I = \frac{\omega}{V_{SH}(\theta)} \mathcal{A}_{SH} = \frac{\omega}{2Q_{55}V_{S0}} \frac{1 + \gamma_Q \sin^2 \theta}{\sqrt{1 + 2\gamma \sin^2 \theta}}, \quad (\text{D.1})$$

where ω is the angular frequency and V_{S0} is the shear-wave velocity along the symmetry axis. If $|\gamma| \ll 1$, equation (D.1) simplifies to

$$k_{SH}^I = \frac{\omega}{2Q_{55}V_{S0}} [1 + (\gamma_Q - \gamma) \sin^2 \theta]. \quad (\text{D.2})$$

The coefficient k_{SH}^I is independent of angle only if

$$\gamma = \gamma_Q. \quad (\text{D.3})$$

D.0.4 P-SV waves

Using the linearized phase-velocity functions (Thomsen, 1986), the P- and SV-wave attenuation coefficients can be obtained from equations (2.36) and (2.41) as

$$k_P^I = \frac{\omega}{V_P(\theta)} \mathcal{A}_P = \frac{\omega}{2Q_{33}V_{P0}} \frac{1 + \delta_Q \sin^2 \theta \cos^2 \theta + \epsilon_Q \sin^4 \theta}{1 + \delta \sin^2 \theta \cos^2 \theta + \epsilon \sin^4 \theta}, \quad (\text{D.4})$$

$$k_{SV}^I = \frac{\omega}{V_{SV}(\theta)} \mathcal{A}_{SV} = \frac{\omega}{2Q_{55}V_{S0}} \frac{1 + \sigma_Q \sin^2 \theta}{1 + \sigma \sin^2 \theta}. \quad (\text{D.5})$$

The coefficient k_P^I becomes isotropic if

$$\epsilon = \epsilon_Q \quad \text{and} \quad \delta = \delta_Q . \quad (\text{D.6})$$

Isotropic k_{SV}^I requires that

$$\sigma = \sigma_Q . \quad (\text{D.7})$$

Both k_P^I and k_{SV}^I are independent of angle if the anisotropic parameters satisfy equation (D.6) and, as follows from equation (2.42),

$$g_Q \equiv \frac{Q_{33}}{Q_{55}} = 1 . \quad (\text{D.8})$$

Therefore, unlike the *normalized* attenuation coefficient, the imaginary wavenumber k^I does not necessarily become isotropic even if all elements Q_{ij} are identical (then $\epsilon_Q = \delta_Q = 0$ and $g_Q = 1$). From equation (D.6), an additional condition required in this case is the absence of velocity anisotropy for P- and SV-waves ($\epsilon = \delta = 0$).

Appendix E

Approximate attenuation outside the symmetry planes of orthorhombic media

The complex Christoffel equation 3.2 for homogeneous wave propagation outside the symmetry planes can be rewritten as

$$\begin{aligned}
& [(c_{11}n_1^2 + c_{66}n_2^2 + c_{55}n_3^2)\mathcal{K}_{1,(1,6,5)} - \rho V^2 + i(c_{11}n_1^2 + c_{66}n_2^2 + c_{55}n_3^2)\mathcal{K}_{2,(1,6,5)}] \\
& \cdot \{ [(c_{66}n_1^2 + c_{22}n_2^2 + c_{44}n_3^2)\mathcal{K}_{1,(6,2,4)} - \rho V^2 + i(c_{66}n_1^2 + c_{22}n_2^2 + c_{44}n_3^2)\mathcal{K}_{2,(6,2,4)}] \\
& \cdot [(c_{55}n_1^2 + c_{44}n_2^2 + c_{33}n_3^2)\mathcal{K}_{1,(5,4,3)} - \rho V^2 + i(c_{55}n_1^2 + c_{44}n_2^2 + c_{33}n_3^2)\mathcal{K}_{2,(5,4,3)}] \\
& - [(c_{23} + c_{44})n_2n_3(\mathcal{K}_{1,(23,44)} + i\mathcal{K}_{2,(23,44)})]^2 \} \\
& - [(c_{12} + c_{66})n_1n_2(\mathcal{K}_{1,(12,66)} + i\mathcal{K}_{2,(12,66)})] \\
& \cdot \{ [(c_{12} + c_{66})n_1n_2(\mathcal{K}_{1,(12,66)} + i\mathcal{K}_{2,(12,66)})] \\
& \cdot [(c_{55}n_1^2 + c_{44}n_2^2 + c_{33}n_3^2)\mathcal{K}_{1,(5,4,3)} - \rho V^2 + i(c_{55}n_1^2 + c_{44}n_2^2 + c_{33}n_3^2)\mathcal{K}_{2,(5,4,3)}] - \\
& [(c_{13} + c_{55})n_1n_3(\mathcal{K}_{1,(13,55)} + i\mathcal{K}_{2,(13,55)})] \cdot [(c_{23} + c_{44})n_2n_3(\mathcal{K}_{1,(23,44)} + i\mathcal{K}_{2,(23,44)})] \} \\
& + [(c_{13} + c_{55})n_1n_3(\mathcal{K}_{1,(13,55)} + i\mathcal{K}_{2,(13,55)})] \\
& \cdot \{ [(c_{12} + c_{66})n_1n_2(\mathcal{K}_{1,(12,66)} + i\mathcal{K}_{2,(12,66)})] \cdot [(c_{23} + c_{44})n_2n_3(\mathcal{K}_{1,(23,44)} + i\mathcal{K}_{2,(23,44)})] \\
& - [(c_{13} + c_{55})n_1n_3(\mathcal{K}_{1,(13,55)} + i\mathcal{K}_{2,(13,55)})] \\
& [(c_{66}n_1^2 + c_{22}n_2^2 + c_{44}n_3^2)\mathcal{K}_{1,(6,2,4)} - \rho V^2 + i(c_{66}n_1^2 + c_{22}n_2^2 + c_{44}n_3^2)\mathcal{K}_{2,(6,2,4)}] \} = 0,
\end{aligned} \tag{E.1}$$

where

$$\begin{aligned}
\mathcal{K}_1 &= 1 - \mathcal{A}^2 + \frac{2}{Q_{33}}\mathcal{A}, & \mathcal{K}_2 &= \frac{1 - \mathcal{A}^2}{Q_{33}} - 2\mathcal{A}, \\
\mathcal{K}_{1,(i,j,l)} &= \mathcal{K}_1 + 2\frac{\Delta_{(i,j,l)}}{Q_{33}}\mathcal{A}, & \mathcal{K}_{2,(i,j,l)} &= \mathcal{K}_2 + \frac{\Delta_{(i,j,l)}}{Q_{33}}(1 - \mathcal{A}^2), \\
\mathcal{K}_{1,(ij,kl)} &= \mathcal{K}_1 + 2\frac{\Delta_{(ij,kl)}}{Q_{33}}\mathcal{A}, & \mathcal{K}_{2,(ij,kl)} &= \mathcal{K}_2 + \frac{\Delta_{(ij,kl)}}{Q_{33}}(1 - \mathcal{A}^2), \\
\Delta_{(i,j,l)} &= \frac{c_{ii}n_1^2 \frac{Q_{33} - Q_{ii}}{Q_{ii}} + c_{jj}n_2^2 \frac{Q_{33} - Q_{jj}}{Q_{jj}} + c_{ll}n_3^2 \frac{Q_{33} - Q_{ll}}{Q_{ll}}}{c_{ii}n_1^2 + c_{jj}n_2^2 + c_{ll}n_3^2},
\end{aligned}$$

and

$$\Delta_{(ij,kl)} = \frac{c_{ij} \frac{Q_{33} - Q_{ij}}{Q_{ij}} + c_{kl} \frac{Q_{33} - Q_{kl}}{Q_{kl}}}{c_{ij} + c_{kl}}.$$

Note that $\mathcal{A} \equiv k^I/k$ is on the order of the inverse Q -factor ($1/Q$). When the attenuation is weak ($\mathcal{A} \ll 1$), one obtains $\mathcal{K}_1 \approx 1$ and $\mathcal{K}_2 \approx \frac{1}{Q_{33}} - 2\mathcal{A}$ by dropping the quadratic and higher-order terms in \mathcal{A} (i.e., in $1/Q$). Assuming that Q_{33} and Q_{55} are of the same order (the common case), weak attenuation anisotropy implies the same order for all components Q_{ij} . Hence, the magnitude of the terms $\Delta_{(i,j,l)}$ and $\Delta_{(ij,kl)}$ cannot be much larger than unity. Then the terms $\frac{\Delta_{(i,j,l)}}{Q_{33}}\mathcal{A}$, $\frac{\Delta_{(ij,kl)}}{Q_{33}}\mathcal{A}$, $\frac{\Delta_{(i,j,l)}}{Q_{33}}\mathcal{A}^2$, and $\frac{\Delta_{(ij,kl)}}{Q_{33}}\mathcal{A}^2$ are either quadratic or cubic in \mathcal{A} . Dropping these terms yields $\mathcal{K}_{1,(i,j,l)} \approx 1$, $\mathcal{K}_{2,(i,j,l)} \approx \frac{1 + \Delta_{(i,j,l)}}{Q_{33}} - 2\mathcal{A}$, $\mathcal{K}_{1,(ij,kl)} \approx 1$, and $\mathcal{K}_{2,(ij,kl)} \approx \frac{1 + \Delta_{(ij,kl)}}{Q_{33}} - 2\mathcal{A}$.

Next, I denote $\mathcal{C}_{(i,j,l)} = c_{ii}n_1^2 + c_{jj}n_2^2 + c_{ll}n_3^2$ and $\mathcal{C}_{(ij,kl)} = (c_{ij} + c_{kl})n_i n_j$ and simplify equation E.1 for weak attenuation and weak attenuation anisotropy as

$$\begin{aligned} & \left[\mathcal{C}_{(1,6,5)} - \rho V^2 + i\mathcal{C}_{(1,6,5)} \left(\frac{1 + \Delta_{(1,6,5)}}{Q_{33}} - 2\mathcal{A} \right) \right] \\ & \cdot \left\{ \left[\mathcal{C}_{(6,2,4)} - \rho V^2 + i\mathcal{C}_{(6,2,4)} \left(\frac{1 + \Delta_{(6,2,4)}}{Q_{33}} - 2\mathcal{A} \right) \right] \right. \\ & \cdot \left[\mathcal{C}_{(5,4,3)} - \rho V^2 + i\mathcal{C}_{(5,4,3)} \left(\frac{1 + \Delta_{(5,4,3)}}{Q_{33}} - 2\mathcal{A} \right) \right] \\ & \left. - \mathcal{C}_{(23,44)}^2 \left[1 + i \left(\frac{1 + \Delta_{(23,44)}}{Q_{33}} - 2\mathcal{A} \right) \right]^2 \right\} \\ & - \mathcal{C}_{(12,66)} \left[1 + \left(\frac{1 + \Delta_{(12,66)}}{Q_{33}} - 2\mathcal{A} \right) \right] \\ & \cdot \left\{ \mathcal{C}_{(12,66)} \left[1 + \left(\frac{1 + \Delta_{(12,66)}}{Q_{33}} - 2\mathcal{A} \right) \right] \cdot \left[\mathcal{C}_{(5,4,3)} - \rho V^2 + i\mathcal{C}_{(5,4,3)} \left(\frac{1 + \Delta_{(5,4,3)}}{Q_{33}} - 2\mathcal{A} \right) \right] \right. \\ & - \mathcal{C}_{(13,55)} \left[1 + \left(\frac{1 + \Delta_{(13,55)}}{Q_{33}} - 2\mathcal{A} \right) \right] \cdot \mathcal{C}_{(23,44)} \left[1 + i \left(\frac{1 + \Delta_{(23,44)}}{Q_{33}} - 2\mathcal{A} \right) \right] \left. \right\} \\ & + \mathcal{C}_{(13,55)} \left[1 + i \left(\frac{1 + \Delta_{(13,55)}}{Q_{33}} - 2\mathcal{A} \right) \right] \\ & \cdot \left\{ \mathcal{C}_{(12,66)} \left[1 + i \left(\frac{1 + \Delta_{(12,66)}}{Q_{33}} - 2\mathcal{A} \right) \right] \cdot \mathcal{C}_{(23,44)} \left[1 + i \left(\frac{1 + \Delta_{(23,44)}}{Q_{33}} - 2\mathcal{A} \right) \right] - \right. \\ & \left. \mathcal{C}_{(13,55)} \left[1 + i \left(\frac{1 + \Delta_{(13,55)}}{Q_{33}} - 2\mathcal{A} \right) \right] \cdot \left[\mathcal{C}_{(6,2,4)} - \rho V^2 + i\mathcal{C}_{(6,2,4)} \left(\frac{1 + \Delta_{(6,2,4)}}{Q_{33}} - 2\mathcal{A} \right) \right] \right\} \\ & = 0. \end{aligned} \tag{E.2}$$

The real part of equation (A-2) is

$$\begin{aligned}
& (c_{11}n_1^2 + c_{66}n_2^2 + c_{55}n_3^2 - \rho V^2) \\
& \cdot [(c_{66}n_1^2 + c_{22}n_2^2 + c_{44}n_3^2 - \rho V^2)(c_{55}n_1^2 + c_{44}n_2^2 + c_{33}n_3^2 - \rho V^2) - (c_{23} + c_{44})^2 n_2^2 n_3^2] \\
& - (c_{12} + c_{66})n_1 n_2 \\
& \cdot [(c_{12} + c_{66})n_1 n_2 (c_{55}n_1^2 + c_{44}n_2^2 + c_{33}n_3^2 - \rho V^2) - (c_{13} + c_{55})(c_{23} + c_{44})n_1 n_2 n_3^2] \\
& + (c_{13} + c_{55})n_1 n_3 \\
& \cdot [(c_{12} + c_{66})(c_{23} + c_{44})n_1 n_2 n_3^2 - (c_{13} + c_{55})n_1 n_3 (c_{66}n_1^2 + c_{22}n_2^2 + c_{44}n_3^2 - \rho V^2)] = 0,
\end{aligned} \tag{E.3}$$

which is identical to the Christoffel equation for the reference nonattenuative medium.

The normalized attenuation coefficient \mathcal{A} is obtained from the imaginary part of equation E.2:

$$\mathcal{A} = \frac{1}{2Q_{33}} \left(1 + \frac{\mathcal{H}_u}{\mathcal{H}_d} \right), \tag{E.4}$$

where

$$\begin{aligned}
\mathcal{H}_u = & \Delta_{(1,6,5)} \mathcal{C}_{(1,6,5)} \left[(\mathcal{C}_{(6,2,4)} - \rho V^2)(\mathcal{C}_{(5,4,3)} - \rho V^2) - \mathcal{C}_{(23,44)}^2 \right] \\
& + \Delta_{(6,2,4)} \mathcal{C}_{(6,2,4)} \left[(\mathcal{C}_{(1,6,5)} - \rho V^2)(\mathcal{C}_{(5,4,3)} - \rho V^2) - \mathcal{C}_{(13,55)}^2 \right] \\
& + \Delta_{(5,4,3)} \mathcal{C}_{(5,4,3)} \left[(\mathcal{C}_{(1,6,5)} - \rho V^2)(\mathcal{C}_{(6,2,4)} - \rho V^2) - \mathcal{C}_{(12,66)}^2 \right] \\
& - 2\Delta_{(13,55)} \mathcal{C}_{(13,55)}^2 (\mathcal{C}_{(6,2,4)} - \rho V^2) - 2\Delta_{(12,66)} \mathcal{C}_{(12,66)}^2 (\mathcal{C}_{(5,4,3)} - \rho V^2) \\
& - 2\Delta_{(23,44)} \mathcal{C}_{(23,44)}^2 (\mathcal{C}_{(1,6,5)} - \rho V^2) \\
& + 2(\Delta_{(13,55)} + \Delta_{(12,66)} + \Delta_{(23,44)}) \mathcal{C}_{(13,55)} \mathcal{C}_{(12,66)} \mathcal{C}_{(23,44)},
\end{aligned} \tag{E.5}$$

and

$$\begin{aligned}
\mathcal{H}_d = & \rho V^2 \left[(\mathcal{C}_{(1,6,5)} - \rho V^2)(\mathcal{C}_{(6,2,4)} - \rho V^2) + (\mathcal{C}_{(1,6,5)} - \rho V^2)(\mathcal{C}_{(5,4,3)} - \rho V^2) \right. \\
& \left. + (\mathcal{C}_{(6,2,4)} - \rho V^2)(\mathcal{C}_{(5,4,3)} - \rho V^2) - \mathcal{C}_{(12,66)}^2 - \mathcal{C}_{(13,55)}^2 - \mathcal{C}_{(23,44)}^2 \right].
\end{aligned} \tag{E.6}$$

The term $\frac{\mathcal{H}_u}{\mathcal{H}_d}$ in equation E.4 can be expressed through the velocity- and attenuation-anisotropy parameters. Assuming that the anisotropy is weak for both velocity and attenuation, I drop the quadratic and higher-order terms in all anisotropy parameters to obtain

$$\mathcal{H}_u = c_{33}(c_{33} - c_{55})^2 \left[\epsilon_Q^{(2)} n_1^4 + \epsilon_Q^{(1)} n_2^4 + (2\epsilon_Q^{(2)} + \delta_Q^{(3)}) n_1^2 n_2^2 + \delta_Q^{(2)} n_1^2 n_3^2 + \delta_Q^{(1)} n_2^2 n_3^2 \right],$$

$$\begin{aligned}
\mathcal{H}_d = & c_{33}(c_{33} - c_{55}) \\
& \cdot \left\{ (c_{33} - c_{55})(1 + 2\epsilon^{(2)}n_1^4 + 2\epsilon^{(1)}n_2^4 + 2\delta^{(2)}n_1^2n_3^2 + 2\delta^{(1)}n_2^2n_3^2 + 4\epsilon^{(2)}n_1^2n_2^2 + 2\delta^{(3)}n_1^2n_2^2) \right. \\
& + c_{33} \left[\epsilon^{(1)}(-2n_2^2 + 6n_2^4) + \epsilon^{(2)}(-2n_1^2 + 6n_1^4 + 12n_1^2n_2^2) \right. \\
& \quad \left. \left. + 6\delta^{(1)}n_2^2n_3^2 + 6\delta^{(2)}n_1^2n_3^2 + 6\delta^{(3)}n_1^2n_2^2 \right] \right. \\
& \left. + c_{55} \left[\gamma^{(1)}(-2 - 2n_2^2) + \gamma^{(2)}(2 - 2n_1^2) \right] \right\} .
\end{aligned} \tag{E.7}$$

Note that since \mathcal{H}_u is linear in the anisotropy parameters, it is sufficient to keep just the isotropic part of \mathcal{H}_d . Substitution of equations A-7 and A-8 into equation A-4 yields the final form of the approximate P-wave attenuation coefficient given in the main text [equation 3.34].

Appendix F

Second-order approximation for the effective parameters of layered attenuative VTI media

Here I derive the second-order approximation for the effective velocity- and attenuation-anisotropy parameters for thin-layered media composed of an arbitrary number of VTI (in terms of both velocity and attenuation) constituents. In accordance with the main assumption of Backus averaging (see the main text), the thickness of each layer has to be much smaller than the predominant wavelength.

F.0.5 Anisotropy parameters for SH-waves

First, I consider the parameters γ and γ_Q , which control the velocity and attenuation anisotropy (respectively) for the SH-wave. The effective stiffness component \tilde{c}_{55} is given by (see equation 5.17)

$$\tilde{c}_{55} = \frac{1}{\sum_{k=1}^N \frac{\phi^{(k)}}{c_{55}^{(k)} (1 - i/Q_{55}^{(k)})}}, \quad (\text{F.1})$$

where $\phi^{(k)}$ denotes the volume fraction of the k -th constituent ($\sum_{k=1}^N \phi^{(k)} = 1$). In the weak-attenuation limit ($\frac{1}{Q_{55}} \ll 1$), \tilde{c}_{55} can be approximated as

$$\tilde{c}_{55} = \frac{\langle \frac{1}{c_{55}} \rangle - i \langle \frac{1}{c_{55} Q_{55}} \rangle}{\langle \frac{1}{c_{55}} \rangle^2}. \quad (\text{F.2})$$

From equation F.2 it follows that

$$c_{55} = \langle \frac{1}{c_{55}} \rangle^{-1}, \quad (\text{F.3})$$

and

$$Q_{55} = \left\langle \frac{1}{c_{55}} \right\rangle / \left\langle \frac{1}{c_{55} Q_{55}} \right\rangle. \quad (\text{F.4})$$

According to equation 5.18,

$$\tilde{c}_{66} = \langle c_{66} \rangle - i \left\langle \frac{c_{66}}{Q_{66}} \right\rangle, \quad (\text{F.5})$$

which yields

$$c_{66} = \langle c_{66} \rangle, \quad (\text{F.6})$$

and

$$Q_{66} = \langle c_{66} \rangle \left\langle \frac{c_{66}}{Q_{66}} \right\rangle. \quad (\text{F.7})$$

By dropping the cubic and higher-order terms in $\hat{\Delta}c_{55}^{(k)}$ and $\gamma^{(k)}$, I obtain the second-order approximation for the effective parameter γ :

$$\begin{aligned} \gamma = \langle \gamma \rangle + \frac{1}{2} & \left[\sum_{k=1}^N \phi^{(k)} \left(\hat{\Delta}c_{55}^{(k)} \right)^2 - \left(\sum_{k=1}^N \phi^{(k)} \hat{\Delta}c_{55}^{(k)} \right)^2 \right] \\ & + \left[\sum_{k=1}^N \phi^{(k)} \hat{\Delta}c_{55}^{(k)} \gamma^{(k)} - \sum_{k=1}^N \phi^{(k)} \hat{\Delta}c_{55}^{(k)} \sum_{k=1}^N \phi^{(k)} \gamma^{(k)} \right]. \end{aligned} \quad (\text{F.8})$$

Note that for any quantities x and y varying among different constituents, one has

$$\sum_{k=1}^N \phi^{(k)} x^{(k)} y^{(k)} - \sum_{k=1}^N \phi^{(k)} x^{(k)} \sum_{k=1}^N \phi^{(k)} y^{(k)} = \sum_{k=1}^N \sum_{l=k+1}^N \phi^{(k)} \phi^{(l)} \Delta x^{(k,l)} \Delta y^{(k,l)}, \quad (\text{F.9})$$

where $\Delta x^{(k,l)} = x^{(l)} - x^{(k)}$. Then γ can be represented as

$$\gamma = \langle \gamma \rangle + \gamma^{(\text{is})} + \gamma^{(\text{is-Van})} + \gamma^{(\text{Van})}, \quad (\text{F.10})$$

where

$$\langle \gamma \rangle = \sum_{k=1}^N \phi^{(k)} \gamma^{(k)}, \quad (\text{F.11})$$

$$\gamma^{(\text{is})} = \frac{1}{2} \sum_{k=1}^N \sum_{l=k+1}^N \phi^{(k)} \phi^{(l)} \left(\frac{\Delta c_{55}^{(k,l)}}{\bar{c}_{55}} \right)^2, \quad (\text{F.12})$$

$$\gamma^{(\text{is-Van})} = \sum_{k=1}^N \sum_{l=k+1}^N \phi^{(k)} \phi^{(l)} \frac{\Delta c_{55}^{(k,l)}}{\bar{c}_{55}} \Delta \gamma^{(k,l)}, \quad (\text{F.13})$$

$$\gamma^{(\text{Van})} = 0, \quad (\text{F.14})$$

where $\Delta^{(k,l)}$ denotes the difference between the medium properties of the k -th and l -th constituents. For example, $\Delta c_{55}^{(k,l)} = c_{55}^l - c_{55}^k$ and $\Delta \gamma^{(k,l)} = \gamma^l - \gamma^k$. Equations F.10-F.14 generalize equations 16-19 of Bakulin (2003) for layered media with an arbitrary number of constituents.

To obtain the second-order approximation for the effective attenuation-anisotropy parameter γ_Q , I substitute equations F.4 and F.7 into equation 5.25 and keep only the linear and quadratic terms in $\hat{\Delta} c_{55}^{(k)}$, $\hat{\Delta} Q_{55}^{(k)}$, $\gamma^{(k)}$, and $\gamma_Q^{(k)}$:

$$\gamma_Q = \langle \gamma_Q \rangle + \gamma_Q^{(\text{is})} + \gamma_Q^{(\text{is-Van})} + \gamma_Q^{(\text{is-Qan})} + \gamma_Q^{(\text{Van-Qan})}, \quad (\text{F.15})$$

where

$$\langle \gamma_Q \rangle = \sum_{k=1}^N \phi^{(k)} \gamma_Q^{(k)}, \quad (\text{F.16})$$

$$\gamma_Q^{(\text{is})} = -2 \sum_{k=1}^N \sum_{l=k+1}^N \phi^{(k)} \phi^{(l)} \frac{\Delta c_{55}^{(k,l)}}{\bar{c}_{55}} \frac{\Delta Q_{55}^{(k,l)}}{\bar{Q}_{55}}, \quad (\text{F.17})$$

$$\gamma_Q^{(\text{is-Van})} = -2 \sum_{k=1}^N \sum_{l=k+1}^N \phi^{(k)} \phi^{(l)} \frac{\Delta Q_{55}^{(k,l)}}{\bar{Q}_{55}} \Delta \gamma^{(k,l)}, \quad (\text{F.18})$$

$$\gamma_Q^{(\text{is-Qan})} = \sum_{k=1}^N \sum_{l=k+1}^N \phi^{(k)} \phi^{(l)} \left(\frac{\Delta c_{55}^{(k,l)}}{\bar{c}_{55}} - \frac{\Delta Q_{55}^{(k,l)}}{\bar{Q}_{55}} \right) \Delta \gamma_Q^{(k,l)}, \quad (\text{F.19})$$

$$\gamma_Q^{(\text{Van-Qan})} = 2 \sum_{k=1}^N \sum_{l=k+1}^N \phi^{(k)} \phi^{(l)} \Delta \gamma^{(k,l)} \Delta \gamma_Q^{(k,l)}. \quad (\text{F.20})$$

F.0.6 Anisotropy parameters for P- and SV-waves

In the weak-attenuation limit, equations 5.14–5.16 yield

$$\begin{aligned} \tilde{c}_{11} = & \sum_{k=1}^N \phi^{(k)} c_{11}^{(k)} (1 - i/Q_{11}^{(k)}) - \sum_{k=1}^N \phi^{(k)} (\xi^{(k)})^2 c_{33}^{(k)} \left[1 + \frac{i}{Q_{33}^{(k)}} (1 - 2\xi_Q^{(k)}) \right] \\ & + \frac{\sum_{k=1}^N \frac{\phi^{(k)}}{c_{33}^{(k)}} - i \sum_{k=1}^N \frac{\phi^{(k)}}{c_{33}^{(k)} Q_{33}^{(k)}}}{\left(\sum_{k=1}^N \frac{\phi^{(k)}}{c_{33}^{(k)}} \right)^2} \left\{ \sum_{k=1}^N \phi^{(k)} \xi^{(k)} \left[1 + \frac{i}{Q_{33}^{(k)}} (1 - \xi_Q^{(k)}) \right] \right\}^2, \end{aligned} \quad (\text{F.21})$$

$$\tilde{c}_{33} = \frac{\sum_{k=1}^N \frac{\phi^{(k)}}{c_{33}^{(k)}} - i \sum_{k=1}^N \frac{\phi^{(k)}}{c_{33}^{(k)} Q_{33}^{(k)}}}{\left(\sum_{k=1}^N \frac{\phi^{(k)}}{c_{33}^{(k)}} \right)^2}, \quad (\text{F.22})$$

and

$$\begin{aligned} \tilde{c}_{13} = & \frac{\sum_{k=1}^N \phi^{(k)} \xi^{(k)}}{\sum_{k=1}^N \frac{\phi^{(k)}}{c_{33}^{(k)}}} \\ & - \frac{i}{\sum_{k=1}^N \frac{\phi^{(k)}}{c_{33}^{(k)}}} \left[\frac{\sum_{k=1}^N \frac{\phi^{(k)}}{c_{33}^{(k)} Q_{33}^{(k)}}}{\sum_{k=1}^N \frac{\phi^{(k)}}{c_{33}^{(k)}}} \sum_{k=1}^N \phi^{(k)} \xi^{(k)} - \sum_{k=1}^N \phi^{(k)} \frac{\xi^{(k)}}{Q_{33}^{(k)}} (1 - \xi_Q^{(k)}) \right], \end{aligned} \quad (\text{F.23})$$

where $\xi \equiv c_{13}/c_{33}$ and $\xi_Q \equiv Q_{33}/Q_{13}$. Using equation 5.24, I then rewrite ξ_Q as

$$\xi_Q = 1 + \frac{(1-g)\delta_Q - g(g_Q - 1)(1 + \xi)^2/(1-g)}{2\xi(g + \xi)}, \quad (\text{F.24})$$

where $g \equiv \frac{c_{55}}{c_{33}}$ and $g_Q \equiv \frac{Q_{33}}{Q_{55}}$.

If the cubic and higher-order terms in δ are ignored, the second-order approximation

for ξ becomes

$$\xi = 1 - 2g + \delta - \frac{\delta^2}{2(1-g)}, \quad (\text{F.25})$$

or

$$\xi = -1 - \delta + \frac{\delta^2}{2(1-g)}, \quad (\text{F.26})$$

depending on the sign of c_{13} ; here, c_{13} is assumed to be positive (see equation F.25).

By keeping only the linear and quadratic terms in $\hat{\Delta}c_{33}^{(k)}$, $\hat{\Delta}c_{55}^{(k)}$, $\hat{\Delta}Q_{33}^{(k)}$, $\hat{\Delta}Q_{55}^{(k)}$, as well as in the interval velocity- and attenuation-anisotropy parameters for P- and SV-waves, one obtains the second-order approximations for the effective VTI parameters.

1. Parameter ϵ :

$$\epsilon = \langle \epsilon \rangle + \epsilon^{(\text{is})} + \epsilon^{(\text{is-Van})} + \epsilon^{(\text{Van})}, \quad (\text{F.27})$$

where

$$\langle \epsilon \rangle = \sum_{k=1}^N \phi^{(k)} \epsilon^{(k)}, \quad (\text{F.28})$$

$$\epsilon^{(\text{is})} = 2\bar{g} \sum_{k=1}^N \sum_{l=k+1}^N \phi^{(k)} \phi^{(l)} \left[\frac{\Delta c_{33}^{(k,l)}}{\bar{c}_{33}} \frac{\Delta c_{55}^{(k,l)}}{\bar{c}_{55}} - \bar{g} \left(\frac{\Delta c_{55}^{(k,l)}}{\bar{c}_{55}} \right)^2 \right], \quad (\text{F.29})$$

$$\epsilon^{(\text{is-Van})} = \sum_{k=1}^N \sum_{l=k+1}^N \phi^{(k)} \phi^{(l)} \frac{\Delta c_{33}^{(k,l)}}{\bar{c}_{33}} (\Delta \epsilon^{(k,l)} - \Delta \delta^{(k,l)}) + 2\bar{g} \frac{\Delta c_{55}^{(k,l)}}{\bar{c}_{55}} \Delta \delta^{(k,l)}, \quad (\text{F.30})$$

$$\epsilon^{(\text{Van})} = -\frac{1}{2} \sum_{k=1}^N \sum_{l=k+1}^N \phi^{(k)} \phi^{(l)} \left(\Delta \delta^{(k,l)} \right)^2, \quad (\text{F.31})$$

and $\bar{g} = \frac{\bar{c}_{55}}{\bar{c}_{33}}$.

2. Parameter δ :

$$\delta = \langle \delta \rangle + \delta^{(\text{is})} + \delta^{(\text{is-Van})} + \delta^{(\text{Van})}, \quad (\text{F.32})$$

where

$$\langle \delta \rangle = \sum_{k=1}^N \phi^{(k)} \delta^{(k)}, \quad (\text{F.33})$$

$$\delta^{(\text{is})} = 2\bar{g} \sum_{k=1}^N \sum_{l=k+1}^N \phi^{(k)} \phi^{(l)} \left(\frac{\Delta c_{33}^{(k,l)}}{\bar{c}_{33}} - \frac{\Delta c_{55}^{(k,l)}}{\bar{c}_{55}} \right) \frac{\Delta c_{55}^{(k,l)}}{\bar{c}_{55}}, \quad (\text{F.34})$$

$$\delta^{(\text{is-Van})} = 0, \quad (\text{F.35})$$

$$\delta^{(\text{Van})} = -\frac{1}{2} \sum_{k=1}^N \sum_{l=k+1}^N \phi^{(k)} \phi^{(l)} \frac{(\Delta \delta^{(k,l)})^2}{1 - \bar{g}}. \quad (\text{F.36})$$

As was the case for SH-waves, equations F.27-F.36 generalize equations 29-32 and 21-24 of Bakulin (2003) for multiconstituent layered media.

3. Parameter ϵ_Q :

$$\epsilon_Q = \langle \epsilon_Q \rangle + \epsilon_Q^{(\text{is})} + \epsilon_Q^{(\text{is-Van})} + \epsilon_Q^{(\text{is-Qan})} + \epsilon_Q^{(\text{Van-Qan})}, \quad (\text{F.37})$$

where

$$\langle \epsilon_Q \rangle = \sum_{k=1}^N \phi^{(k)} \epsilon_Q^{(k)}, \quad (\text{F.38})$$

$$\begin{aligned} \epsilon_Q^{(\text{is})} = & -4\bar{g} \sum_{k=1}^N \sum_{l=k+1}^N \phi^{(k)} \phi^{(l)} \left[(1 - \bar{g}_Q) \left(\frac{\Delta c_{33}^{(k,l)}}{\bar{c}_{33}} - 2\bar{g} \frac{\Delta c_{55}^{(k,l)}}{\bar{c}_{55}} \right) \frac{\Delta c_{55}^{(k,l)}}{\bar{c}_{55}} + \frac{\Delta c_{55}^{(k,l)}}{\bar{c}_{55}} \frac{\Delta Q_{33}^{(k,l)}}{Q_{33}} \right. \\ & \left. + \bar{g}_Q \left(\frac{\Delta c_{33}^{(k,l)}}{\bar{c}_{33}} - 2\bar{g} \frac{\Delta c_{55}^{(k,l)}}{\bar{c}_{55}} \right) \frac{\Delta Q_{55}^{(k,l)}}{Q_{55}} \right], \quad (\text{F.39}) \end{aligned}$$

$$\begin{aligned} \epsilon_Q^{(\text{is-Van})} = & 2 \sum_{k=1}^N \sum_{l=k+1}^N \phi^{(k)} \phi^{(l)} \left[-2\bar{g}(1 - \bar{g}_Q) \frac{\Delta c_{55}^{(k,l)}}{\bar{c}_{55}} \Delta \delta^{(k,l)} - 2\bar{g}\bar{g}_Q \frac{\Delta Q_{55}^{(k,l)}}{Q_{55}} \Delta \delta^{(k,l)} \right. \\ & \left. - \frac{\Delta Q_{33}^{(k,l)}}{Q_{33}} (\Delta \epsilon^{(k,l)} - \Delta \delta^{(k,l)}) \right], \quad (\text{F.40}) \end{aligned}$$

$$\begin{aligned} \epsilon_Q^{(\text{is-Qan})} = & \sum_{k=1}^N \sum_{l=k+1}^N \phi^{(k)} \phi^{(l)} \left[\frac{\Delta c_{33}^{(k,l)}}{\bar{c}_{33}} (\Delta \epsilon_Q^{(k,l)} - \Delta \delta_Q^{(k,l)}) - \frac{\Delta Q_{33}^{(k,l)}}{Q_{33}} \Delta \epsilon_Q^{(k,l)} \right. \\ & \left. + 2\bar{g} \frac{\Delta c_{55}^{(k,l)}}{\bar{c}_{55}} \Delta \delta_Q^{(k,l)} \right], \quad (\text{F.41}) \end{aligned}$$

$$\epsilon_Q^{(\text{Van-Qan})} = \sum_{k=1}^N \sum_{l=k+1}^N \phi^{(k)} \phi^{(l)} \left[2\Delta\epsilon^{(k,l)} \Delta\epsilon_Q^{(k,l)} - \Delta\delta^{(k,l)} \Delta\delta_Q^{(k,l)} \right]. \quad (\text{F.42})$$

4. Parameter δ_Q :

$$\delta_Q = \langle \delta_Q \rangle + \delta_Q^{(\text{is})} + \delta_Q^{(\text{is-Qan})} + \delta_Q^{(\text{Van-Qan})} + \delta_Q^{(\text{Van})}, \quad (\text{F.43})$$

where

$$\langle \delta_Q \rangle = \sum_{k=1}^N \phi^{(k)} \delta_Q^{(k)}, \quad (\text{F.44})$$

$$\begin{aligned} \delta_Q^{(\text{is})} = -4\bar{g} \sum_{k=1}^N \sum_{l=k+1}^N \phi^{(k)} \phi^{(l)} & \left[(1 - \bar{g}_Q) \left(\frac{\Delta c_{33}^{(k,l)}}{\bar{c}_{33}} - \frac{\Delta c_{55}^{(k,l)}}{\bar{c}_{55}} \right) \frac{\Delta c_{55}^{(k,l)}}{\bar{c}_{55}} + \frac{\Delta c_{55}^{(k,l)}}{\bar{c}_{55}} \frac{\Delta Q_{33}^{(k,l)}}{\bar{Q}_{33}} \right. \\ & \left. + \bar{g}_Q \left(\frac{\Delta c_{33}^{(k,l)}}{\bar{c}_{33}} - 2 \frac{\Delta c_{55}^{(k,l)}}{\bar{c}_{55}} \right) \frac{\Delta Q_{55}^{(k,l)}}{\bar{Q}_{55}} \right], \end{aligned} \quad (\text{F.45})$$

$$\delta_Q^{(\text{is-Qan})} = - \sum_{k=1}^N \sum_{l=k+1}^N \phi^{(k)} \phi^{(l)} \frac{\Delta Q_{33}^{(k,l)}}{\bar{Q}_{33}} \Delta\delta_Q^{(k,l)}, \quad (\text{F.46})$$

$$\delta_Q^{(\text{Van-Qan})} = - \frac{1}{1 - \bar{g}} \sum_{k=1}^N \sum_{l=k+1}^N \phi^{(k)} \phi^{(l)} \Delta\delta^{(k,l)} \Delta\delta_Q^{(k,l)}, \quad (\text{F.47})$$

$$\delta_Q^{(\text{Van})} = \bar{g} \frac{1 - \bar{g}_Q}{(1 - \bar{g})^2} \sum_{k=1}^N \sum_{l=k+1}^N \phi^{(k)} \phi^{(l)} (\Delta\delta^{(k,l)})^2, \quad (\text{F.48})$$

where $\bar{g}_Q = \frac{\bar{Q}_{33}}{\bar{Q}_{55}}$.

Appendix G

Radiation patterns for 2D attenuative anisotropic media

Here I derive an asymptotic solution for far-field radiation patterns in 2D attenuative anisotropic media using the steepest-descent method. The wave equation in the frequency-wavenumber domain can be written for wave propagation in the $[x_1, x_3]$ -plane as

$$(\tilde{c}_{ijkl}k_jk_l - \rho\omega^2\delta_{ik})\tilde{u}_k(\omega, k) = \tilde{f}_i(\omega), \quad (\text{G.1})$$

where k_j are the wavenumber components, ρ is the density, ω is the angular frequency, and $i, j, k, l = 1, 3$. $\tilde{u}_k(\omega, k)$ denotes the spectrum of the k -th component of the particle displacement in the frequency-wavenumber domain, $\tilde{c}_{ijkl} = c_{ijkl} - ic_{ijkl}^I$ are the complex stiffness coefficients, and $\tilde{f}_i(\omega)$ is the spectrum of the i -th component of the line source function (i.e., independent of x_2).

The spectrum of the particle displacement is given by

$$\tilde{u}_k(\omega, \mathbf{x}) = \frac{1}{(2\pi)^2} \int_{-\infty}^{\infty} \int_{-\infty}^{\infty} \frac{\tilde{f}_i(\omega)}{\tilde{c}_{ijkl}k_jk_l - \rho\omega^2\delta_{ik}} e^{i(k_1x_1 + k_3x_3)} dk_1 dk_3. \quad (\text{G.2})$$

The integral G.2 can be represented in polar coordinates by using

$$p_1 = p \sin \theta; \quad p_3 = p \cos \theta, \quad (\text{G.3})$$

where $p = \frac{k}{\omega}$ is the slowness and θ is the polar angle:

$$\tilde{u}_k(\omega, \mathbf{x}) = \frac{1}{(2\pi)^2} \int_{-\infty}^{\infty} \int_0^{2\pi} \frac{p\tilde{f}_i(\omega)}{\tilde{c}_{ijkl}p^2n_jn_l - \rho\delta_{ik}} e^{i\omega p(x_1 \sin \theta + x_3 \cos \theta)} dp d\theta; \quad (\text{G.4})$$

$n_1 = \sin \theta$ and $n_3 = \cos \theta$.

Next, I apply the steepest-descent method to evaluate the integral over the slowness p . Two complex poles of the integrand correspond to the solution of the Christoffel equation:

$$\tilde{c}_{ijkl}p^2n_jn_l - \rho\delta_{ik} = 0. \quad (\text{G.5})$$

The term $\frac{p\tilde{f}_i(\omega)}{\tilde{c}_{ijkl}p^2n_jn_l - \rho\delta_{ik}}$ in equation G.4 can be expanded in a Laurent series in terms

of the slowness p , which helps to find the residue at the pole (namely, complex slowness \tilde{p}_s). Equation G.4 then takes the form

$$\tilde{u}_k(\omega, \mathbf{x}) = \frac{i}{2\pi} \int_0^{2\pi} \tilde{U}_k e^{i\omega\tilde{p}_s(x_1 \sin\theta + x_3 \cos\theta)} d\theta, \quad (\text{G.6})$$

where \tilde{U}_k is the residue associated with a certain wave mode (P , S_1 , or S_2).

The saddle-point condition corresponds to setting the derivative of the phase function to zero:

$$\left. \frac{d[\tilde{p}_s(x_1 \sin\theta + x_3 \cos\theta)]}{d\theta} \right|_{\theta=\tilde{\theta}_s} = 0, \quad (\text{G.7})$$

or

$$\tan \tilde{\theta}_s = \frac{x_1}{x_3} + \left. \frac{d\tilde{p}_s}{d\theta} \right|_{\theta=\tilde{\theta}_s} \frac{\tilde{V}_s}{x_3 \cos \tilde{\theta}_s} (x_1 \sin \tilde{\theta}_s + x_3 \cos \tilde{\theta}_s), \quad (\text{G.8})$$

where $\tilde{V}_s = \frac{1}{\tilde{p}_s}$, and \tilde{p}_s is obtained from the Christoffel equation at the saddle point $\tilde{\theta}_s$ (both \tilde{p}_s and $\tilde{\theta}_s$ are complex). At the pole for p and the saddle point for θ , the slowness components (equation G.3) are

$$\tilde{p}_1 = \tilde{p}_s \sin \tilde{\theta}_s; \quad \tilde{p}_3 = \tilde{p}_s \cos \tilde{\theta}_s. \quad (\text{G.9})$$

By expanding the complex phase function into a Taylor series, we find the steepest-descent direction in the vicinity of the saddle point,

$$\alpha_{\tilde{\theta}_s} = \left\{ \frac{\pi}{4} - \frac{\psi}{2}, \frac{5\pi}{4} - \frac{\psi}{2} \right\}, \quad (\text{G.10})$$

where the perturbation on the steepest-descent direction, $\frac{\psi}{2}$, is the phase angle of the second derivative of the phase function at the saddle point:

$$\phi = \tan^{-1} \left[\frac{\text{Im}(\tilde{Y})}{\text{Re}(\tilde{Y})} \right]; \quad \tilde{Y} = \left. \frac{d^2 [\tilde{p}_s(x_1 \sin\theta + x_3 \cos\theta)]}{d\theta^2} \right|_{\theta=\tilde{\theta}_s}. \quad (\text{G.11})$$

Evaluating the integral G.6 in the high-frequency limit along the steepest descent path

yields

$$\tilde{u}_k(\omega, \mathbf{x}) = \frac{\tilde{U}_k \exp[i\omega \tilde{p}_s(x_1 \sin \tilde{\theta}_s + x_3 \cos \tilde{\theta}_s)]}{\sqrt{\frac{i}{2\pi\omega}} \sqrt{(x_1 \sin \tilde{\theta}_s + x_3 \cos \tilde{\theta}_s) \left[\tilde{p}_s + 2\tilde{p}_s \left(\frac{x_1 \cos \tilde{\theta}_s - x_3 \sin \tilde{\theta}_s}{x_1 \sin \tilde{\theta}_s + x_3 \cos \tilde{\theta}_s} \right)^2 - \frac{d^2 \tilde{p}_s}{d\theta^2} \Big|_{\theta=\tilde{\theta}_s} \right]}}. \quad (\text{G.12})$$